Engineering Radiative Heat Transfer with Thermal Polaritonics

by

Ryan Christopher Kent Starko-Bowes

A thesis submitted in partial fulfillment of the requirements for the degree of

Doctor of Philosophy

in

Photonics and Plasmas

Department of Electrical and Computer Engineering

University of Alberta

Abstract

This thesis explores the concept of polaritons, collective excitations of light and matter, for applications in thermal photonics. Emerging technologies such thermophotovoltaics and passive radiative cooling would greatly benefit from advancements in thermal photonics where complete control over spectral shape, polarization state, directionality and coherence of thermally generated radiation is the ultimate goal. Conventional thought does not associate these properties of light with photons that are thermally generated. However, recent advances in nanophotonics has allowed us to challenge these longstanding assumptions of thermal light.

First, we propose the use of plasmon polaritons in metallic nanowire metamaterials for the purpose of controlling visible frequency light. These metamaterial structures possess strong anisotropic and tunable absorption behavior at visible frequencies. The obvious roadblock that is encountered when moving to high temperature environments is that the metal constituents in plasmonic metamaterials fail.

To rectify the problem of high temperature operation, we subsequently move to polar diatomic ceramic materials, which are known to support phonon polaritons at mid infrared frequencies. Bound surface phonon polaritons in silicon carbide are coupled to free space with the aid of a 2D bi-periodic grating. With this structure patterned in to a single crystal wafer, we are able to achieve two independently controllable emission bands that exist within the Reststrahlen region of silicon carbide.

Localized surface phonon polariton resonances within μ-particles of SiO_2 and SiC are also explored as a means to control mid infrared thermal radiation. The strong overlap between the resonant emission bands of the polaritonic particles and the atmospheric transmission window establishes them as excellent candidates for passive radiative cooling applications. Their emissivity spectrum is determined through direct thermal emission measurements and used to calculate a potential radiative cooling result of $\approx 6°C$ below ambient temperature.

Lastly, we investigate the potential of boron nitride nanotubes (BNNTs) for high temperature mid infrared thermal emission. BNNTs are unique emerging materials that possess optical phonons in two distinct mid infrared bands due to the particles extreme optical anisotropy. We characterize the polaritonic modes of BNNTs through thermal emission and absorption measurements and show that there is strong agreement with Mie theory simulations. This is the first study exploring the thermal radiative behavior of BNNTs and the results tout them as a strong candidate for high temperature thermal photonics applications.

The findings of this thesis help pave the way for future technologies to transform the world we live in through the advancement of thermal photonics.

Preface

Sections of this thesis are reproductions of work published in peer reviewed journals. Chapter 2 and 3 are direct reproductions, published respectively as:

- R. Starko-Bowes, J. Atkinson, W. Newman, H. Hu, T. Kallos, G. Palikaras, R. Fedosejevs, S. Pramanik, and Z. Jacob, "Optical characterization of epsilon-near-zero, epsilon-near-pole, and hyperbolic response in nanowire metamaterials," Journal of the Optical Society of America B 32, 2074-2080 (2015)

- R. Starko-Bowes, J. Dai, W. Newman, S. Molesky, L. Qi, A. Satija, Y. Tsui, M. Gupta, R. Fedosejevs, S. Pramanik, Y. Xuan, Z. Jacob, "Dual-band quasi-coherent radiative thermal source," Journal of Quantitative Spectroscopy and Radiative Transfer 216, 99-104 (2018)

Chapter 4 is comprised of new results and is under preparation for submission to a peer reviewed journal. The concept of the study was formed by myself and Zubin Jacob. All aspects of the project from fabrication and experimental measurement to simulations and writing were carried out by Ryan Starko-Bowes.

Chapter 5 is also comprised of new work and is under preparation for submission to a peer reviewed journal. The concept of this study was formed by a collaboration between Zubin Jacob and Tongcang Li. Sample fabrication was carried out by Zhujing Xu and Ryan Starko-Bowes. Thermal emission measurements were carried out by Xueji Wang and Ryan Starko-Bowes. All other aspects of the project (simulation and writing) were completed by Ryan Starko-Bowes.

For Joanna, Dale and Larisa
with love.

Physics is like sex: sure, it may give some practical results, but that's not why we do it.

– Richard Feynman

Acknowledgements

To Zubin Jacob, your patience, drive, and passion for science are truly admirable. Over the course of my PhD, I have always looked forward to meetings or discussions with you as they would always leave me inspired and renew my passion for science. Thank you for shaping me in to the scientist I am today. I consider myself lucky to have been part of the Jacob research group and know it will go on to achieve greatness. As brief as my tenure was, I am just happy to have been along for the ride.

A tremendous amount of credit goes to my friend and colleague Ward Newman. It was a priviledge working with you in the lab and your "just do it" attitude towards experiments certainly motivated me and pushed my projects to completion faster than they would have otherwise. Cris Cortes, Sean Molesky, Prashant Shekhar, Farid Kalhor, Saman Jahani, and Todd Van Mechelen, thank you for your friendship and inspiring conversations on physics and all else. You have all impacted the way I approach science.

A number of people are owed a massive thanks for collaboration, experimental assistance, and passing on invaluable knowledge. To Yi Xuan, Jerry Shepard, Dave Lubelski, and Kenny Schwartz, from the Birck Nanotechnology Center, thank you for your expertise on all things fabrication and experiment. To Robert Fedosejevs and Manisha Gupta, thank you for valuable discussions as we were getting our projects off the ground. To Ying Tsui and Mojgan Daneshmand, thank you for overseeing my work and sitting on my supervisory committee. To Sandipan Pramanik, thank you for giving me my start in academia. I certainly would not be here had you not allowed me to join your group in 2010.

My graduate career would not have been possible without financial sup-

Contents

List of Tables

List of Figures

List of Abbreviations

Abbreviation	Extended Form
PV	Photovoltaic
TPV	Thermophotovoltaic
LO	Longitudinal Optical
TO	Transverse Optical
EM	Electromagnetic
LST	Lydanne-Sachs-Teller
ENZ	Epsilon-near-zero
ENP	Epsilon-near-pole
SP	Surface Polariton
SPP	Surface Plasmon Polariton
SPhP	Surface Phonon Polariton
LP	Localized Polariton
NW	Nanowire
ML	Multilayer
EDX	Energy Dispersive X-ray
XRD	X-ray Diffraction
AAO	Anodic Aluminum Oxide
SEM	Scanning Electron Microscope
EMT	Effective Medium Theory
FTIR	Fourier Transform Inrared
RCWA	Rigorous Coupled Wave Analysis
BNNT	Boron Nitride Nanotube
hBN	Hexagonal Boron Nitride
TE	Transverse Electric
TM	Transverse Magnetic

List of Symbols

Symbol	Description
λ	Wavelength of radiation
k	Wavevector of radiation
ω	Frequency of radiation
ϵ	Emissivity
α	Absorptivity
ε	Dielectric permittivity
$L(\lambda)$	Planck's law of radiative spectral energy density

Chapter 1

Introduction

1.1   Thermal Emission Engineering

Any discussion of thermal radiation naturally begins with Planck's law, which describes the far-field spectral radiance $L(\lambda, T)$ emitted by a black-body in thermal equilibrium at temperature T:

$$L(\lambda, T) = \frac{2hc^2}{\lambda^5} \frac{1}{e^{\frac{hc}{\lambda k_B T}} - 1},\tag{1.1}$$

where λ is the wavelength of radiation, c is the speed of light ($c = 2.9979 \times 10^8\ m/s$), h is the Planck constant ($h = 6.6261 \times 10^{-31} J \cdot s$) and k_B is the Boltzmann constant ($k_B = 1.3806 \times 10^{-23} J{\cdot}\mathrm{K}^{-1}$). While this is an elegant description of thermal radiation, it is a generalized model of an ideal emitter only valid for macroscopic objects larger than the wavelength of radiation. In practice, bodies can have fine structure or non-ideal emission due to material properties. An object's emissivity spectrum ($\epsilon(\lambda)$) is used to account for this and describe the efficiency with which a material can radiate its thermal energy. The result is the observed linear far-field spectral radiance:

$$I(\lambda, \theta, T) = \epsilon(\lambda, \theta) L(\lambda, T)\,.\tag{1.2}$$

In practice, experimental measurement of an objects thermal radiation spectrum is difficult because of the need for specialized infrared detectors and low intensity levels of emitters around room temperature. In addition strong background signals from the room, optical elements and the detector itself,

1

all at room temperature can bury the thermal signal trying to be detected. Because of this, the majority of studies today use Kirchoff's law to relate the absorptivity spectrum to the emissivity spectrum.

Kirchoff's law states that for any body in thermodynamic equilibrium, its emissive power is equal to its absorptive power at any wavelength. That is to say its spectral emissivity is equal to its spectral absorptivity ($\epsilon(\lambda) = \alpha(\lambda)$) [1]. Using this relation one would be able to measure an objects emissivity spectrum simply by careful measurement of its absorptivity. In addition, if a material is fully opaque ($T = 0$), the emissivity spectrum can also be approximated as $\epsilon(\lambda) = 1 - R(\lambda)$, where $R(\lambda)$ is the spectral reflectivity. These optical characterization techniques are routinely used to measure the emissivity of photonic devices. While this is a good approximation for the emissivity, we know that material properties can change in different environments, especially at high temperature where thermal radiation is of great interest.

In this thesis, Kirchoff's law will not be taken for granted. Direct thermal emission measurements of photonic devices at varying temperatures are taken wherever possible and compared to absorption measurements at room temperature for direct verification of Kirchoff's law. This also gives insight in to the evolution of material properties through varying temperatures.

Advanaces in photonics and our understanding of light matter interactions has lead to the notion that we can control not only spectral emissivity features [2], [3] but polarization [4], coherence [5] and angular dependence [6] of thermal radiation as well. These discoveries have sparked interest in several emerging technologies like thermophotovoltaics [7], [8], radiative cooling [9], [10] and narrowband thermal infrared sources [6], [11], [12]. In the following sections, we will discuss the underlying physics we will use to achieve the above radiative properties.

1.2 Motivating Technologies

1.2.1 Passive Radiative Cooling

One of the most promising applications of thermal emission engineering, and main motivations of this thesis, is passive radiative cooling whereby the emissivity spectrum of a material is engineered in such a way that it preferentially radiates its own thermal energy away without absorbing much from the sun or atmosphere. The results is a device that passively lowers its temperature without any external energy input. Naturally, one can imagine the impact of such a technology in hot climates where air conditioning (AC) systems drive high energy demand. Currently, refrigeration (including AC) accounts for 17% of world electricity consumption [13]. As the global standard of living rises, it is projected that AC units will grow from 1.6 billion today to 5.6 billion by the year 2050 [14]. This proliferation of AC units (primarily in developing countries with warm climates) will greatly contribute to our growing worldwide electricity demand. Moreover, because the electricity produced today is predominantly generated by burning fossil fuels, AC units contribute to the very thing they are trying to combat, a warming climate. To prevent such a positive feedback loop from running away, it will be critical to address cooling technologies in a novel and cost effective way. Passive radiative cooling is one technology that promises to address this world problem.

During the daytime any object will interact with radiation from the sun (P_{sun}) and the atmosphere (P_{atm}) in addition to thermal energy it gains (or loses) through convection and conduction (P_{con}). As described in section 1.1, any object will also radiate its thermal energy away according to equation (1.2). Part of this energy will be absorbed by the atmosphere. However, in regions where the atmosphere is transmissive, radiation will be allowed to escape to outer space. A schematic representation of the radiative cooling effect and the terms involved in energy transfer is shown in figure 1.1. The net cooling effect from all terms involved can then be calculated as:

$$P_{cool}(T_a, T_S) = P_{rad}(T_S) - P_{atm}(T_a) - P_{sun} - P_{con}(T_a, T_S), \qquad (1.3)$$
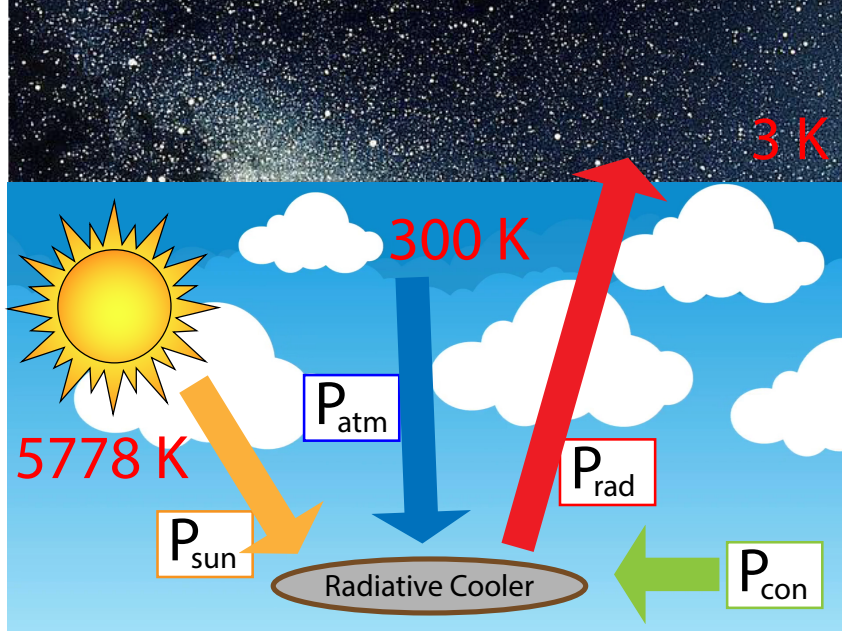
Figure 1.1: Schematic of radiative cooling effect. P_{sun} is the power absorbed by the sun, P_{atm} is the power absorbed from the atmosphere, P_{con} is the power absorbed via conduction and convection and P_{rad} is the power emitted out by the radiative cooler.

where T_a is the ambient air temperature and T_S is the sample temperature.

1.2.2 Thermophotovoltaics

The vast majority of electricity generated today is generated through an exothermic process. This could be burning fossil fuels or nuclear fission reactions. Generally, this heat is used to generate steam, which is then forced through a turbine that converts its kinetic energy to electricity. Thermal losses in combustion power plants account for 50-60% of the total power [15], [16]. Thermophotovoltaic electricity generation also suffers from the Shockley-Queissar limit of 41% [17]. The main reason for this is that the majority of energy in the solar spectrum lies in frequencies outside that of a photovoltaic (PV) cell's bandgap. However, if the incident spectral energy density has strong overlap with the bandgap of the PV cell, the energy conversion efficiency can be greatly improved.

The field of thermophotovoltaics (TPV) aims to improve electricity generation by converting thermal energy to electricity via photonic energy transfer.

Figure 1.2 shows the spectral radiance of a black-body at 1500 K. Highlighted in red is the spectral region of high energy conversion of a hypothetical low bandgap PV cell.
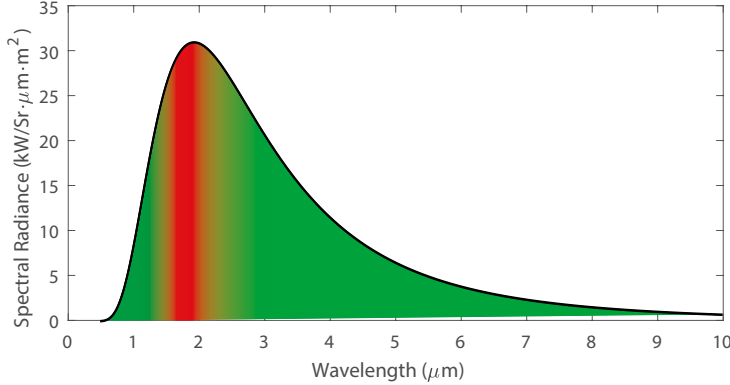
Figure 1.2: Black-body spectral radiance at 1500 K. The red highlighted area shows the spectral region of high conversion efficiency for a single junction photovoltaic cell.

By tailoring the emissivity spectrum of a thermal emitter to have maximal overlap with the highlighted high conversion efficiency region, we can ensure that minimal photons are lost to thermalization. Recent works have already shown the feasibility of this technology, achieving conversion efficencies as high as 24% [18]. However, further progress is needed to achieve the promise of TPV, surpassing the Shockley-Queissar limit [19].

1.3   Permittivity and the Lorentz Model

In this thesis, we will use material oscillators as the fundamental building blocks to control a materials emissive properties. This section will introduce the framework used to handle the interaction between electromagnetism and matter. Within Maxwell's equations, we use permittivity ($\varepsilon(\omega)$) and permeability ($\mu(\omega)$) to represent the linear electric and magnetic response, respectively, of electromagnetic radiation in frequency (ω) dispersive media. For nonmagnetic material (which will exclusively be used in this thesis) we can set $\mu(\omega) = 1$ and only consider $\varepsilon(\omega)$ to fully describe the electromagnetic field. In the presence of an electric field, such a material will accumulate a charge

separation known as the displacement field $\boldsymbol{D}$:

$$\boldsymbol{D} = \varepsilon_0 \boldsymbol{E} + \boldsymbol{P} = \varepsilon_0 (1 + \chi) \boldsymbol{E} = \varepsilon_0 \varepsilon_r \boldsymbol{E} \,, \tag{1.4}$$

where $\varepsilon_0 = 8.854 \times 10^{-12} F/m$ is the free space permittivity, $\boldsymbol{E}$ is the applied electric field, $\boldsymbol{P}$ is the polarization density, χ is the susceptibility and ε_r is the relative permittivity. Typically when permittivity is mentioned, people are actually referring to relative permittivity. This convention will be adopted throughout this thesis as well. This relative permittivity can further be separated in to its real ($\varepsilon'(\omega)$) and imaginary ($\varepsilon''(\omega)$) parts, which relate to the phase shift and dissipation of the EM wave, respectively.

Modelling the optical properties of a material can give an analytical description for the behavior of radiation in that medium. By treating the charged particles (typically electrons or ionic nuclei) in a medium as harmonic oscillators, we arrive at the well known and versatile Lorentz model:

$$\varepsilon(\omega) = \varepsilon'(\omega) + i\varepsilon''(\omega) = \varepsilon_\infty + \frac{\omega_p^2}{\omega_0^2 - \omega^2 - i\omega\gamma} \,, \tag{1.5}$$

where ω is the frequency of radiation, ε_∞ is the high frequency limit permittivity, $\omega_0 = \sqrt{K/m}$ is the natural resonant frequency of the oscillator (K is spring constant and m is mass of the oscillator), γ is the damping coefficient and ω_p is known as the plasma frequency. The plasma frequency is defined as:

$$\omega_p^2 = \frac{Nq^2}{\varepsilon_0 m} \,. \tag{1.6}$$

Here, q and m are the charge and mass of the oscillating particle and N is the charged particle density.

1.3.1 Drude Model for Free Charge Carriers

For metals, we can assume that free electrons respond to electric fields and are the charged oscillating particles responsible for polarizability. This is shown in figure 1.3 a). Because they are not bound to atomic nuclei and hence, move freely, there is no resonant frequency of the oscillator ($\omega_0 = 0$). We can then recover the well known Drude model

Plasmon Oscillation

Phonon Oscillation
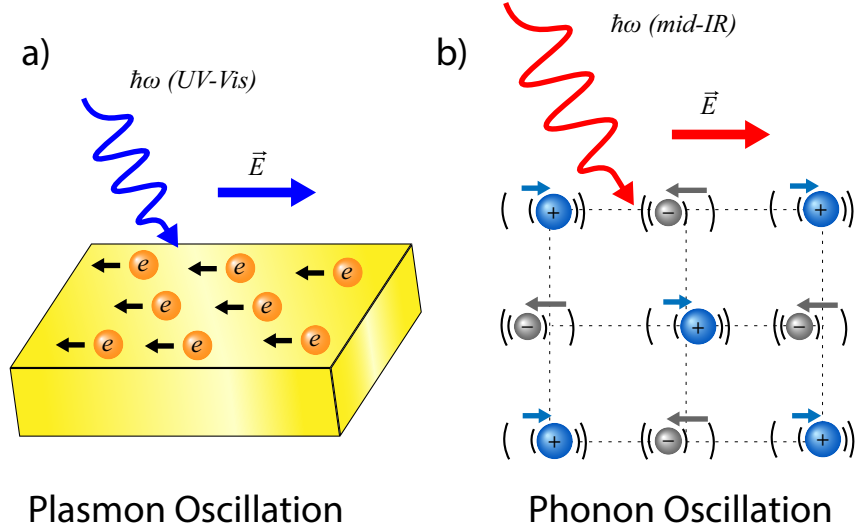
Figure 1.3: a) Electron response to incident EM wave in metals (plasmon oscillation). b) Ion response to to IR radiation in diatomic crystal (phonon oscillation).

$$\varepsilon(\omega) = \varepsilon_\infty - \frac{\omega_p^2}{\omega^2 + i\omega\gamma} \, . \tag{1.7}$$

In the case of the Drude model for metals, $q \rightarrow q_e$ (charge of electron) and $m \rightarrow m_e$ (mass of electron). From this expression, we can see that for frequencies below ω_p, we are left with a negative permittivity. In regions where the permittivity is negative, electrons are able to respond to oscillating electric fields. This leads to quickly decaying fields and high reflectivity in the metal. At frequencies above the plasma frequency, we obtain a positive permittivity, which conveys that the material is transparent to these frequencies. The Drude model is relatively accurate for predicting permittivity of metals at energies below their interband transitions. However, this can be improved by incorporating additional Lorentz oscillator terms as in equation (1.5). Figure 1.4 shows the Drude model representation for the example metals of tungsten (W), gold (Au) and copper (Cu).

In addition to metals, the Drude model can also be used to describe doped semiconductors where we can control the charge carrier density with doping concentrations or induced electric fields. This gives great control of optical properties in semiconductors for photonic applications.
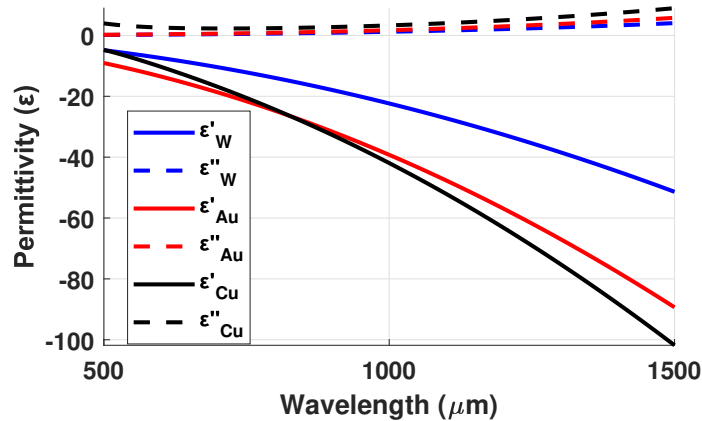
Figure 1.4: Drude model for metals of tungsten (blue), gold (red) and copper(black). Real part of permittivity ($\varepsilon'(\omega)$) is solid lines while imaginary ($\varepsilon''(\omega)$) part is in dashed lines.

1.3.2 Lorentz Model for Polar Dielectrics

The atomic nuclei of polar diatomic crystals such as SiC carry a partial charge on them due to differing electronegativity of the constituent atoms. For this reason the atomic nuclei are semi-charged ions that will respond to EM radiation, even though there are no free charge carriers as is the case in metals (figure 1.3 b)). However, this type of optical response will occur at much lower frequencies due to the relatively massive ion (when compared to the electron). This turns out to be an excellent system for the application of the Lorentz model as these semi-charged particles are bound to lattice sites and will experience a resonant frequency (ω_0).

Because these phononic oscillations are able to couple to EM fields they are considered optically active and we refer to them as optical phonons. In optical phonons, the sublattices of diatomic crystals oscillate out of phase and there are two modes that can exist. Transverse optical (TO) phonons have their particle motion perpendicular to the direction of propgation or wavevector ($\vec{k}$) as is the case in EM radiation. In contrast, a longitudinal optical (LO) phonon has its particle motion parallel to the wavevector as in a pressure or sound wave. Because of this, the LO phonon mode is, in general, unable to be excited by a transverse EM wave. This conclusion is supported by Gauss's

8

law which states $\nabla \cdot \boldsymbol{D} = \varepsilon_0 \varepsilon_r \nabla \cdot \boldsymbol{E} = 0$, which implies $\boldsymbol{k} \cdot \boldsymbol{E} = 0$. However, this condition can also be satisfied if $\varepsilon_r = 0$. We will use this condition to help represent the Lorentz model, equation (1.5), in more useful terms when considering optical phonons in polar crystals.

Because there are generally no free charge carriers in a diatomic crystal, the concept of a plasma frequency does not hold the same meaning. Instead, it can be helpful to represent the Lorentz model in terms of its LO and TO frequencies (ω_{LO} and ω_{TO}). To do this we employ the Lydanne-Sachs-Teller (LST) relationship:

$$\frac{\omega_{LO}^2}{\omega_{TO}^2} = \frac{\varepsilon(0)}{\varepsilon_\infty} \, . \tag{1.8}$$

If we evaluate the static permittivity ($\varepsilon(\omega = 0)$) of the Lorentz model, we can represent the plasma frequency as:

$$\omega_p^2 = \omega_{TO}^2 (\varepsilon(0) - \varepsilon_\infty) \, . \tag{1.9}$$

Using equations (1.5), (1.8) and (1.9), we arrive at:

$$\varepsilon(\omega) = \varepsilon_\infty \left(1 + \frac{\omega_{LO}^2 - \omega_{TO}^2}{\omega_{TO}^2 - \omega^2 - i\gamma\omega} \right) . \tag{1.10}$$

This gives rise to a negative real permittivity bounded by the two optical phonon frequencies ($\varepsilon'(\omega_{TO} - \omega_{LO}) < 0$), which results in a high reflectivity region known as the "Restsrahlen" band. Figure 1.5 shows the Reststrahlen effect in experimental (exp.) reflectivity measurements for two types of SiC. The reflectivity measurements are fit using Lorentz and Drude terms, which is also plotted in figure 1.5. The semi-insulating (SI) SiC shows strong reflectivity in the region from 10.3-12.5 μm as there are no free carriers so the reflection is a direct result of phonon modes. Its permittivity is well modelled by a single Lorentz oscillator. The conductive (C) form of SiC has dopants (nitrogen) and free electrons introduced which causes increased damping, lowering the reflectivity in the Restsrahlen band. To accurately model its reflectivity, an additional Drude term must be added. Another consequence of doping is the
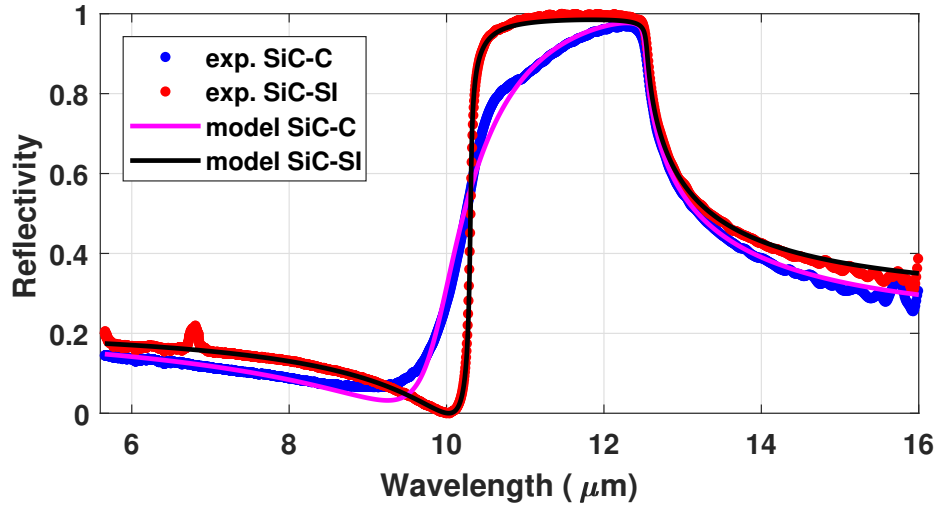
Figure 1.5: Reflectance Measurements of SiC wafers and their fitting results to Lorentz models.

fact that the epsilon-near-zero (ENZ) point is blue shifted. This can be seen in figure 1.6 where the analytical permittivity functions are shown.
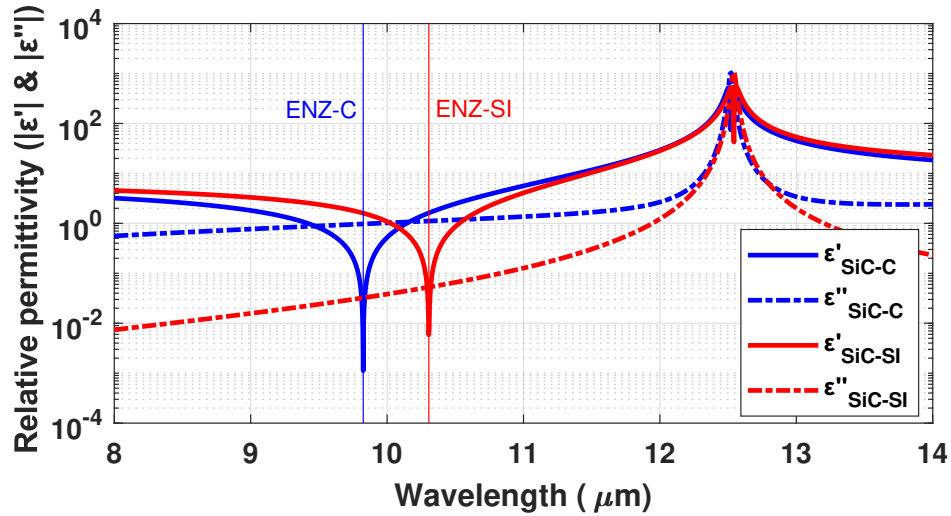
Figure 1.6: Lorentz model of real (solid lines) and imaginary (dashed lines) permittivities of semi-insulating (red) and conducting (blue) SiC wafers.

1.4   Polaritons

Polaritons are wave-like quasi-particles that possess an electric or magnetic dipole moment. They exist at the interface between two materials with one

10

having a positive real permittivity ($\varepsilon'_1 > 0$) and the other having a negative real permittivity ($\varepsilon'_2 < 0$) as shown in figure 1.7. Due to the oscillation of charges within a polaritonic medium, these quasiparticles are able to couple to light. For reasons described in section 1.3, plasmonic and phononic materials are exemplary candidates for engineering light matter interactions and radiative thermal emission. In this section, we will describe two forms of polaritons and discuss how we can use nano and micro-structure to engineer selective thermal emission.
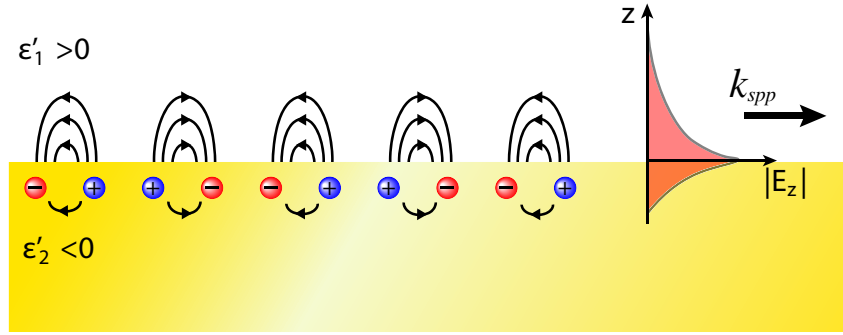
Figure 1.7: Schematic of propagating surface polariton that exists at the interface between a metal and dielectric.

1.4.1 Surface Polaritons and Gratings

Surface polaritons (SP's) are confined to a plane interface between a dielectric ($\varepsilon'_1 > 0$) and a metallic ($\varepsilon'_2 < 0$) material. Maxwell's equations do not discriminate between charge oscillations and as a result, SP's can exist on the surface of metals as surface plasmon polaritons (SPP) or polar dielectric crystals as surface phonon polaritons (SPhP). This forms a 2D space on the surface of the metal where the SP is allowed to propagate. The SP will experience frequency dependant dispersion that follows:

$$k_{SP} = \frac{\omega}{c}\sqrt{\frac{\varepsilon_1(\omega)\varepsilon_2(\omega)}{\varepsilon_1(\omega) + \varepsilon_2(\omega)}}, \qquad (1.11)$$

An example of the dispersion relation for a SiC-vacuum interface are shown in figure 1.8. Also shown is the bulk material dispersion (k_B) and the free space dispersion or "light line" (k_c).

11
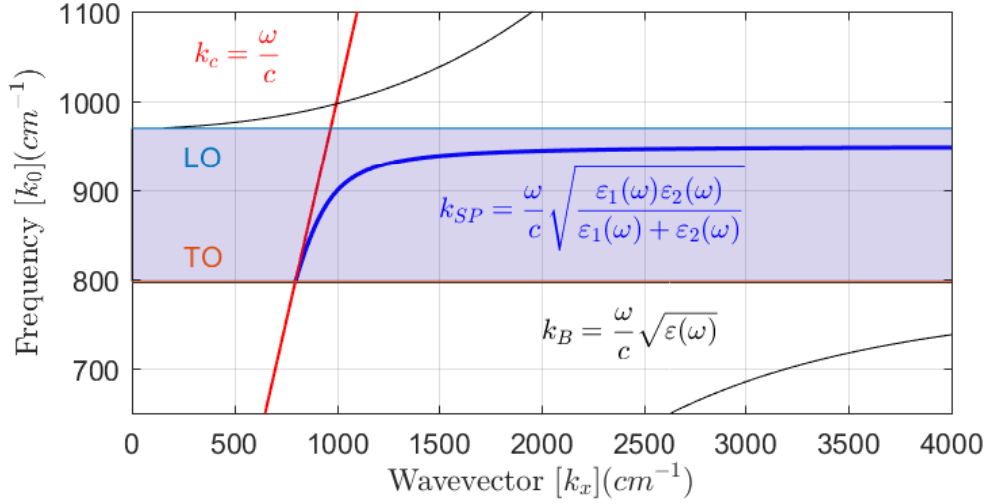
Figure 1.8: Dispersion relation of surface polariton in SiC (blue line). The SP exists only within the shaded region which represents the Reststrahlen band where $\varepsilon(\omega)' < 0$. Black line is the bulk polariton mode. The light line is also shown in red.

In the area above the light line, radiation is able to propagate in free space and therefore material modes can efficiently couple to light here. However, modes that lie below the light line, such as k_{SP}, are confined within the material and do not couple to free space modes. This is the result of the momentum mismatch between the surface mode and free space. Several methods to overcome this momentum mismatch can be employed such as prism coupling or, what we will use later in this thesis, grating coupling.

By introducing a grating into the flat interface, the propogation of the SP can be impeded, lowering its k_x and scattering the polariton into the light cone. The new SP dispersion will follow the relation:

$$\sqrt{\varepsilon_1} k_0 sin\theta = \boldsymbol{k}_{SP} - \boldsymbol{k}_G\,, \tag{1.12}$$

where θ is the angle of propagation relative to normal, k_0 is the free space wavevector and $\boldsymbol{k}_G = 2\pi m/\Lambda$ is the grating vector (m being an integer). Figure 1.9 shows the SP dispersion of a SiC-vacuum interface after a grating of period $\Lambda = 9.6\mu m$ has been patterned.

12
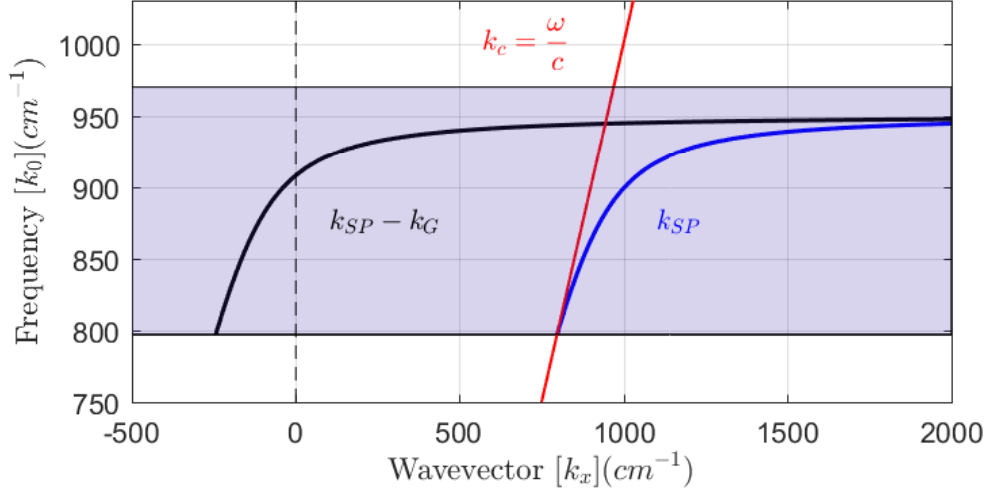
Figure 1.9: Dispersion relation of surface polariton in SiC with a 9.6 μm grating patterned in to the interface (black line). The original SP with no grating at the interface is also shown (blue line). The grating scatters the surface bound wave in to free space propogating modes. The light line is also shown in red.

1.4.2 Localized Polaritons and Particles

In the context of a sub-wavelength particle, the concept of a surface wave is ill-defined. Instead, for particles with large curvature or sharp features, we can describe their interaction with electromagnetic radiation in terms of scattering. Because the oscillating polaritons within these particles are confined to its volume and not able to propogate, we call them localized polaritons (LP). Here, we are again able to couple polaritonic modes to light. However, because there is no flat surface to propagate along, the particle itself radiates according to its LP modes.

For the case where particles are much smaller than the wavelength ($d <<$ λ), the particle will experience a uniform electric field throughout its volume. This is known as the quasi-static limit (figure 1.10). In this regime, the electric response is dominated by the dipolar term, which results in a single narrow line width resonance. This mode is referred to as the Fröhlich mode, which occurs approximately when $\varepsilon_2'(\omega) = -2\varepsilon_1'$ (ε_2 is the particles permittivity and ε_1 is the surrounding material permittivity). In phonon polaritonic materials
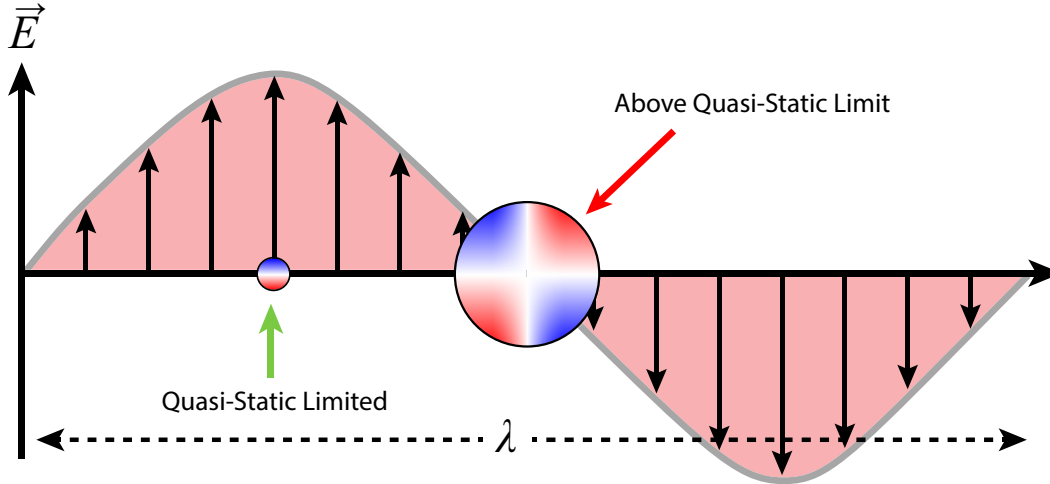
Figure 1.10: Schematic representation of quasistatic limit. Small particle on the left is within the quasi-static limit and experiences a uniform electric field. Its response is dominated by a dipolar moment. The larger particle on the right is outside the quasi-static limit and experiences a nonuniform field. Higher order terms contribute significantly to its response. It is shown with a quadripole moment.

we can calculate the Fröhlich mode as:

$$\omega_F = \sqrt{\frac{\omega_{LO}^2 + \omega_{TO}^2 \frac{2\varepsilon_1}{\varepsilon_\infty}}{1 + \frac{2\varepsilon_1}{\varepsilon_\infty}}} \; . \tag{1.13}$$

As the size of the particle becomes larger, higher order multipolar terms become more dominant and cannot be neglected. These higher order terms can add neighbouring absorption bands, broadening the overall absorption profile of the particle. The exact scattering and absorption properties of sub-wavelength particles was reported by Gustav Mie in 1908 [20]. As these calculations can be quite cumbersome, the equations have been moved to appendix C.

1.5   Overview of Thesis

The aim of this thesis is to uncover new designs, materials and nanostructures that will allow us to better control thermal radiative properties in novel ways. In this section (Chapter 1) we motivate the work by discussing some of the technologies where thermal emission engineering can play a major role. We also

introduce the physics governing electromagnetic fields and resonances within materials, namely polaritons, and discuss mechanisms we can use to couple these material modes to light and thermal radiation.

Chapter 2 explores the potential of plasmonic metamaterials to control light matter interactions. In particular, a 2D metamaterial of gold nanowires in an alumina matrix is used to engineer visible absorption resonances via localized plasmon polaritonic resonances. The nanowire metamaterial is contrasted with a multilayer metamaterial system to emphasize the benefits of strong resonances in 2D metamaterial systems. The fabrication process, which is significantly more involved than that of multilayer systems, is also described in detail. As its resonances are in the visible spectrum, they need to be heated to extremely hot temperatures ($> 1300 \; K$) to have any appreciable thermal emission that can be detected. At these temperatures, the gold nanowires will not survive. This motivates the need for high temperature stable polaritonic materials in the chapters to follow. Milestones achieved in this first study include:

- Development of a robust procedure to fabricate metal nanowire metamaterials on glass (or arbitrary) substrates for optical characterization.

- Demonstrated control of ENZ and ENP resonance frequencies through fabrication procedure variables.

Chapter 3 addresses the high temperature stability roadblock by moving to an advanced ceramic material, silicon carbide. SiC is a polar diatomic crystal that possesses optical phonons and supports surface phonon polaritons. A 2D, bi-periodic grating is designed and patterned in to the SiC wafer to couple the bound surface modes in to free space propagating radiation. Using this structure, we are able to control the frequency, polarization and directionality of narrow thermal emission features within the Reststrahlen band of SiC. Some notable accomplishments from this study are:

- Design, construction and calibration of a custom high temperature vacuum chamber coupled with an FTIR spectrometer experimental set up.

- Demonstrated control of surface polariton coupled emissivity bands through angular and temperature dependent emission measurements.

In Chapter 4, localized polaritonic resonances are used to couple optical phonons in SiO_2 and SiC to free space radiation. Due to the strong overlap between the atmospheric transmission window and the Reststrahlen bands of SiO_2 and SiC, passive radiative cooling becomes a well suited application. The emissivity spectrum of SiO_2 μ-spheres and SiC μ-particles is calculated from thermal emission measurements. The emissivity spectrum is then used to theoretically calculate approximate values of cooling power for a polaritonic particle passive radiative cooler.

- First direct measurement of thermal emission from SiO_2 and SiC phonon polariton particle systems.

- Demonstration of thermal emission technique to investigate polaritonic particle resonant modes.

Chapter 5 looks at the thermal emission spectrum from an extremely unique and emerging material system, boron nitride nanotubes (BNNT). BN-NTs are the tubular form of hexagonal boron nitride which is a natural hyperbolic material that supports optical phonons in two distinct spectral regions. Moreover, studies have shown BNNTs to be stable at high temperatures making them excellent candidates for thermal emission measurements. The results from this study has lead to significant impactful discoveries such as:

- Observation of high frequency localized optical phonons through thermal emission. Highest known phononic Reststrahlen band that exists.

- Extreme temperature stability of 1D polaritonic ceramic particle emitter.

Chapter 2

Optical Characterization of Epsilon-near-zero, Epsilon-near-pole, and Hyperbolic Response in Nanowire Metamaterials

We report on the optical and physical characterization of metallic nanowire (NW) metamaterials fabricated by electrodeposition of ≈30 nm diameter gold nanowires in nanoporous anodic aluminum oxide. We observe a uniaxial anisotropic dielectric response for the NW metamaterials that displays both epsilon-near-zero (ENZ) and epsilon-near-pole (ENP) resonances. We show that a fundamental difference in the behavior of NW metamaterials from metal-dielectric multilayer (ML) metamaterials is the differing directions of the ENZ and ENP dielectric responses relative to the optical axis of the effective dielectric tensor. In contrast to multilayer metamaterials, nanowire metamaterials exhibit an omnidirectional ENP and an angularly dependent ENZ. Also in contrast to ML metamaterials, the NW metamaterials exhibit ENP and ENZ resonances that are highly absorptive and can be effectively excited from free space. Our fabrication allows a large tunability of the epsilonnear-zero resonance in the visible and near-IR spectrum from 583 to 805 nm as the gold nanorod fill fraction changes from 26 % to 10.5 %. We support our fabrication process flow at each step with rigorous physical and optical characterization.

Energy dispersive x-ray (EDX) and x-ray diffraction (XRD) analyses are used to ascertain the quality of electrochemically deposited Au nanowires prior to and after annealing. Our experimental results are in agreement with simulations of the periodic plasmonic crystal and also analytical calculations in the effective medium metamaterial limit. We also experimentally characterize the role of spatial dispersion at the ENZ resonance and show that the effect does not occur for the ENP resonance. The application of these materials to the fields of biosensing, quantum optics, and thermal devices shows considerable promise.

2.1   Introduction

Nanowire (NW) and multilayer (ML) metamaterials made of plasmonic metals are the two most promising designs for device applications that show tunable epsilon-near-zero (ENZ) [21], epsilon-near-pole (ENP) [22], and hyperbolic responses [23]–[25]. These three exotic electromagnetic responses arise from the coupled plasmon-polaritons in the multilayer superlattice and nanowire geometries. Although both the NW and ML metamaterials can be characterized by an effective uniaxial dielectric tensor the key characteristics of the types of plasmons supported by each of these two structures cause the two materials to display very distinct electromagnetic responses (see figure 2.1). While ML metamaterials are generally easier to fabricate, NW metamaterials offer significant benefits in terms of higher transmission, lower loss, and a broad tunability across the visible frequency range [21], [23], [26], [27]. As a result, NW metamaterials are expected to have dramatic impacts in fields such as superresolution imaging [28], polarization control/filtering [29], thermal photovoltaics (TPV) [22], [30]–[33], and biosensing [26].

Several procedures have been used by different groups to achieve metamaterials of metallic nanowires in a dielectric matrix. The most common and by far the easiest way to fabricate nanowire arrays is to deposit metal via electrodeposition into the pores of anodic aluminum oxide (AAO) templates. These templates are commercially available [24]; however, additional control

over the template properties can be gained by fabricating them in-house on either Al foil substrates [34]–[36] or Al thin films that have been deposited onto transparent substrates [23]. Depending on sample constraints, metallic nanowires (typically Au or Ag) can be deposited by either AC [34] or DC [23], [24], [35], [36] electrochemical deposition. A simple yet effective technique to characterize and confirm the ENZ, ENP, and hyperbolic responses of the systems is to study spectrally resolved angular transmission measurements [34], [37]. More sophisticated characterization techniques, such as Brewster angle discontinuity reflection measurements [24], shifting of Fabry–Perot oscillations [35], and near-field scanning optical microscopy [36], allow for a deeper understanding of the optical response of the nanowire metamaterials. In this paper, we report on the optical and physical characterization of nanowire metamaterials emphasizing the key differences between ML and NW metamaterials. Even though a body of research exists on these two nanostructured media, we show that the difference in resonant characteristics arises from the opposite orientations of the ENZ and ENP responses. Our work also shows for the first time the role of the ENP metamaterial and its omnidirectional nature, which was recently predicted to have applications in Salisbury screens [38]. For completeness, we present the in-depth fabrication procedure of an array of vertically aligned gold nanowires housed in an AAO matrix supported by an optically transparent glass substrate. To optimize the quality of our NW materials we have analyzed the fabrication with rigorous material characterization and structural analysis using scanning electron microscopy (SEM), energy dispersive x-ray (EDX), and x-ray diffraction (XRD) characterization techniques at each step of the process flow. Reliable estimates of NW fill fractions are extracted using postprocessing of SEM micrograph images. The tunabilities of the ENZ and ENP absorption resonances of the nanowire metamaterials were observed using white-light transmittance measurements and are presented as extinction spectra for metamaterials containing different fill fraction/ nanowire diameters. Theoretical analysis and modeling in the form of effective medium theory (EMT) and full-wave numerical simulation (commercial software CST) [39] show excellent agreement with experimental data.

Finally, we experimentally contrast the spatially dispersive properties of the ENZ and ENP resonances. This work will help researchers adopt our approach to large-area nanowire fabrication and characterization for possible quantum, thermal, and imaging applications [40]–[43].
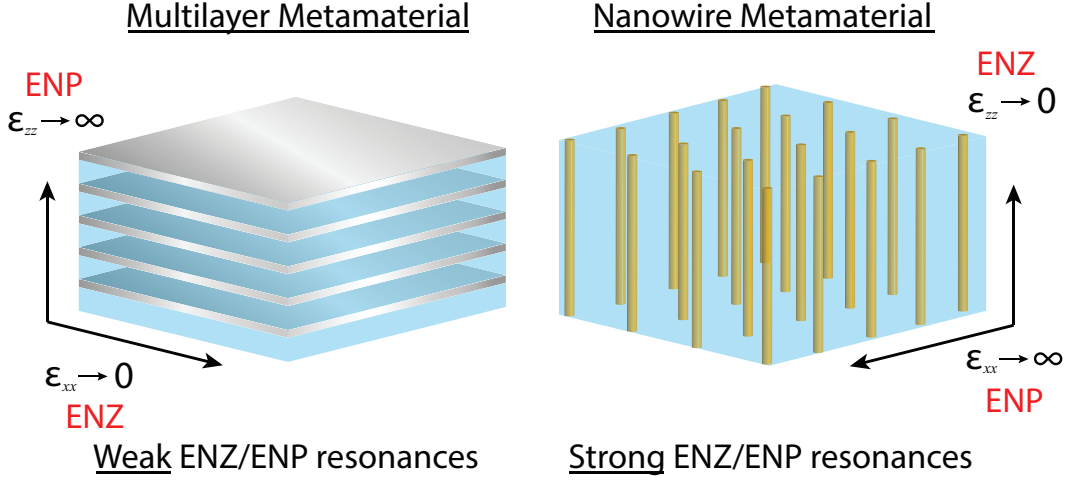
Figure 2.1: Schematic depiction of multilayer versus nanowire metamaterials cross section and the orientation of the ENZ and ENP directions. The difference in directions causes a stark contrast in resonant properties.

2.2 Theory

ML metamaterials have a periodic structure of alternating subwavelength metal and dielectric layers in one dimension ($\vec{z}$). In contrast, NW metamaterials have a periodic structure in two dimensions ($\vec{x}$ and $\vec{y}$). Both structure types are characterized by an effective dielectric tensor that is uniaxial anisotropic that displays ENZ, ENP, and hyperbolic dispersion. However, the directions in which the ENZ and ENP occur are opposite for two structures. Interestingly the NW metamaterials exhibit an angularly dependent ENZ resonance whose spectral location is highly tunable and can be controlled by adjusting the metal nanowire fill fraction. Even though ML metamaterials also exhibit ENP and ENZ resonances as the NW metamaterials do, their resonance characteristics are significantly weaker due to free electron motion in the $\vec{x}$ and $\vec{y}$ directions leading to high reflection of incoming propagating fields [22], [32], [44]. A useful metric to quantify the absorption spectra of the metamaterials

is the extinction (optical density, OD) spectrum. In this study, the extinction spectrum is defined as $OD = -log_{10}(T)$, where T is the transmittance through the sample. This definition is used theoretically in simulations as well as experimentally to characterize absorbing plasmonic resonances. Peaks will occur in extinction spectra at locations of low transmission. Diffuse reflection measurements indicate that reflection and scattering is relatively weak for our NW samples in the visible and near-IR spectrum. This implies that peaks in the extinction spectra can be associated with absorption through plasmonic resonances. The extinction peaks in this study are solely a result of the localized and collective plasmon resonances of the nanowire arrays. There are no Fabry–Perot effects observed in these samples. Additional Fabry–Perot resonant reflection (low transmittance) peaks are only observed in samples with nanowires above 700 nm in length. Longer nanowires result in stronger absorption peaks for our samples but do not change the location of the peaks because they are well below the 700 nm threshold. At the ENZ wavelength, there exists field enhancement inside the metamaterial for the component of the electric field normal to the metamaterial air interface for (p)-polarized light. However, continuity of the displacement field $(\varepsilon_{air}(E_z^{inc} + E_z^{ref}) = \varepsilon_z E_z^{trans})$ dictates that this phenomenon can occur only if the dielectric constant with the ENZ occurs in the direction perpendicular to the interface ($\varepsilon_z \to 0$). Thus, ML metamaterials which have ENZ in the parallel component of the permittivity tensor ($\varepsilon_x \to 0$) do not exhibit the same field enhancement and absorption at ENZ wavelengths present in NW metamaterials. Furthermore, the NW ENP resonance is polarization insensitive and omnidirectional because the parallel component of the dielectric tensor (ε_x) interacts with both (s)- and (p)-polarized light. This makes ENP metamaterials attractive for thermal applications [22], [30]–[33] and Salisbury screens [38] where omnidirectionality and polarization insensitivity is important. Our experimental work explains these effects using EMT.

Using EMT we can calculate the effective permittivities of the nanowire metamaterial, which are described by the following equations:

$$\varepsilon_{xx} = \varepsilon_{yy} = \varepsilon_d \left[\frac{\varepsilon_m(1+\rho) + \varepsilon_d(1-\rho)}{\varepsilon_m(1-\rho) + \varepsilon_d(1+\rho)} \right] \qquad (2.1)$$

$$\varepsilon_{zz} = \varepsilon_m\rho + \varepsilon_d(1-\rho) \qquad (2.2)$$

where ε_d is the permittivity of the dielectric host, ε_m is the permittivity of the metal nanowires, and ρ is the metal fill fraction ratio, which is defined as

$$\rho = \frac{\text{nanowire area}}{\text{unit cell area}} \qquad (2.3)$$

For $\rho \ll 1$ the ENP is weakly dependent on the fill fraction and the condition reduces to $\varepsilon_m + \varepsilon_d \approx 0$. On the other hand the ENZ resonance is strongly dependent on the fill fraction and can be tuned by exploiting this fact.

Figure 2.2 (a) shows the complex permittivity of a nanowire array with a fill fraction of 22% [45]. A pole exists in $\mathrm{Re}(\varepsilon_{xx})$ which dictates the location of the ENP resonance, while a zero exists in $\mathrm{Re}(\epsilon_{zz})$ dictating the location of the ENZ resonance. We confirm this through EMT and CST extinction simulations presented in figure 2.2 (b). ML metamaterial permittivities are shown in figure 2.2 (c) for a five-period structure with a fill fraction of 20%. An ENZ is present in this plot as well as a much weaker ENP. The extinction spectrum of the ML structure simulated through EMT and CST is presented in figure 2.2 (d), where the absence of sharp absorption peaks (that are present in the NW extinction) can be noted.

2.3   Fabrication Procedure

Transparent NW metamaterial thin films are fabricated on clear rigid substrates. Glass slides are first cleaned with a 15 min Piranha bath (3:1 sulfuric acid:hydrogen peroxide). A 20 nm TiO_2 layer is deposited as an adhesion layer between the glass substrate and a gold layer using atomic layer deposition. A subsequent 7 nm Au layer is deposited using DC magnetron sputtering, which will later act as a cathode during electrodeposition. Finally, a 700 nm layer of Al is deposited on top of the Au layer using DC magnetron sputtering.
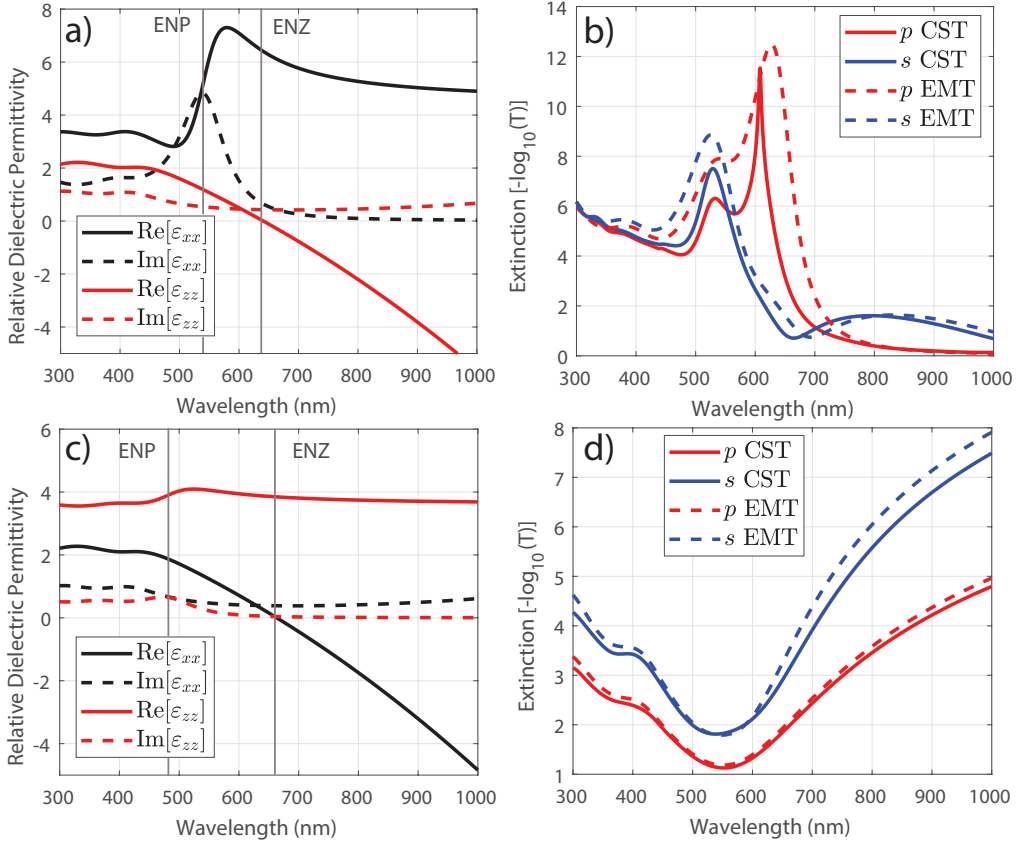
Figure 2.2: real and imaginary parts of effective medium theory (EMT) permittivity in the parallel (ε_{xx}) and perpendicular (ε_{yy}) directions of (a) Au nanowire array in alumina matrix metamaterials and (c) Au-alumina multilayer (five period) metamaterial with a fill fraction of 22% and 20%, respectively. Simulated extinction spectra of (b) Au nanowire array in alumina matrix metamaterial on glass substrate and (d) Au-alumina multilayer (five period) metamaterial from EMT and CST (full-wave simulation) under s and p-polarization at 60∘ plane wave incidence. Dashed blue line and dashed red line are extinction from EMT under s-polarization and p-polarization, respectively. Solid blue line and solid red line are extinction from CST under s-polarization and p-polarization, respectively. The parameters we use for (a) and (b) are as follows: nanowire radius 16 nm, nanowire length 300 nm, and nanowire spacing 65 nm, which gives a fill fraction of 22%. The wavelength of T resonance and L resonance from CST is 524 and 602 nm, respectively (523 and 624 nm from EMT). The parameters we use for (c) and (d) are as follows: Au thickness 10 nm, alumina thickness 40 nm, five periods, total thickness 250 nm, which gives a fill fraction of 20%. The multilayer structure shows no absorption resonances unlike the nanowire design even though both designs possess epsilon-near-zero, epsilon-near-pole, and hyperbolic response.

A two-step anodization procedure is performed on the Al layer to transform the Al metal into nanoporous Al_2O_3 called AAO. Fortuitously, pores are formed via self-assembly in a quasi-hexagonal closed pack structure. The same electrolyte is used for each step [46] and this helps to improve pore order over a one-step procedure. The first anodization step uses 3% oxalic acid with a 30 V bias for 9 min. This initial Al_2O_3 oxide layer is removed with a wet etch in chromic phosphoric acid at 60°C for 2 h. A second anodization step is performed again using 3% oxalic acid at ≈0°C with a 30 V bias until the entire aluminum layer is anodized through, making the sample transparent. This usually takes ≈14 min at which point the anodization current begins to rise and is allowed to reach ≈50 mA. The bias is subsequently decreased to 25, 20, and 15 V for durations of 1 min each. This step-wise decrease in voltage helps to thin the oxide barrier layer that exists at the bottom of the pores after anodization, exposing the underlying Au cathode. To further thin the barrier layer, a wet etch in 5% phosphoric acid is performed for 20 min at room temperature. This wet etch removes any remaining barrier layer while slightly widening the pores, giving us control of nanowire diameter and fill fraction.

Au nanowires are deposited in the pores of the template using DC electrodeposition with a gold electrolyte (prepared using 0.05 M $HAuCl_4$, 0.42 M Na_2SO_3, and 0.42 M $Na_2S_2O_3$) and a bias of ≈1 V [23], [47]. Au from the electrolyte begins to plate the pore bottom as the exposed Au thin film acts as a cathode. Nanowire length is controlled by the duration of deposition and can range from tens of nanometers to the entire length of the pore in the AAO thin film. Deposition for our samples was carried out for a total of roughly 1–2 min resulting in a nanowire length of approximately 400 nm.

Depending on the AAO film thickness and the nanowires length, there may be some over or under deposition, leaving excess gold on the surface of the template or a void at the top of the pore. To level off the surface of the sample, an ion milling dry etch is performed. This leaves a surface where the Au nanowires are flush with the AAO thin film.

The samples are also annealed for 2 h in an inert Ar atmosphere at 300°C [1]. This helps to increase the grain size of the metallic nanowires, allowing

the electrons to have longer mean free path and reduced Drude damping. Figure 2.3 is a schematic that outlines the complete process flow. All steps are included in the schematic other than the annealing step as annealing does not alter the structure of the device.
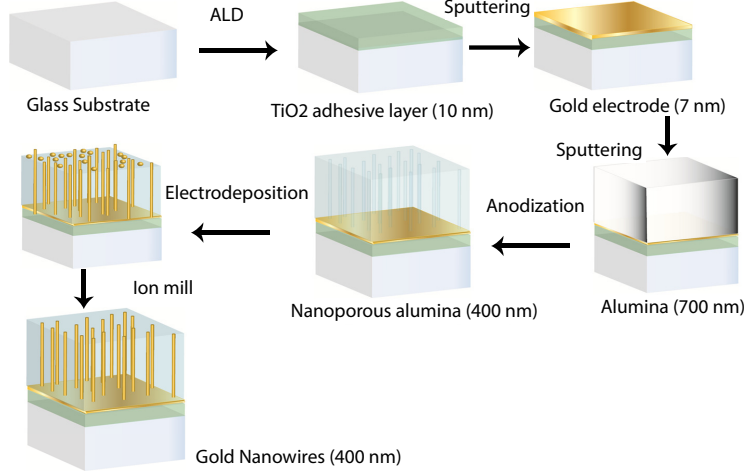
Figure 2.3: Schematic of process flow of device fabrication. Physical dimensions (diameter and length) and spacing of nanowires can be controlled by adjusting certain variables within the process flow. Our approach gives rise to large area uniform fabrication for the nanowire metamaterial.

2.4 Materials Characterization

To confirm the presence of Au nanowires, SEM, EDX, and XRD analyses are performed on the samples. Gold is chosen because it is an easy material to work with, it electrodeposits with a high yield of nanowires, does not oxidize easily, and has a dielectric response that is ideal for plasmonics in the visible spectrum. Figure 2.4 shows the pore ordering of the template surface. Using this image we can obtain values for pore diameter (d) and spacing (S) and calculate the metal fill fraction (ρ) using the following equation (assuming perfect hexagonal structure):

$$\rho = \frac{\pi d^2}{2\sqrt{3}S^2} \tag{2.4}$$

A more rigorous method to extract the fill fraction from the above SEM image was also done to confirm an accurate fill fraction. The image is run

through a code that outputs the ratio of "dark" pixels to "light" pixels. Given an accurate contrast threshold for the pore wall, "dark" pixels are defined as those pixels with a contrast below the boundary and represent the pore in the structure (where the metal is later deposited). Consequently, the "light" pixels are those with contrast above the threshold and represent the Al2O3 matrix. Figure 2.5 shows the gold nanowire array after the alumina matrix has been removed using a 1 mM NaOH wet etch. This wet etch can cause the nanowires to clump together in groups due to the surface tension of the drying rinse water, as seen in the top-view SEM micrograph image shown in figure 2.4 (a).
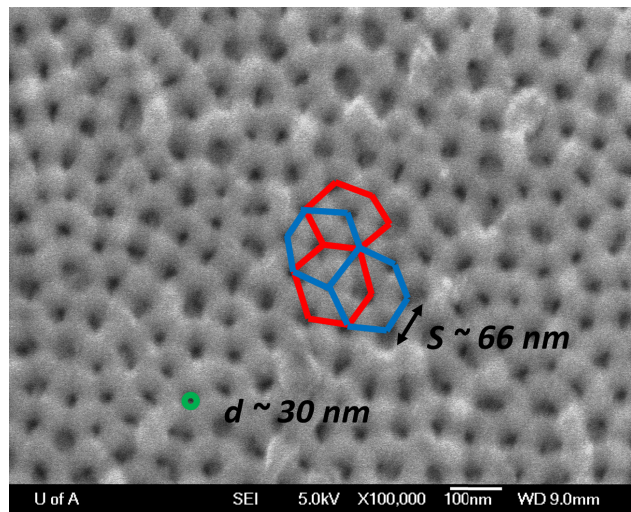
Figure 2.4: SEM image of AAO template quasi-hexagonal porous structure. Nanopore (and hence nanowire) diameter is approximately 30 nm; center to center pore spacing is approximately 66 nm. This produces a fill fraction of $\rho = 19\%$. The template parameters (pore diameter, pore spacing, ordering, film thickness) can be altered by adjusting the anodization parameters.

2.4.1 Energy Dispersive X-Ray Spectroscopy

EDX analysis of an AAO template with gold nanowires deposited in the pores is compared with that of a template with empty pores to show which peaks are arising from the background elements present in the sample's substrate and matrix and which peaks can be attributed to the gold nanowires. There are several peaks visible in both sample spectra [figure 2.6 (a)] which correspond

26
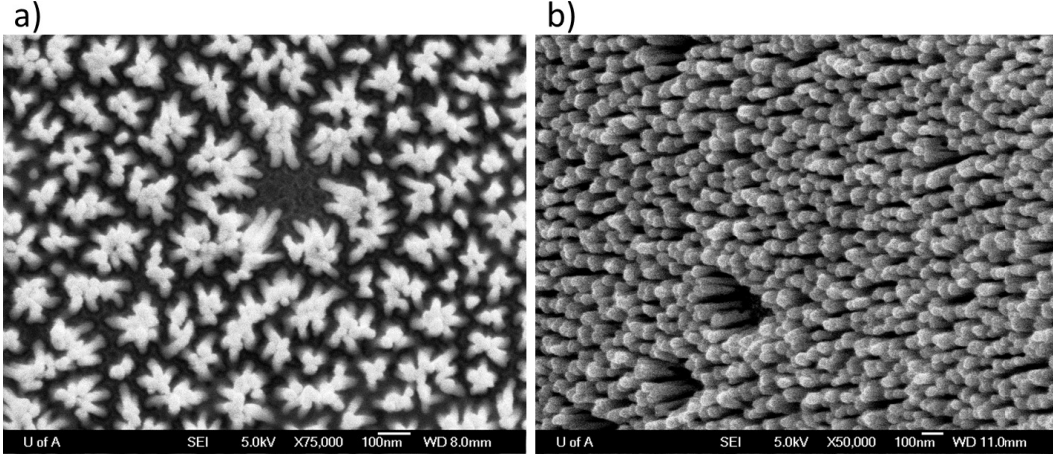
Figure 2.5: SEM images of (a) top down and (b) oblique views of Au nanowires grown in the pores of AAO templates. The AAO matrix has been removed in these images to view the nanowires, but is still present in the samples during transmission measurements. Because the template removal is done using a wet etch, the surface tension of the etchant/water pulls the nanowires together in to clumps as it dries. This is evident in (a) as the nanowires can be seen leaning on each other in groups.

to the elements Si, Ca, Na, Mg, K (the glass substrate is predominantly Si with contaminants of Ca, Na, Mg, K), Ti (an adhesion layer of TiO_2 exists under the Au thin film), and Cr (a few nanometers of Cr is sputtered on top of all samples prior to SEM to ensure samples are suitable for SEM and to prevent surface charging artifacts in SEM images). In figure 2.6 (a), we notice peaks present only in the gold nanowire sample at 2.1229 and at 9.7133 keV. These are the two main characteristic peaks for gold, which are a result of the $M_{\alpha 1}$ and $L_{\alpha 1}$ electron transmission lines, respectively [48].

2.4.2   X-Ray Diffraction Analysis

To improve the optical properties of the gold nanowire arrays we investigated the effects of annealing on the crystallinity of the gold NWs. XRD was performed on samples prior to and after annealing. Gold peaks are observed in all samples for the (111), (200), (220), (311), (222), and (400) crystal planes [figure 2.6 (b)]. Annealing has reduced the FWHM values of all Au plane peaks, as shown in figure 2.6 (b). This suggests an increase in the overall grain size of the nanowires resulting in a larger mean free path of conduction

27
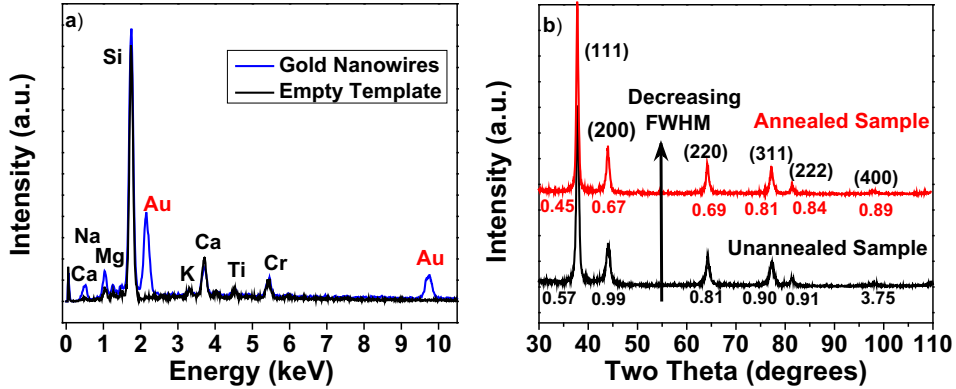
Figure 2.6: (a) Energy dispersive x-ray analysis of empty template versus gold nanowire-filled template. Peaks corresponding to the elements Si (primary element in glass), Ca (glass impurity), Na (glass impurity), Mg (glass impurity), K (glass impurity), Ti (present in TiO_2 adhesion layer), and Cr (few nanometer conductive layer deposited on all samples for SEM imaging) are observed in both samples. Only in the gold nanowire sample spectrum are peaks observed at 2.1229 and 9.7133 keV, which correspond to the $M_{\alpha 1}$ and $L_{\alpha 1}$ electron transmission lines, respectively, the characteristic lines of gold. (b) X-ray diffraction pattern of gold nanowire samples before and after annealing. FWHM values are presented directly below each peak. Note that the FWHM value is larger prior to the annealing step for each individual peak.

electrons. A larger electron mean free path allows for lower optical losses. This ultimately leads to more efficient plasmon generation and higher-quality factor resonances in the nanowires.

2.5 Experimental Results

Angular transmission spectroscopy is performed on several samples with fill fractions ranging from 10.5% to 26% using an Ocean Optics fiber optic spectrometer and linearly polarized white light. Within the extinction spectra, two features can be observed in every sample (figure 2.7). One absorption peak, located at ≈530 nm, is attributed to the ENP resonance and another absorption peak, which is highly tunable in a range from 583 to 805 nm, is attributed to the ENZ resonance. These two absorption resonances are the result of localized plasmon polariton resonances supported by the NW structure. The ENP, also known as the transverse electric (TE) mode, is omnidirectional and

its location is generally dependent on the materials used, although it is also very weakly dependent on the fill fraction. This is reflected in figure 2.7 as well as figure 2.8 (b). Both show an ENP in the range of $\approx 530 \pm 10$ nm that is fixed in wavelength for any given angle of incident light. The TE mode is a plasmonic mode with resonant electron motion perpendicular to the nanowire axis and therefore is excited by both (s) and (p)-polarized light [21].
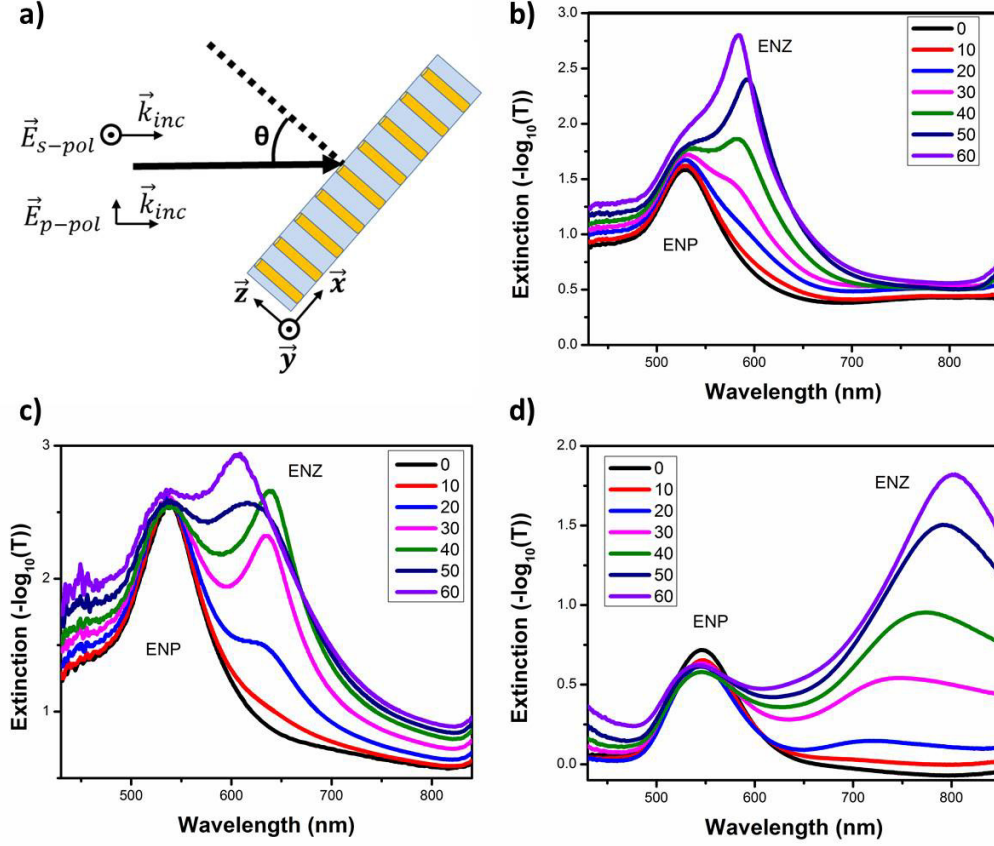
Figure 2.7: (a) Experimental setup showing how the extinction of our samples was measured. p-polarized light is defined as light with a maximum E-field perpendicular to the metasurface [z direction in (a)] for a given angle while s-polarized light has its E-Field in the plane of the metasurface [xy-plane in (a)] at all angles. (b)–(d) The experimental extinction spectra for p-polarized light of a gold nanowire system with fill fraction (b) 26%, (c) 23%, and (d) 10.5%. The ENP resonance is the shorter wavelength resonance for all three samples and occurs at $\lambda_{ENP} \approx 530 \pm 10$ nm. The ENZ extinction increases in intensity with an increase in incident angle from 0° to 60°. The location of the ENZ resonance shifts to longer wavelengths when we decrease the fill fraction from (b) $\lambda_{ENZ} \approx 583$ nm to (c) $\lambda_{ENZ} \approx 664$ nm to (d) $\lambda_{ENZ} \approx 805$ nm.

29

The second absorption peak, located at the ENZ point, is known as the transverse magnetic (TM) mode. Contrary to the TE mode, the excitation efficiency of the TM mode is angularly dependent and highly sensitive to the fill fraction as well as the materials used. Also, this resonance is only present in the absorption spectra using p-polarized light and does not exist for s-polarized light. The TM mode is a plasmonic mode with electron motion parallel to the nanowire axis [21], [49]. As the incident angle of light increases [measured from the normal as θ in figure 2.7 (a)], so does the amplitude of the absorption peak. The growing electric field vector parallel to the nanowire axis with increasing angle is the cause of this angularly dependent behavior. Using Au/Al_2O_3 nanowire arrays as has been fabricated in this report, the TM mode can be tuned from 583 nm (corresponding to a fill fraction of 26%) to 805 nm (corresponding to a fill fraction of 10.5%). Beyond the ENZ resonance wavelength the dielectric component ε_{zz} becomes negative and the sample is hyperbolic. This forms the best approach to characterize the NW metamaterial with hyperbolic dispersion.

Scattering is one major source of uncertainty in extinction measurements as it is difficult to determine what fraction of the total power is being absorbed as opposed to scattered by the metamaterial. In an effort to remove scattering effects from our measurements, we have plotted T_p/T_s [figure 2.8 (a)], which allows scattering effects to be canceled out as they are expected to affect s and p-polarizations equally. We see a good agreement between CST simulations and our experimental data.

The ENZ and ENP points for the samples plotted in figure 2.7 (b)-(d) are shown in figure 2.8 (b) along with the theoretical ENZ and ENP curves predicted by EMT [equations (2.2 2.1)]. It is shown that the experimental and theoretical ENP resonances are very weakly dependent on the fill fraction values. Although it is stated earlier that this is only valid for $\rho \ll 1$ we can see that experimentally this holds true for much larger values of ρ. Alternatively, the ENZ point varies drastically along with the fill fraction and can be tuned within the range of 583-805 nm. Furthermore, within each ENZ point, a shifting of the ENZ resonance occurs as the angle of incident light is increased
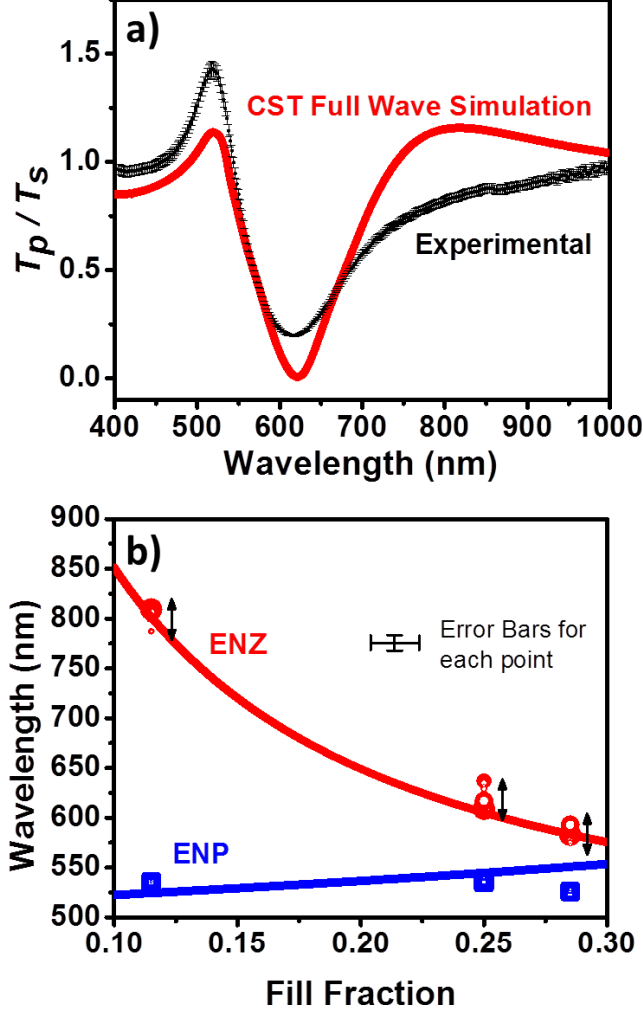
Figure 2.8: (a) *p*-polarized transmittance divided by *s*-polarized transmittance from experiment and CST simulation at 30° incidence. In experiment the surface roughness always leads to scattering thus usually lower transmittance. By comparing the transmittance ratio we can greatly reduce the scattering effect from optical measurement. The agreement between experiment and CST further confirms the experimental realization of nanowire metamaterial. (b) Varying sized data points show experimental ENZ and ENP resonant wavelength's dependence on fill fraction and angle. The ENP resonance stays at a relatively fixed wavelength ($\approx 530 \pm 10$ nm) for multiple fill fractions, whereas the ENZ resonance can shift dramatically from ≈ 583 nm all the way to ≈ 805 nm for changing fill fractions. Data points are plotted for angles from $10^{/circ}$ to 60° (symbol size is proportional to angle value) showing the spatial dispersion effect of the ENZ resonance. Solid lines show the theoretical location of the ENZ and ENP resonances as a function of fill fraction predicted using EMT [equations (2.2 2.1)].

31

[larger symbols in figure 2.8 (b)] and corresponds to larger incident angles. The slight shift in peak wavelength of the plasmonic resonances is due to the interplay of competing effects of material loss and nonlocality. This will be addressed in future work. An overview of nonlocal effects can be found in [21]. Note the ENZ resonances are only present for p-polarized light. In stark contrast, the ENP resonance does not show within experimental uncertainty any spatial dispersion effects and has a fixed wavelength for varying angles of incident light.

2.6   Conclusion

We have contrasted the behavior of the omnidirectional and fixed wavelength ENP resonance with the angularly dependent and tunable ENZ resonance. While the ENP resonance remains at a wavelength of $\approx$540 nm in all samples, the ENZ resonance is highly dependent on the fill fraction of metal nanowire (ρ) and can be designed to exist in the range from $\approx$583 to 805 nm, corresponding to fill fractions of $\approx 26\% - 10.5\%$, respectively. We have distinguished the different structure and behavior of NW metamaterials from that of ML metamaterials and our experimental results agree with EMT and CST simulations. Future work will explore quantum, thermal, and biosensing applications of such nanowire arrays.

Chapter 3

Dual-Band Quasi-Coherent Radiative Thermal Source

Thermal radiation from an unpatterned object is similar to that of a gray body. The thermal emission is insensitive to polarization, shows only Lambertian angular dependence, and is well modeled as the product of the black-body distribution and a scalar emissivity over large frequency bands. Here, we design, fabricate and experimentally characterize the spectral, polarization, angular and temperature dependence of a microstructured SiC dual band thermal infrared source; achieving independent control of the frequency and polarization of thermal radiation in two spectral bands. The measured emission of the device in the Reststrahlen band (10.3-12.7 μm) selectively approaches that of a black-body, peaking at an emissivity of 0.85 at $\lambda_x = 11.75$ μm and 0.81 at $\lambda_y = 12.25$ μm. This effect arises due to the thermally excited phonon polaritons in silicon carbide. The control of thermal emission properties exhibited by the design is well suited for applications requiring infrared sources, gas or temperature sensors and nanoscale heat transfer. Our work paves the way for future silicon carbide based thermal metasurfaces.

3.1   Introduction

Thermally excited light is traditionally thought of as being incoherent, unpolarized and spectrally broad. These notions have been challenged in the past decade to overcome incoherent properties of thermal radiation sources.

Many different approaches have been used to engineer the spectrum [2], [3], [50], coherence [6], [51], polarization [51], [52] and directionality properties [6], [51], [53] of thermally emitted radiation. Proper design of ruled gratings in metals [11], [53], [54] or polar dielectrics [6] have been successfully employed to couple thermally excited surface waves into far-field thermal radiation. A selection of studies have also built on this concept to generate beamed thermal emission from 2D gratings [8], [51], [52], [55]. Another popular design for controlled thermal emission is the use of photonic crystals patterned in to metals or polar dielectrics [56].

The control of a material's epsilon-near-zero (ENZ) and optical topological transition characteristics has also proven to be a promising route for thermal emission engineering [3], [22], [50], [57]. Plasma frequency tunable materials such as aluminum zinc oxide (AZO) or gallium zinc oxide (GZO) can provide a platform for implementation of this idea [22], [50]. Intriguingly, a single thin layer of epsilon-near-zero material can function as a spectrally selective thermal emitter without the need for any nanostructuring. Multilayer thermal metamaterial designs have also experimentally demonstrated that thermal radiation can be controlled by engineering the optical topological transition [3]. Such advances in thermal radiation control can impact a variety of commercial applications such as coherent infrared sources [6], [51], [58], [59], thermophoto-voltaics [7], [8], [22], [54], [60], radiative cooling [9], [61], temperature sensors, gas sensors [62], nanoscale heat transfer [63]–[66] and general thermal management.

Designs that exhibit dual band emission are also of interest and several studies towards this type of emission pattern have been published [2], [55]. By designing emitters to have multi-band emission, we can increase functionality of the device for certain applications (e.g. sensing) by dedicating each emission band to perform a specific function. Despite the potential benefits of dual band emitters, all current designs have been limited to metallic structures and few have been experimentally demonstrated [2], [55]. Furthermore, these demonstrations do not simultaneously control all emitter properties (spectrum, polarization, directionality, coherence) necessary for multiplexing of thermal

signals.

In this article, we design, fabricate and experimentally demonstrate a 2D bi-periodic SiC grating infrared source with orthogonally polarized, angularly coherent, dual band thermal emission in the mid-IR regime. We present a comprehensive experimental study of the thermal properties of this device by characterizing the spectral, polarization, angular, and temperature dependence of its thermal emission. The polarized emissivity spectrum is measured as both a function of temperature and emission angle within the Reststrahlen band of semi-insulating 6H-SiC (10.3-12.7 μm). Two emission bands, termed λ_x and λ_y, are observed at normal incidence. This effect fundamentally arises due to thermally excited phonon polaritons in silicon carbide. The peak emissivity achieved for λ_x and λ_y are 0.85 and 0.81 respectively. The main emission peaks of each band shows an angular dependence, red shifting at higher emittance angles. A red shift of the emission peaks is also observed with increasing temperatures. The peak of the λ_x band shifts by 70 nm over a 255 K temperature change, while the peak of the λ_y band shifts by 60 nm over a temperature change of 259 K. Using a temperature dependent Drude model of SiC [67] in rigorous coupled wave analysis (RCWA) numerical simulations, strong agreement with our measurements is observed.

3.2 Design, Fabrication and Characterization of Structure

3.2.1 Surface Phonon Polaritons in Polar Dielectrics

Polar dielectric materials possess a spectral region known as the Reststrahlen band where a negative ε' (ε' is the real part of the complex dielectric permittivity) leads to metal-like behavior with high reflectivity. This region exists between the transverse (TO) and longitudinal optical (LO) phonons where polar lattice vibrations (phonon-polaritons) act to effectively screen electromagnetic waves, leading to high reflectivity analogous to a metal. Within the Reststrahlen band, coupled photonic-phononic surface waves, called surface phonon polaritons (SPhP), are supported, due to the interface between neg-

ative ε' and positive ε' materials [68]. By attaching a piece of this material to a thermal bath (in our case a substrate heater), we can thermally populate these surface waves. Since the SPhP has a well defined dispersion relation, this provides a unique opportunity to engineer thermal emission in the Reststrahlen region in to well defined angular direction and spectral bands. SiC is one such polar dielectric that has been a popular choice for engineering thermal emission due to its high thermal stability (up to 3000 K) and its ability to support SPhP waves.

3.2.2 Design of Bi-Periodic Grating

Previous works have shown that the SPhP of SiC can be thermally excited and efficiently coupled to free space using 1D and 2D gratings [6], [51]. Here, we have designed and fabricated a bi-periodic grating to couple the thermally excited SPhP of SiC in to two bands of far-field propagating waves. The center wavelength of each emission peak can be independently tuned by modifying the x or y directions grating period as defined in figure 3.1 a). The structure is engineered such that each grating period (Λ_x and Λ_y) will efficiently couple the SPhP in to a single band of emission ($\lambda_x = 11.75 \ \mu m$ and $\lambda_y = 12.25 \ \mu m$) that propagates with a k-vector normal to the surface ($\theta = 0$ as defined in figure 3.1 a)). Because surface waves are by nature p-polarized, the two engineered emission bands are orthogonally polarized in the far-field, providing an additional degree of discrimination.

Figure 3.1 b) shows the real and imaginary permittivity of SiC, calculated using a Lorentz model [51] with the Reststrahlen band highlighted by the shaded region. On top of this we have plotted the measured emissivity of a bare SiC wafer at 1000 K (0.3 mm thick). Within the Reststrahlen band, low emissivity is indeed observed. This result supports Kirchoff's law as one would expect to see a high reflectivity here.

To calculate the emissivity spectrum in figure 3.1 b) (as well as emissivity spectra in later figures), the following approach was used from reference [69]:

$$\epsilon(\lambda, \theta, T_S) = \left[\frac{S_S(\lambda, \theta, T_S) - S_R(\lambda, T_R)}{S_B(\lambda, T_B) - S_R(\lambda, T_R)} \right] \left[\frac{L(\lambda, T_B) - L(\lambda, T_R)}{L(\lambda, T_S) - L(\lambda, T_R)} \right] \quad (3.1)$$

where S_S is the sample spectrum, T_S is the temperature of the sample, S_B is the spectrum of the black-body calibration source, T_B is the temperature of the black-body calibration source, S_R is the background spectrum at room temperature, T_R is room temperature and $L(\lambda, T)$ is Planck's law at temperature T.

3.2.3 Kirchoffs Law and Reflectivity/Emissivity Calculation

According to Kirchoff's law of thermal radiation, a body that is in thermal equilibrium with its environment must have $\epsilon(\lambda, \theta) = \alpha(\lambda, \theta)$ where $\epsilon(\lambda, \theta)$ is the emissivity spectrum and $\alpha(\lambda, \theta)$ is the absorptivity spectrum of the material. It follows that if we are considering a material that is optically thick (transmission $= 0$) we can calculate the emissivity of a material as $\epsilon(\lambda, \theta) = 1 - R(\lambda, \theta)$, where $R(\lambda, \theta)$ is the reflectivity spectrum. For typical polar materials, such as SiC, this condition is met for thicknesses greater than about 100 μm [70].

The permittivity function of a polar dielectric material is commonly modeled as a Lorentz oscillator [6]. However, it is known that at elevated temperatures the dielectric function of SiC changes. Here, we take in to account the changes in this material property at elevated temperatures by using a modified Drude model described by Hervé et al. [67].

$$\varepsilon(\omega) = \varepsilon_\infty \left[1 - \frac{\Omega_p^2}{\omega(\omega + i\gamma_p)} \right] + \frac{S\Omega^2}{\Omega^2 - \omega^2 - 2\Omega \sum_{j=1}^n [\Delta_j(\omega) + i\Gamma_j(\omega)]} \quad (3.2)$$

This model consists of two pieces: a high frequency contribution, ε_∞ multiplied by a Drude term, with Ω_p acting as the plasma wavenumber, and γ_p the Drude damping factor; and a phonon term [71] with S denoting the oscillator strength, Ω the wavenumber of the bare resonance frequency and $\sum[\Delta + i\Gamma]$ the self energy contribution. For simulations presented in this study, we have

37
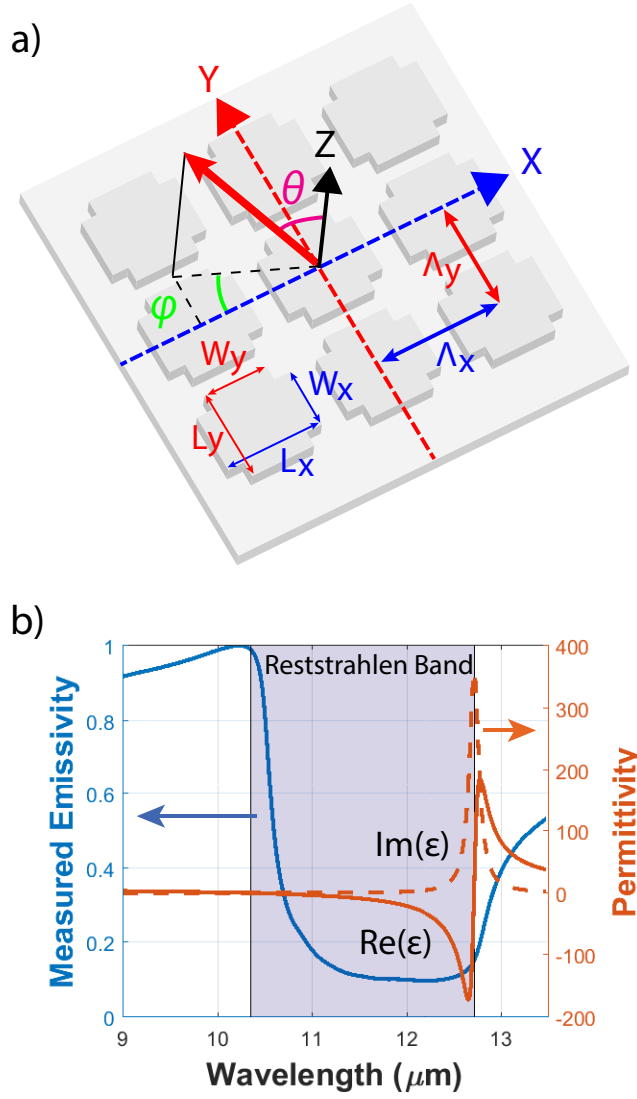
Figure 3.1: a) Schematic of sample with axes, grating periods and emission angles defined. b) Real (solid red) and imaginary (dashed red) dielectric functions are plotted with the Reststrahlen band shaded. The blue curve shows measured emissivity at normal angle of emission of a bare SiC wafer. A low emissivity spectrum within the Reststrahlen band suggests high reflectivity, supporting the approximation $\epsilon(\lambda) = \alpha(\lambda) = 1 - R(\lambda)$.

taken constants from ref. [67] at 996 K to compute the permittivity near our typical operating temperature.

The two grating periods are designed such that the SPhP is coupled in to two directional emission bands almost normal to the surface. The two emission bands center wavelength of $\lambda_x = 11.75\ \mu m$ and $\lambda_y = 12.25\ \mu m$ are chosen so that they lie in the middle of the Reststrahlen band. We use RCWA

simulations with the above dispersion relation to simulate the reflectivity of our design and determine the grating periods of $\Lambda_x = 9.6 \ \mu m$ and $\Lambda_y = 11.5 \ \mu m$ that are required to achieve the designed emission pattern. Furthermore, the dimensions W_x, W_y, L_x and L_y (as labeled in figure 3.1 a)) of the cross structure within the bi-periodic grating are optimized for efficient coupling of SPhP to achieve the maximum possible peak emissivities.

3.2.4 Fabrication and Characterization

V-doped semi-insulating 6H-SiC wafers were purchased from Xiamen Power-way Advanced Material. Figure 3.2 a) shows a conventional lift off process flow used to fabricate the nickel mask for device fabrication. First, a 400 nm thick layer of PMMA A4 resist is spun on the SiC wafer and pre-baked at 180°C for 90 s. Then, the resist layer is patterned by an electron-beam lithography (EBL) system and developed in a MIBK:IPA (1:3) solution for 1 min. Next, a 100 nm thick Ni metal film is deposited on the wafer using electron beam evaporation and a lift-off process is implemented using acetone as the solvent. The SiC wafer is then dry etched 700 nm deep using an SF6-based chemistry, creating a grating in the wafer. Finally, the Ni hard mask layer is removed by Piranha solution and the final structure is obtained. Figure 3.2 b) is an SEM of the final structure from a normal view.

3.3 Emissivity Measurements

The emissivity spectrum of our structure is directly measured through thermal emission measurements. The signal is generated by controlled heating of the device on a substrate heater in vacuum. Detection is performed using a Thermo Scientific Nicolet is50 fourier transform infrared (FTIR) spectrometer. The measurement methods and results are described below.

3.3.1 Experimental Thermal Emission Measurements

Thermal emission measurements are taken by collecting the temperature (T) and angular (θ) dependent emission signal of the patterned SiC wafer. The
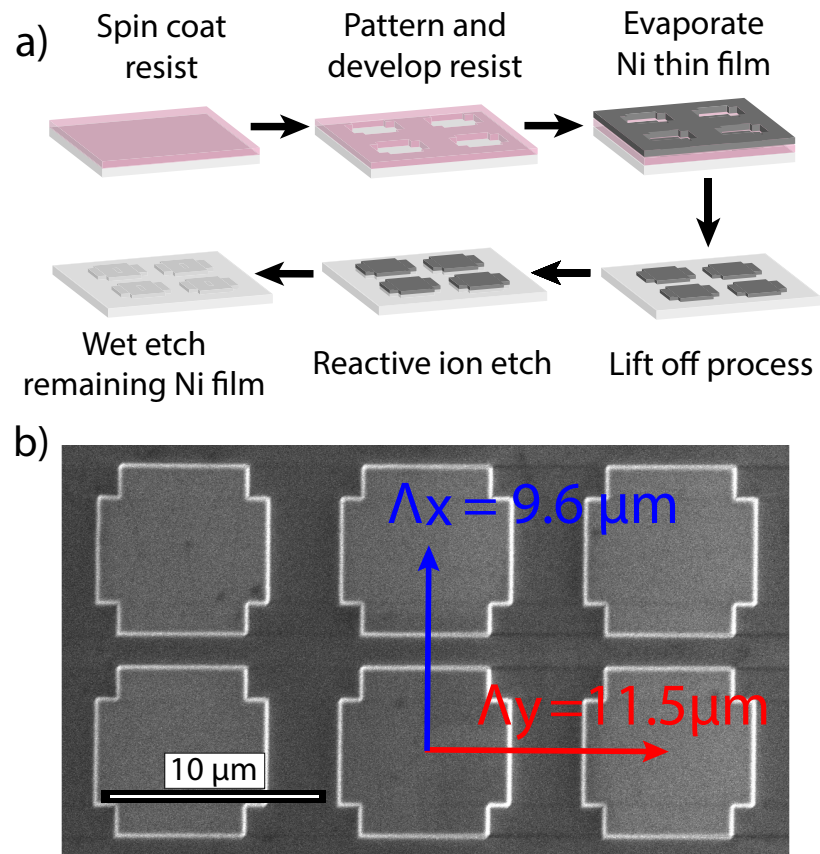
Figure 3.2: a) Lift off process flow used to pattern bi-periodic grating in SiC. b) SEM image of final patterned structure with Λ_x and Λ_y periods labeled.

emitter is attached to a high temperature substrate heater inside a custom built vacuum chamber and heated to temperatures from 689 to 963 K under vacuum (10^{-7} mbarr). The emission signal is sent through a ZnSe window to allow for ex situ analysis and detection. Once the signal exits the chamber, its propagation path is confined to a nitrogen purged environment to reduce atmospheric absorption. The experimental set up is shown in figure 3.3.
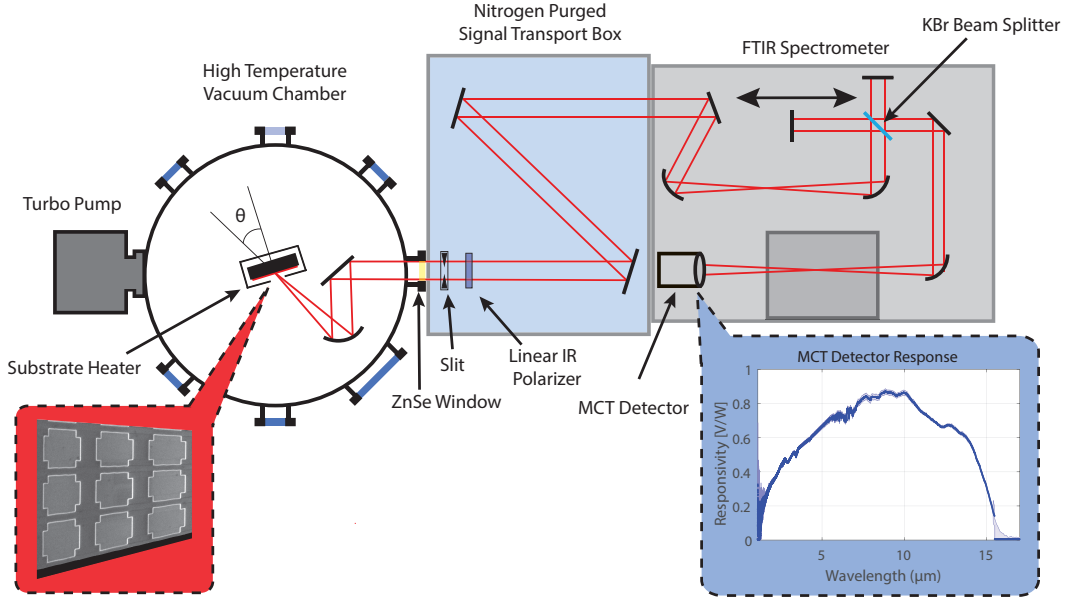
Figure 3.3: Schematic of Experimental set up. Patterned sample is placed on the substrate heater inside the vacuum chamber. Emission signal is collected with a 4" focal length parabolic mirror and is directed out of the chamber through a ZnSe window. A nitrogen purged signal transport box couples the signal in to the FTIR with proper alignment while housing optical analyzing elements (slits, polarizers etc.). For emissivity measurements from this structure, a MCT detector is typically used for high sensitivity in this spectral region.

After exiting the chamber, the signal passes through a slit to isolate the planar emission from one grating period (Λ_x or Λ_y) at a time. The signal is then polarized using a KRS-5 wire grid linear polarizer. The combination of these two optical elements allows us to isolate s or p polarized light originating from either grating period of the structure. The slit is 22.86 mm long and 3 mm wide. With the collimating parabolic lens placed at its focal focal distance of 101.6 mm (4"), this corresponds to a collection angle of 12.8°

41

and 1.7° respectively. For these measurements the FTIR spectrometer uses a KBr beam splitter and a mercury cadmium telluride (MCT) detector. The combined responsivity of the detection method spans the range of 1.4-16.7 μm and is shown in figure 3.3. Measured spectra is averaged over 32 scans with a data spacing of 0.48 cm^{-1}.

To accurately determine the temperature of the emitter, we use the Christiansen wavelength method [70]. The Christiansen wavelength is a particular point in polar dielectric materials where there is a low extinction coefficient and the refractive index is 1. At this wavelength, there is a low impedance with free space so the reflectivity tends to 0. If the material is sufficiently thick such that the transmission is also 0 (as in this case), then it follows that absorptivity tends to 1. One can then justify, using Kirchoff's law of thermodynamics, that emissivity tends to 1 and at the Christiansen wavelength the material behaves like a black body. The emission of the device at this wavelength can be compared to Planck's law to accurately determine the temperature of operation. For SiC this occurs at 10.1 μm [51].

Figure 3.4 shows the experimentally measured p-polarized emissivity of the SiC device at 963 K and $\theta = 0°$ and its agreement with RCWA numerical simulations. Indeed we see two emission bands at $\lambda_x = 11.75$ μm and $\lambda_y = 12.25$ μm. Of note is a second shoulder peak present in the emission spectrum of the λ_y band. This shoulder peak results from the first order diffraction of the SPhP traveling in the opposite direction $(-\vec{k}_{SPhP})$. Figure 3.5 a) shows the temperature dependent p-polarized emission spectra resulting from the Λ_x grating period ($\phi = 0°$). A shift of 70 nm in the peak wavelength is observed over a temperature change from 708 to 963 K. Figure 3.5 b) shows the temperature dependent p-polarized emission resulting from the Λ_y grating period ($\phi = 90°$). A shift of 60 nm in the peak wavelength is observed for a temperature change from 689 to 948 K. This is consistent with previous studies and the temperature dependence of emission from SiC based grating structures is discussed in detail by Hervé et al. [67].
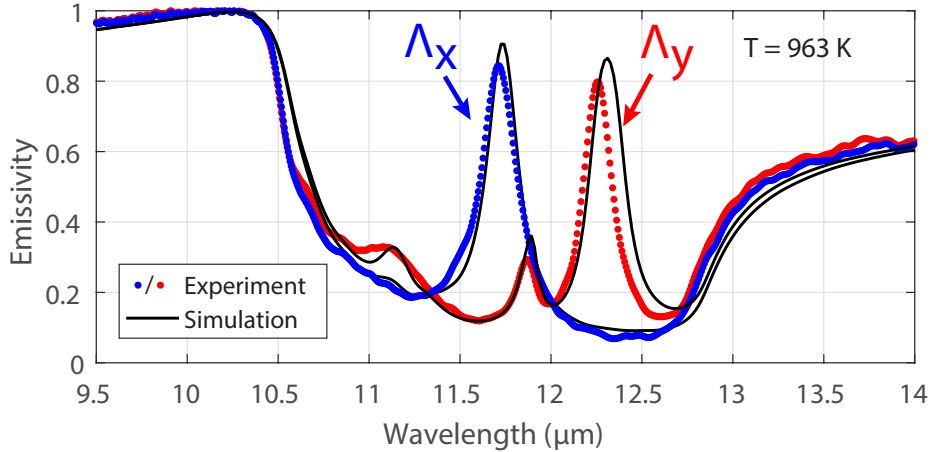
Figure 3.4: Experimental (dot) vs simulated (line) p-polarized emissivity Spectrum of patterned SiC bi-periodic grating taken at normal angle of emission. The first peak located at 11.75 μm is due to $\Lambda_x = 9.6$ μm while the second emission peak located at 12.25 μm is due to $\Lambda_y = 11.5$ μm.

3.3.2 Angularly Dependent Emission Spectra

To further confirm the behavior of our bi-periodic grating design, angularly resolved numerical simulations are performed and compared to experiment. The simulated spectrum as a function of emission angle (θ) is presented in figure 3.6 a)-d) where the 4 permutations of polarization (s or p) and grating period (Λ_x or Λ_y) are shown separately. We can see that for a normal angle of emission ($\theta = 0°$) in figures 3.6 a) and b), there exists a high emissivity peak at 11.75 μm and 12.25 μm for p-polarized waves (the polarization for which this structure was designed to have high efficiency coupling between SPhP and free space propagating waves).

Figures 3.6 c) and d) shows that there exists a high emissivity peak for s-polarized waves. While our emitter is not designed to have such an emission pattern, it can be explained by out of plane scattering of SPhPs. Once a p-polarized surface wave is scattered to any wavevector that is not in the plane defined by the grating vector and the surface normal vector, a portion of it will then be s-polarized. This is common when coupling surface waves to free space and has been reported in previous studies [4], [51].

Figure 3.6 e)-h) shows the measured angularly resolved emissivity mea-

43
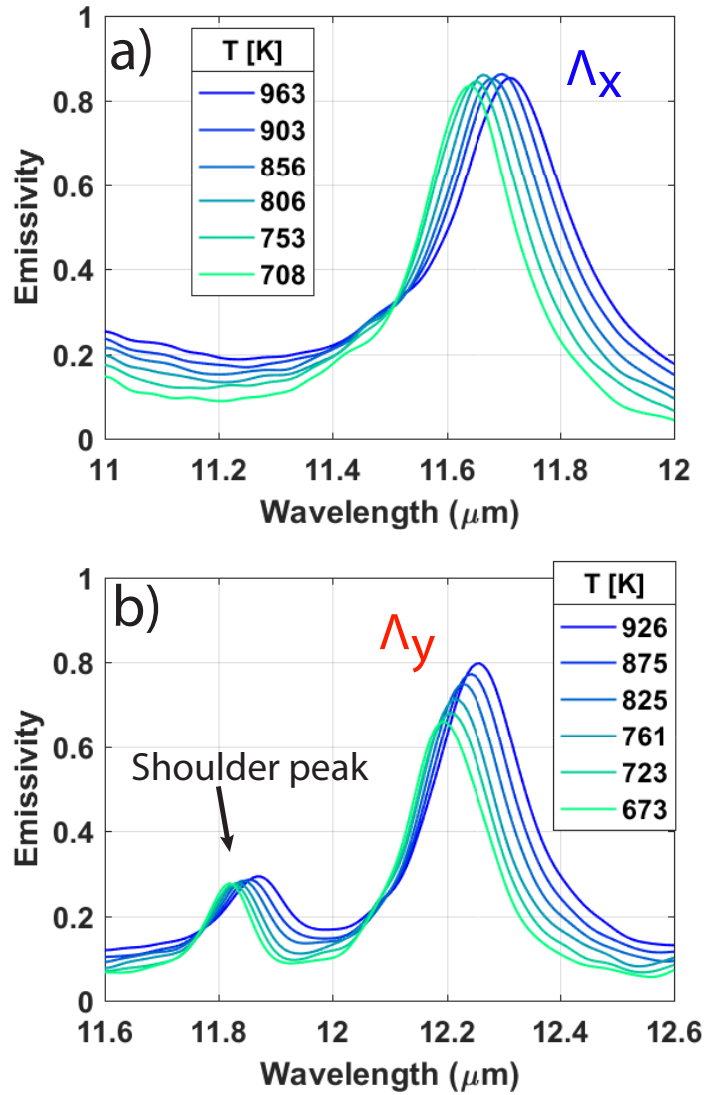
Figure 3.5: a) Temperature dependent emission spectrum of the p-polarized λ_x emission band. b) Temperature dependent emission spectrum of the p-polarized λ_y emission band.

surements. Measurements were taken at every 1° from 0°-40° with an angular resolution of 1.7°. For the two p-polarized cases figures 3.6 e) and f), we see an extremely good agreement between simulation and experiment. The main peak in the p-polarized emission is observed to shift to longer wavelengths at higher angles of emission (θ). This can be attributed to the fact that the SPhP needs a larger angle (θ) to be properly phase matched with free space propagating waves as described by the typical grating law:

44

$$\vec{k}_{SPhP} = \frac{\omega}{c} sin(\theta) - \frac{2\pi m}{\Lambda} \qquad (3.3)$$

where $\vec{k}_{SPhP}$ is the SPhP wave vector, m is the diffraction order integer ($m = \pm1, \pm2, ...$), Λ is the grating period, ω is the angular frequency and θ is the angle from the surface normal.

Additionally, there is good agreement between the experimental angular dependence of s-polarized emission and their theoretical simulations as shown in figures 3.6 g) and h). However, unlike the p-polarized case, the wavelength of this emission peak is not highly dependent on θ. This is to be expected as the origin of this emission peak lies in the out of plane emission originating from the grating period orthogonal to the one being measured (grating period of $\phi = 0$ when $\phi = 90$ is being measured). For this reason, there is no θ dependence as described in equation (3.3).

Of note is some disagreement between simulation and experiment for the s-polarized case of Λ_x. This discrepancy can be attributed to the use of a slit for isolation of emission angles. In this particular case, the length of the slit is aligned along the Y period, allowing a large angular spread (12.8°) of emission through the slit. This allows emission from the λ_y shoulder peak to be detected as we can see it present in figure 3.6 g). This is not present in simulations as they are performed at precise angles and do not account for the finite window of angles being detected. Furthermore, because the main p-polarized λ_y peak is highly sensitive to small changes at low θ angles, this leads to a reduced observed magnitude of the main peak (12.25 μm at $\theta=0°$) in figure 3.6 g).

3.4   Conclusion

We have successfully engineered a dual-band thermal emitter within the Reststrahlen region of semi-insulating SiC. The two spectral peaks are produced by coupling the SPhP in to free space propagating waves using a bi-periodic grating structure. We have fully characterized thermal emission from the device by analyzing its polarization, spectrum, angular emission pattern and tem-
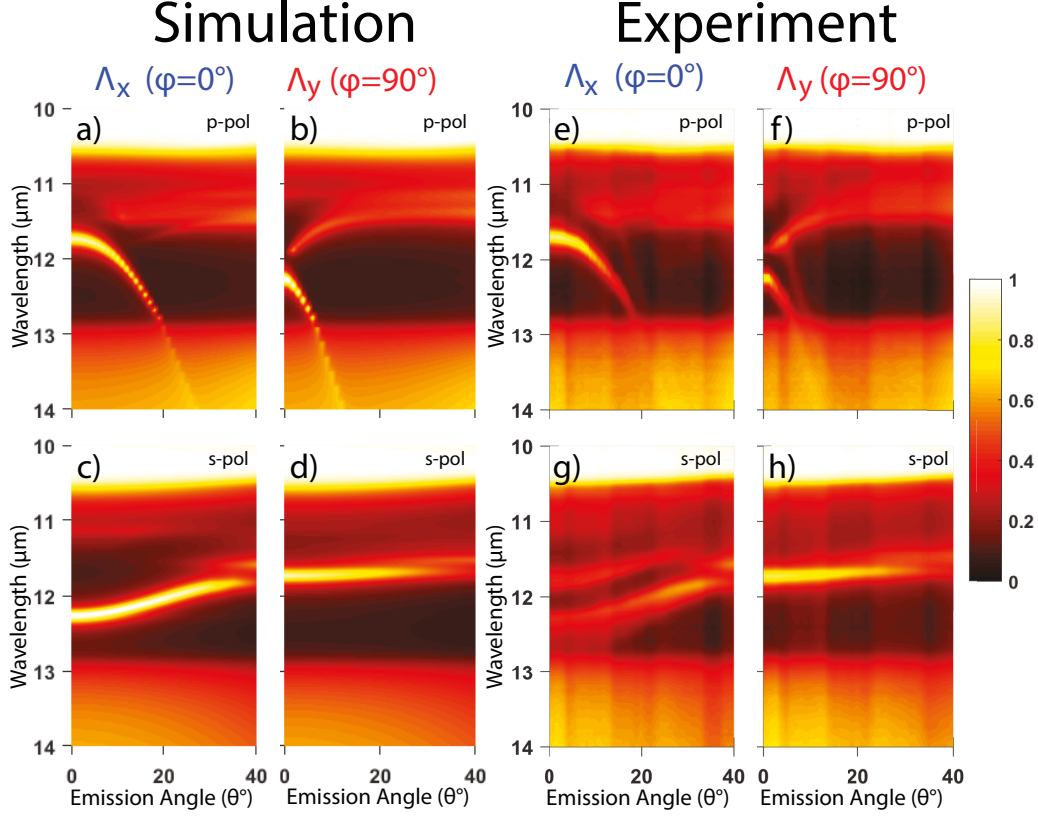
Figure 3.6: a)-d) Simulated angular absorption/emission spectra of p-polarized (a) and b)) and s-polarized waves (c) and d)). Figures a) and c) are for emission that is propagating in the x-z plane ($\varphi = 0°$) and figures b) and d) are for emission that is propagating in the y-z plane ($\varphi = 90°$). RCWA numerical analysis is used to generate these simulations. e)-h) Experimental angular emissivity spectra of p-polarized (e) and f)) and s-polarized (g) and h)) waves. Figures e) and g) are for emission that is propagating in the x-z plane ($\varphi = 0°$) and figures f) and h) are for emission that is propagating in the y-z plane ($\varphi = 90°$).

perature dependence. The center wavelength of the orthogonally polarized emission peaks can be independently controlled by adjusting the two grating periods. We have directly measured the the emissivity spectrum of the device through thermal emission measurements in vacuum and show that an emissivity of 0.85 is achieved for the $\lambda_x = 11.75$ μm band and 0.81 for the $\lambda_y = 12.25$ μm band. Our measurements are compared to RCWA numerical simulations and show they are in agreement when the temperature dependent material permittivity is accounted for.

While this study reports on a SiC based device to exploit it's SPhP, the

design principles can be easily transferred to metallic systems with surface plasmon-polaritons or other materials supporting surface waves.

Chapter 4

Direct Measurement of Thermal Emission from Polaritonic Particles

Thermal emission of disordered SiO_2 and SiC polaritonic particles is directly measured by thermally exciting their localized surface phonon polariton modes. We show that strong, near black-body emission can be achieved ($\epsilon = 0.9$ for 1 μm SiO_2 μ-spheres and $\epsilon = 0.8$ for 2 μm SiC particles). Emissivity spectra of the polaritonic particle systems are compared to extinction spectra (from transmission measurements) as well as simulations from Mie theory and show strong agreement. We also discuss how this metrology technique can be used to indirectly measure the absorption spectrum of arrays of subwavelength particles. These results demonstrate broad applicability in fields such as passive radiative cooling, thermal infrared sources and astronomical spectroscopy.

4.1   Introduction

The efficiency with which sub-wavelength particles scatter electromagnetic (EM) radiation is highly dependent on particle size and shape and is well described by Mie theory [20]. Additionally, if they are made of polaritonic materials, these sub-wavelength features will couple radiation to their polaritonic modes, leading to enhanced absorption efficiency. Metallic particles are good candidates when engineering interaction in the ultraviolet (UV) [72], visible [73] and near infrared (NIR) [74] frequency ranges due to the plasmon

energies of metals like Au and Ag. For infrared frequencies, phonon polaritonic materials such as SiC, SiO$_2$ or hBN provide optical phonons that are also able to couple to mid-IR radiation.

When photons interact with sub-wavelength particles, it becomes difficult to detect a scattered photon due to the probabilistic nature of scattering events (figure 4.1 a)). For this reason, true absorption spectroscopy necessitates the use of an integrating sphere. However, we know that for systems in thermal equillibrium, Kirchoff's law states that the linear angular absorptivity spectrum is equal to the angular emissivity spectrum ($\alpha(\lambda) = \epsilon(\lambda)$). Using this relation, we can indirectly measure the absorption spectrum through thermal emission measurements. With thermal emission measurements, radiation originates from the particle (or other emitting system) and propogates to your detector without experiencing a scattering event (figure 4.1 b)). This allows us to separate the emissivity/absorptivity spectrum from the scattered spectrum. Thermal emission from subwavelength particles has seen a spark in interest due to potential applications like narrowband IR sources [68], thermal antennas [12], passive radiative cooling [10], [75], [76] and astronomical spectroscopy due to the formation of SiC particles in carbon rich stars [77]. More broadly, thermal emission from other nanostructures such as photonic crystals [56], [78], [79], gratings [6], [51], [80] and metamaterials [3], [22], [30], [50], [81] has seen increased attention due to research interests like thermophotovoltaics, super-planckian radiation[57], circularly polarized thermal emission [82], [83] and quasi-coherent thermal sources [6], [11], [80].

In this study we will look at thermal emission from disordered SiC and SiO$_2$ μ-particle films. These two material systems have optical phonons in the range of $\approx$ 8-21 μm (1250-476 cm^{-1}), making them strong candidates for thermal emission applications at or above room temperature. Moreover, they are high temperature stable with melting points of 1986 K (SiO$_2$) and 3100 K (SiC) [84]. Figure 4.1 shows a schematic of the two experiments that are performed and the information that can be obtained from each measurement.

The permittivty of polar diatomic crystals can be modelled using a Lorentz model shown in equation (4.1).
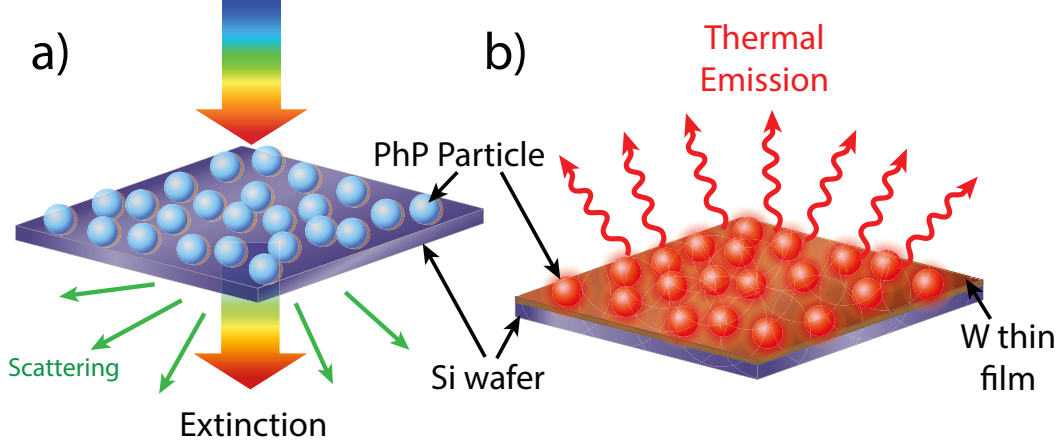
Figure 4.1: Schematic of experimental set up to measure a) extinction through transmission measurements and b) emissivity/absorbtivity through thermal emission measurements.

$$\varepsilon(\omega) = \varepsilon' + i\varepsilon'' = \varepsilon_\infty \left(1 + \frac{\omega_{LO}^2 - \omega_{TO}^2}{\omega_{TO}^2 - \omega^2 - i\omega\gamma} \right) \qquad (4.1)$$

Where ε' (ε'') is the real (imaginary) part of the dielectric permittivity, ω_{LO} (ω_{TO}) is the longitudinal (transverse) optical phonon, ε_∞ is the high frequency limit permittivity and γ is the damping coefficient. For SiC, we use the parameters $\omega_{LO} = 970$ cm^{-1}, $\omega_{TO} = 797$ cm^{-1}, $\varepsilon_\infty = 6.76$ and $\gamma = 35$ cm^{-1}. These parameters were calculated by fitting equation 4.1 to IR reflection data of a semi-insulating 6H-SiC (α-phase) wafer. However, the γ value has been increased (original $\gamma = 2.46$ cm^{-1}) due to increased damping of optical phonons in μ-particles [85]. The permittivity of SiO$_2$ was taken from references [86], [87].

The complex dielectric permittivity for both SiC and SiO$_2$ are plotted in figure 4.2. Also highlighted in this figure are the main Reststrahlen bands for both material systems. To determine the LO and TO phonon frequencies in SiO$_2$ responsible for the two main Restrahlen bands shown in figure 4.2, the SiO$_2$ data was fit using equation (4.1) with two Lorentz oscillators. This gives phonon frequencies of $\omega_{LO} = 1220$ cm^{-1} (529 cm^{-1}) and $\omega_{TO} = 1074$ cm^{-1} (466 cm^{-1}) with damping coefficients of $\gamma = 43$ cm^{-1} (19 cm^{-1}) for the high (low) frequency Reststrahlen bands and a high frequency limit permittivity of $\varepsilon_\infty = 2.10$.
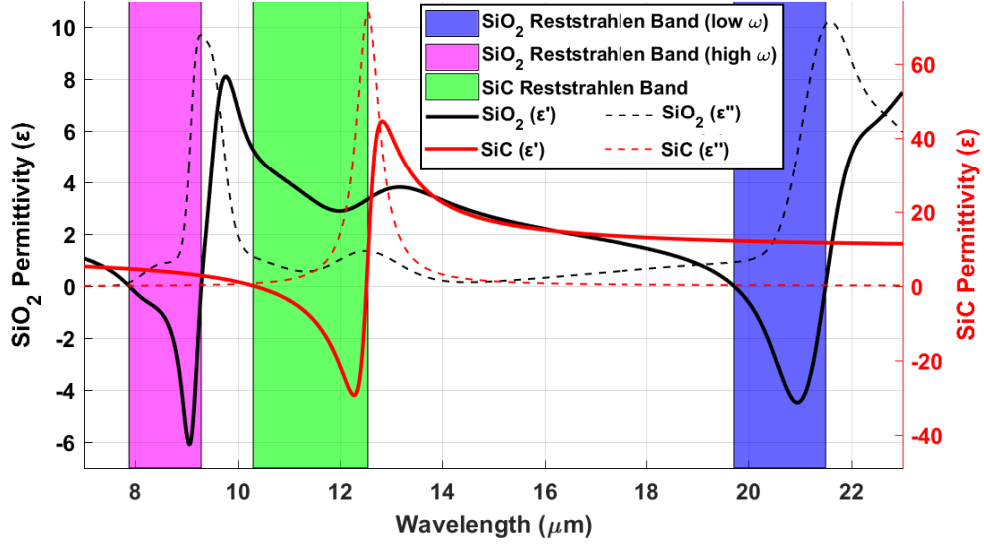
Figure 4.2: Real (solid) and imaginary (dashed) parts of the dielectric permittivity for SiO_2 (black) and SiC (red). The Restrahlen bands for both materials are also highlighted. SiC (green area) exists between 10.3-12.5 μm. SiO_2 has two bands that exist between 7.9-9.3 μm (purple area) and 19.7-21.5 μm (blue area).

4.2   Resonances in Polaritonic Particles

The absorption and scattering of electromagnetic radiation from particles is well described by Mie theory [20]. A useful measure for determining how the size of a spherical particle influences the Mie absorption or scattering efficiency is the size parameter $x = k_0 r$, where k_0 is the free space wave-vector and r is the particle radius. For small size parameter particles ($k_0 r \to 0$), we approach the quasi-static limit where a uniform electric field occupies the entire volume of the particle and therefore can be approximated as a dipole. In this regime there is a single resonance known as the Fröhlich mode [68], [88], [89] that can be calculated using equation (4.2).

$$\omega_F = \sqrt{\frac{\omega_{LO}^2 + \omega_{TO}^2 \frac{2\varepsilon_m}{\varepsilon_\infty}}{1 + \frac{2\varepsilon_m}{\varepsilon_\infty}}} \tag{4.2}$$

ω_F is the resonant frequency of the Fröhlich mode and ε_m is the permittivity of the surrounding matrix (we will consider $\varepsilon_m = 1$).

Table 4.1 shows the Fröhlich resonance frequencies for SiO_2 and SiC par-

51

Table 4.1: Polaritonic particles Fröhlich mode resonant frequencies

Material	Restrahlen Band [high/low (ω)]	ω_{LO} [cm^{-1}]	ω_{TO} [cm^{-1}]	ε_∞	ω_F [cm^{-1}]	λ_F [μm]
SiO$_2$	high	1220	1174	2.10	1154	8.68
SiO$_2$	low	529	466	2.10	499	20.02
SiC	-	970	797	6.76	933	10.71

ticles within the quasi-static limit as well as the optical phonon frequencies (ω_{LO} and ω_{TO}) and high frequency permittivity (ε_∞) used to calculate them. For SiC, we used the optical phonon frequencies presented earlier. For SiO$_2$, we use the optical phonon frequencies from the fitting procedure described earlier. At these Fröhlich mode frequencies, polaritonic particles are known to have large absorption cross sections [77], [89].

For larger sized particles that are outside of the quasi-static limit, there are additional higher order modes present. These modes are expected to be in the same frequency range as the Fröhlich mode giving a broader spectral response than the single Lorentzian oscillator shape of the Fröhlich mode. Mie theory can be used to calculate scattering and absorption efficiencies [20], [90] for these larger particles, accounting for these higher order terms. The efficiency (Q_i) represents a particles ability to interact with EM radiation and is defined as the scattering cross section normalized by the particles spatial cross section (πr^2 for a sphere) as shown in equation (4.3).

$$Q_i = \frac{\sigma_i}{\pi r^2} \tag{4.3}$$

Where i represents extinction (ext), scattering (sca) or absorption (abs). σ_i is the scattering cross section and r is the radius of the particle. The calculations for Q_{ext} and Q_{abs} are described in the supplementary information/appendix C.

Figure 4.3 shows the a) absorption (Q_{abs}) and b) extinction (Q_{ext}) efficencies for 1 and 4 μm SiO$_2$ spheres ($r = 0.5$ μm and $r = 2$ μm respectively) as well as 2 μm SiC spheres ($r = 1$ μm). For these simulations, we used the permittivities shown in figure 4.2. Within the absorption spectra of the three particles, we can see the main dipolar Fröhlich mode at ≈ 8.6 μm (20.0 μm)

for the SiO_2 high (low) frequency Restsrahlen band and ≈ 10.7 μm for SiC.
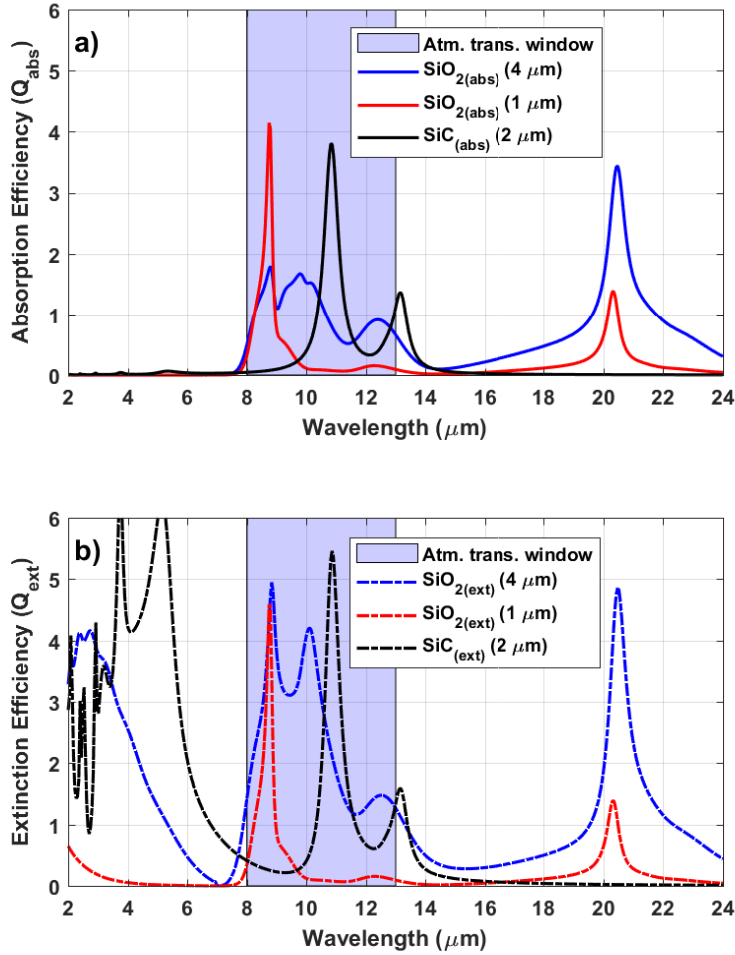
Figure 4.3: a) Absorption (solid lines) and b) extinction (dashed lines) efficiencies of 4 μm (blue lines) and 1 μm (red lines) SiO_2 spheres ($r = 2$ μm and $r = 0.5$ μm) and 2 μm SiC spheres (black lines) ($r = 1$ μm).

4.3 Infrared Transmission Spectroscopy

To investigate the extinction spectra of our particle films with transmission measurements, we must deposit them on an IR transmissive substrate. We use a Si wafer which has $\approx$5-40 % transmission from 4-25 μm. While transmission is relatively low at shorter IR wavelengths, it is sufficient to allow enough source signal through for our measurements. SiO_2 particle dispersions are made by
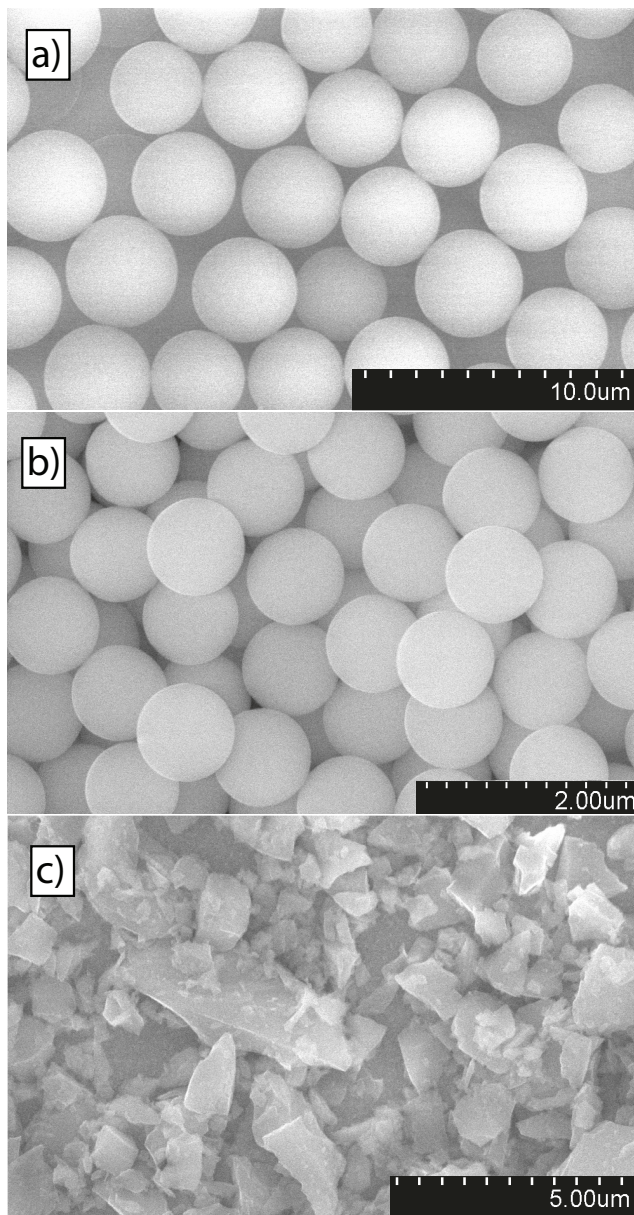
Figure 4.4: SEM images of a) 4 μm SiO$_2$ spheres, b) 1 μm SiO$_2$ spheres and c) 2 μm SiC particles.

mixing 1 mL of 5% aqueous SiO$_2$ μ-spheres (Sigma-Aldrich) with 4 mL of isopropyl alcohol to dilute the particle dispersion. SiC particle dispersions are made by adding 2 μm α-particle powder (Alfa Aesar) to ethanol in a 10 mg/mL concentration. Several drops of the particle dispersions are place on Si substrates and allowed to dry. SEM images of the disordered particle systems are shown in figure 4.4.

Transmission measurements are performed with a Thermo Fisher Scientific Nicolet is50 FTIR spectrometer using the Polaris^{TM} long lifetime IR-source and a deuterated triglycine sulfate (DTGS) detector. Figure 4.5 shows the extinction (-$\log_{10}(T)$) spectra for the SiO_2 and SiC disordered particle films. Qualitatively, these spectra match very well with the extinction efficiency spectra in figure 4.3. Of note in the SiO_2 spectra are the two Fröhlich resonances at $\approx$ 8 μm and $\approx$ 21 μm. Additionally, we can see a strong SiC extinction peak at $\approx$ 11-12 μm. This main peak appears to be broader and slightly red shifted when compared to the predicted peak in figure 4.3. This difference can be attributed several causes including particle size and shape variation since the particles are not spherical and a large distribution of particle size can be seen be figure 4.4. Additionally, long range coupling of SiC particles in 3D arrays is predicted by Tervo et al. [91], leading to a similar spectral peak shape to the one observed here. While Tervo et al. only consider an ordered 3D array, we believe that long range coupling of these SiC particles persists to some degree for our disordered systems. This has also been observed in other experimental transmission measurements on SiC α-particles [77], [85]. Lastly, we can see the broadband scattering regions begin at $\approx$ 4, 7 and 10 μm for the 1 μm SiO_2, 4 μm SiO_2 and 2 μm SiC particles respectively. Again, this agrees with the broadband scattering regions predicted in figure 4.3.

4.4 Thermal Emission Spectroscopy

Thermal emission measurements are taken using a custom built high temperature vacuum chamber coupled to the FTIR spectrometer. The experimental set up is described in reference [80]. Emissivity spectra are calculated using equation 4.4.

$$\epsilon(\lambda) = \frac{S_S(\lambda, T_S) - S_R(\lambda, T_R)}{L(\lambda, T_S) R_{det}(\lambda) A_{spot} \Omega} \tag{4.4}$$

where $\epsilon(\lambda)$ is the emissivity spectrum, $S_S(\lambda, T_S)$ is the measured sample signal at sample temperature T_S, $S_R(\lambda, T_R)$ is the measured background signal signal at room temperature T_R, $L(\lambda, T_S)$ is the Planck distribution for a black-
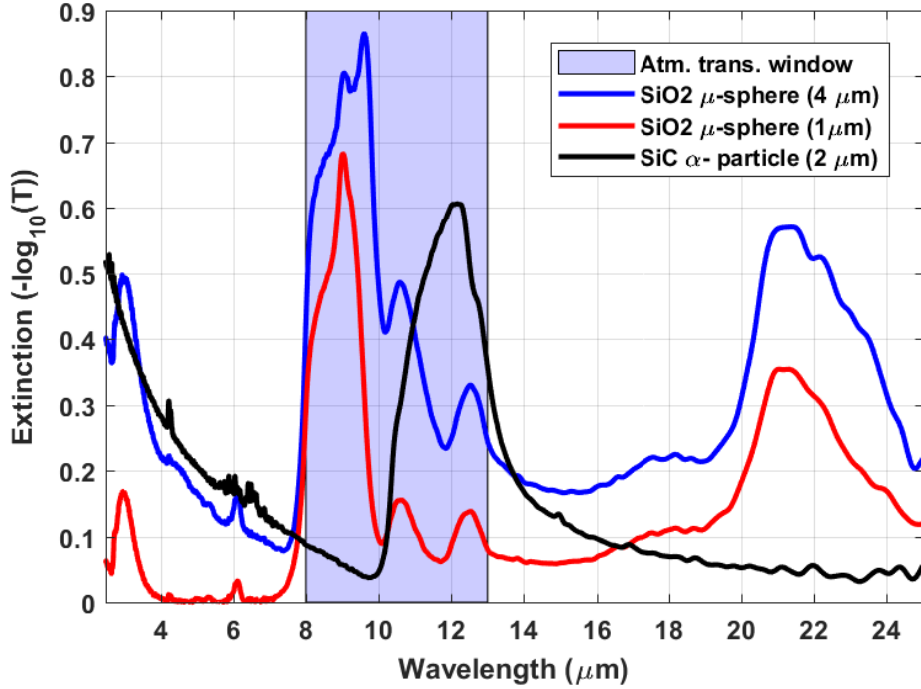
Figure 4.5: Extinction spectra for 4 μm (blue) and 1 μm (red) SiO$_2$ spheres ($r = 2$ μm and $r = 0.5$ μm) and 2 μm SiC particles (black) ($r \approx 1$ μm).

body at temperature T_S, A_{spot} is the spot size area on the sample, Ω is the solid angle of collection and $R_{det}(\lambda)$ is the responsivity of our detector. For thermal emission measurements, we use a mercury cadmium telluride (MCT) detector and the responsivity of it is calibrated using a black-body cavity source (Infrared Systems Development Corp. IR-518). An MCT detector has higher sensitivity in in the 2-16 μm spectral region and is used for this reason. Furthermore, a ZnSe window is used to outcouple thermal signal from our vacuum chamber (see ref. [80]) which cuts off radiation at ≈ 20 μm, limiting our long wavelength detection capability.

The polaritonic particles must be placed on a low-E (emissivity) substrate that is capable of reflecting thermal infrared radiation generated by the heater. A low-E substrate reduces background emission allowing the signal from polaritonic particles to be easily resolved. We sputter a 300 nm thin film of tungsten on a silicon substrate with a 10 nm titanium film to improve adhesion. Tungsten is a refractory metal that has high IR reflectivity ($> 90\%$) [92],

[93].

Figure 4.6 shows the emissivity spectra of our polaritonic particle samples on tungsten thin films at 823 K. For reference, the emissivity spectrum of a bare tungsten thin film is included as a baseline. Contrary to the extinction spectra of SiO_2 particles shown in figure 4.5, we see that the 1 μm spheres have a stronger peak. This demonstrates that while 1 μm SiO_2 particles have stronger absorption/emission efficiencies, 4 μm SiO_2 particles have stronger scattering efficencies. This is described by Mie theory and predicted in figure 4.3. The main resonance peak (Fröhlich mode) is still observed around 9 μm. However, it is slightly red shifted, which is to be expected as optical phonon frequencies red shift as a polaritonic material's temperature is elevated [67], [80]. An addition peak at 12.3 μm is clearly visible and is the result of another oscillator resonance that is also observed as an extinction peak in figure 4.5 and a peak in ε''_{SiO_2} in figure 4.2.
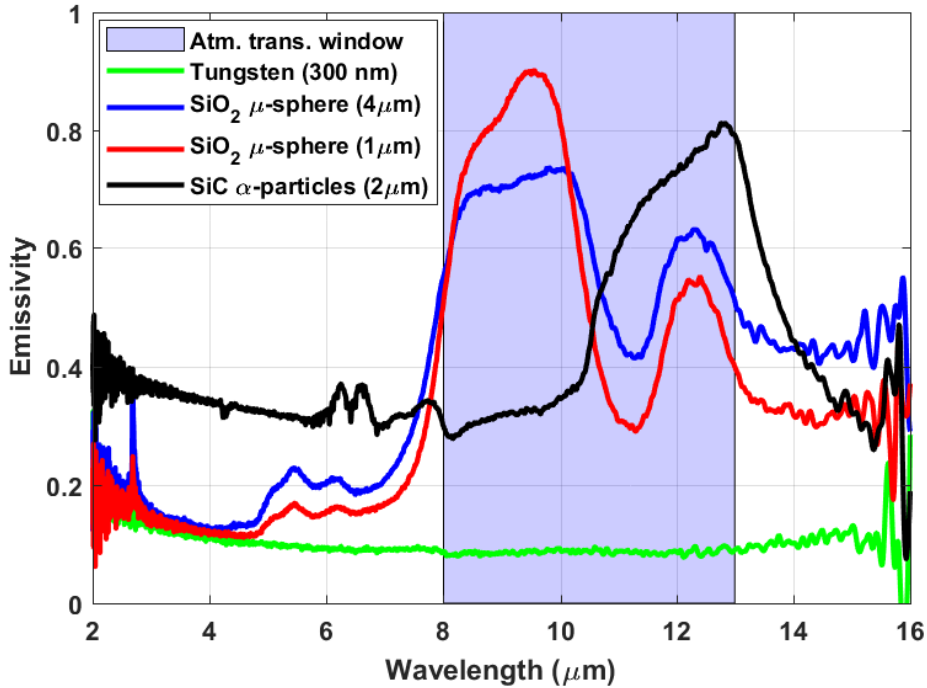
Figure 4.6: Emissivity spectra for 4 μm (blue) and 1 μm (red) SiO_2 spheres ($r = 2$ μm and $r = 0.5$ μm) and 2 μm SiC particles (black) ($r \approx 1$ μm) at 823 K. The emissivity spectrum of a tungsten thin film (green) is included as a baseline reference for all samples.

The emissivity spectrum of SiC particles is again qualitatively similar to the extinction spectrum shown in figure 4.5. The main resonance peak (Fröhlich mode) is centered around ≈ 12 μm (however, slightly red shifted). The shape of the emission resonance mirrors that in figure 4.5 and those described in ref's [77], [85], [91]. The obvious and striking difference between the emissivity and extinction spectra is that the baseline emissivity appears to be significantly higher than that of the SiO_2 samples or the bare tungsten thin film. Several reasons can be cited to explain this increased baseline emissivity for SiC. First, we know that for polar dielectric particles, the damping coefficient is larger than that of its bulk crystalline counterpart. Additionally, we know that increasing the temperature of a polar dielectric material can also increase the damping coefficient of that material. Lastly, the SiC μ-particle powder is quoted as being 99.8% pure, suggesting 0.2% of the powder is free Si and C. These impurities can act as a soot leading to broad black emission. We attribute the increased baseline emissivity of SiC particles to the combination of these effects. This broad emission/absorption can also be seen in figure 4.3. The absorption efficiency of SiC particles show broad nonzero absorption ($Q_{abs} \approx 0.05$) from 2-9 μm, whereas for SiO_2 it is near zero ($Q_{abs} \approx 10^{-4}$). To reduce this broad background emissivity one can use either smaller particles (≈ 1 μm) or address the inflated damping coefficient.

4.5 Radiative Cooling Power

Due to the strong overlap between the polaritonic emission bands and the atmospheric transmission window, such a device is well suited for passive radiative cooling applications. To estimate the cooling power of a device fabricated from these polaritonic particles, we have performed a cooling power calculation, the details of which can be found in appendix B. Figure 4.7 shows the results of the calculation.

In panel a) we see the emissivity spectrum of the energy radiated out by the emitter in red. The blue area represent the energy that is being absorbed from the atmosphere and the black area represents the power being absorbed
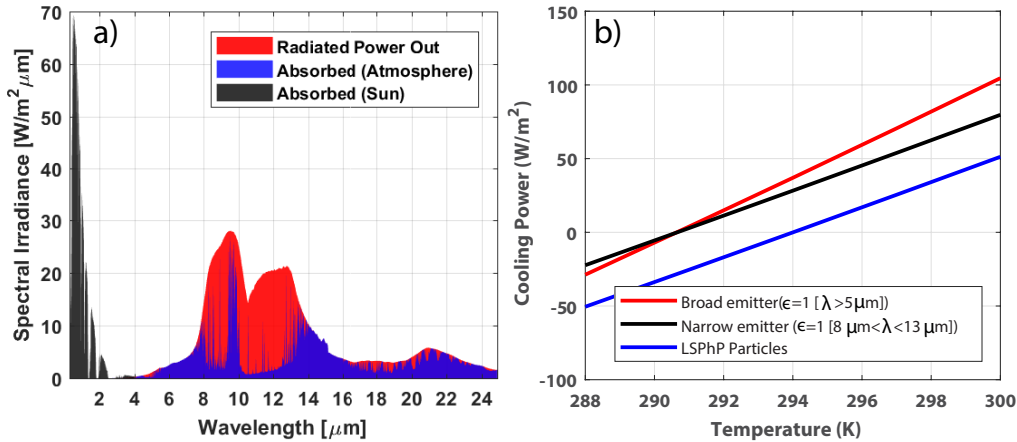
Figure 4.7: a) Emitted radiation spectrum of emitter (red) and absorbed spectra from the sun (black) and the atmosphere (blue). b) The radiative cooling power of the LSPhP particle device as a function of temperature (blue) compared to an ideal broad (red) and ideal narrow (black) emitter.

by the sun (we take 5% of the total AM1.5 solar spectrum). Additional assumptions for this calculation are that $h_c = 6\,W/m^2 K$ and that the ambient air temperature is $27°C$ ($300K$). We can see that for our emitter, the equilibrium temperature would be approximately $6°C$ cooler than ambient. In addition, when the emitter is at the same temperature as the ambient air, we see a cooling power of $\approx 50\,W/m^2$). This level of cooling is similar to what has been observed in other works [9], [10]. However, this design has the additional benefit of low cost, easy manufacturing.

4.6   Conclusion

In summary, we have measured the emissivity spectrum of SiO_2 and SiC polaritonic particles through direct thermal emission measurements and shown that they qualitatively agree with measured extinction spectra and simulations from Mie theory. We have demonstrated that that these particle resonances can be be used to generate strong thermal emission bands near the black-body limit ($\epsilon = 0.9$ for 1 μm SiO_2 μ-spheres and $\epsilon = 0.8$ for 2 μm SiC particles) and could lead to the development of commercial products in the fields of passive radiative cooling or thermal IR sources. These particular samples are

not optimized for any one application. Particle size, shape, crystal structure and material can be considered when trying to control the spectral shape, bandwidth or location of engineered thermal emission bands. This thermal measurement technique can also be applied to other systems to indirectly measure the IR absorption properties of scattering elements or subwavelength particles, deconvolving it from the scattering spectra without the use of an integrating sphere.

Chapter 5

High Temperature Polaritons in Ceramic Nanotube Antennas

High temperature thermal photonics presents unique challenges for engineers as the database of polaritonic materials that can withstand the extreme environments necessary are very limited. Hexagonal boron nitride (hBN) is an emerging high temperature stable 2D material that possesses low-loss polaritons in two spectrally distinct frequency bands. The hyperbolic nature of these frequency bands leads to a large local density of states (LDOS). In 2D form, these polaritonic states are dark modes, bound to the material. In cylindrical form, boron nitride nanotubes (BNNTs) create subwavelength particles capable of coupling these dark modes to radiative ones. In this study, we leverage the high frequency optical phonons present in BNNTs to create strong mid IR thermal antenna emitters. Through direct measurement of thermal emission of a disordered system of BNNTs we confirm their radiative polaritonic modes and show that the antenna behavior can be observed even in a disordered system. To our knowledge, these are the highest frequency optical phonon polaritons that exist and could be used as high temperature mid-IR thermal nano-antenna sources.

5.1   Introduction

The field of thermal photonics aims to control the radiation emitted by objects due to thermal fluctuations within the medium. The field has experienced re-

newed interest due to the promise of emerging technologies such as thermopho-tovoltaics [3], [19], [22] and passive radiative cooling [9], [10]. By careful consid-eration of an objects material composition as well as its micro/nanostructure, studies have shown it is possible to control spectrum, polarization, coherence and directionality of thermal radiation. The subset of high temperature ther-mal photonics presents a unique set of challenges as materials need to be stable in these extreme environments and, in some cases, access higher energy po-laritonic resonances commensurate with energy densities of a black body at higher temperatures.

Since Rubio et al's prediction in 1994 [94], the potential of boron nitride nanotubes (BNNTs) and its 2D counterpart, hexagonal boron nitride (hBN), has spread to many scientific communities because of their unique set of prop-erties such as high thermal conductivity, thermal stability, mechanical strength and neutron absorption [95]–[97]. This combination of properties makes BN-NTs appealing for many applications in the aerospace industry, among others, where materials need to routinely sustain extreme environmental conditions. The last decade has also seen the materials make waves in the fields of nanopho-tonics and quantum optics due to their ability to support phonon polaritons [98], [99] and behave as single photon emitters [100], [101].

Plasmonic metamaterials [3], [50], [79], [81] have been proposed as systems for controlling radiative thermal emission but the high-loss and low melting point of metals has stunted their progress. Polar dielectric materials support-ing phonon polaritons have also been investigated with great success [5], [6], [12], [68], [80] but these materials are limited to low frequency mid-IR optical phonons < 1200 cm^{-1} (> 8.6 μm). Interestingly, hBN is a natural hyperbolic material that has shown thermal stability at temperatures up to 1173 K [95]. The combination of thermal stability, low-loss and hyperbolic permittivity of hBN and BNNTs make them excellent candidates for high temperature in-frared photonics. In this study, we look at the radiative thermal emission spectrum of a disordered system of BNNT nanoantennas.

hBN is a 2D material that has the same hexagonal crystal structure as graphene but with alternating boron and nitrogen atoms in place of carbon.

These 2D layers can be stacked on top of each other to form bulk hBN. Optically, this polymorph forms an extremely anisotropic material, with the perpendicular ($\varepsilon_\perp$) and parallel ($\varepsilon_\parallel$) components of permittivity well modelled as Lorentz oscillators:

$$\varepsilon(\omega) = \varepsilon' + i\varepsilon'' = \varepsilon_\infty \left(1 + \frac{\omega_{LO}^2 - \omega_{TO}^2}{\omega_{TO}^2 - \omega^2 - i\omega\gamma} \right). \tag{5.1}$$

We know that the resonant frequency of a Lorentz oscillator is inversely proportional to the square root of the mass of the oscillator ($\omega_{TO} \propto 1/\sqrt{m}$). Because boron and nitrogen are among the lightest elements capable of forming polar crystals, hBN and BNNTs produce the highest known optical phonon frequencies. Table 5.1 shows the optical phonon frequencies used to model the perpendicular ($\varepsilon_\perp$) and parallel ($\varepsilon_\parallel$) components of permittivity for hBN as well as other commonly used materials with optical phonons. All other listed materials possess lower frequency optical phonons than the in plane phonons of hBN ($\varepsilon_\parallel$). Interestingly, because both components of permittivity have a spectrally distinct Reststrahlen band, hBN posseses both types of optical hyperbolicity. Type I, which has one negative component and two positive components ($\varepsilon_\perp' < 0$ & $\varepsilon_\parallel' > 0$), exists between 760 and 825 cm^{-1} and Type II, which has two negative components and one positive component ($\varepsilon_\perp' > 0$ & $\varepsilon_\parallel' < 0$), exists between 1360 and 1614 cm^{-1} [44]. Figure 5.1 a) shows the permittivity of both components highlighting the two Reststrahlen bands (regions of hyperbolicity).

The hyperbolic topology of the isofrequency surface of hBN leads to a large local density of states (LDOS) in hBN as a 2D material. This is due to the unbounded nature of a hyperboloid, which is in contrast to isotropic materials that posses bounded isofrequency contours of spherical or ellipsoidal topology. One can calculate the LDOS in the near-field above a surface of hBN [57], [109], [110]. Figure 5.1 b) shows the LDOS at several near-field distances above a hBN-vacuum interface. Both Reststrahlen bands show large LDOS in the extreme near-field but decay as we move away from the interface. This implies that for hBN, these are dark modes that are not present in the far-

Table 5.1: Optical phonon frequencies of common phonon polaritonic materials show that the in plane optical phonons of hBN have the highest frequencies.

Material Permittivity	ω_{LO} (λ_{LO}) [cm^{-1}] (μm)	ω_{TO} (λ_{TO}) [cm^{-1}] (μm)	γ [cm^{-1}]	ε_∞	Ref.
hBN ($\varepsilon_\parallel/\varepsilon_{t,a}$)	1614 (6.20)	1360 (7.35)	7	4.90	[98]
hBN ($\varepsilon_\perp/\varepsilon_r$)	825 (12.12)	760 (13.16)	2	6.76	[98]
cBN	1340 (7.46)	1065 (9.39)	40.5	4.5	[102]
SiO$_2$	1186 (8.43)	1167 (8.57)	4.43	2.09	[103]
	1112 (9.00)	1046 (9.56)	15.53		
	1106 (9.04)	1058 (9.45)	0.42		
	814 (12.29)	799 (12.52)	12.94		
	525 (19.05)	434 (23.04)	54.14		
SiC	969 (10.32)	793 (12.61)	4.76	6.70	[51]
SrTiO$_3$	788 (12.69)	543 (18.42)	17.0	5.10	[104]–[106]
	474 (21.10)	175 (57.14)	5.4		
	172 (58.14)	91 (109.89)	15.0		
α-GaN	740 (13.51)	530 (18.87)	7	5.40	[107]
β-GaN	739 (13.53)	553 (18.08)	7	5.35	[107]
GaP	403 (24.8)	367 (27.25)	1.29	9.09	[108]

field and would not produce strong thermal radiation. However, by creating sub-wavelength particles (BNNTs) out of phonon polaritonic materials (hBN) we can introduce a mechanism to couple the dark modes to radiation in the far-field.

By rolling a sheet of hBN in to a tubular geometry we can form BNNTs (figure 5.2), which are analogous to their carbon counterpart carbon nanotubes (CNTs). In doing so, we form an extremely anisotropic nanotube who's axial (and tangential) permittivity is equivalent to the parallel component of hBN ($\varepsilon_\parallel \rightarrow \varepsilon_{t,a}$) and who's radial permittivity is equivalent to the perpendicular component of hBN ($\varepsilon_\perp \rightarrow \varepsilon_r$). The orientation of permittivities for hBN and BNNTs is shown in figure 5.2 which depicts the atomic crystal structure of the two.

5.2 Optical Phonons in BNNTs

Mie theory is used to calculate the absorption resonances present in BNNTs. Figure 5.3 a) shows the absorption efficiency of an infinitely long isotropic
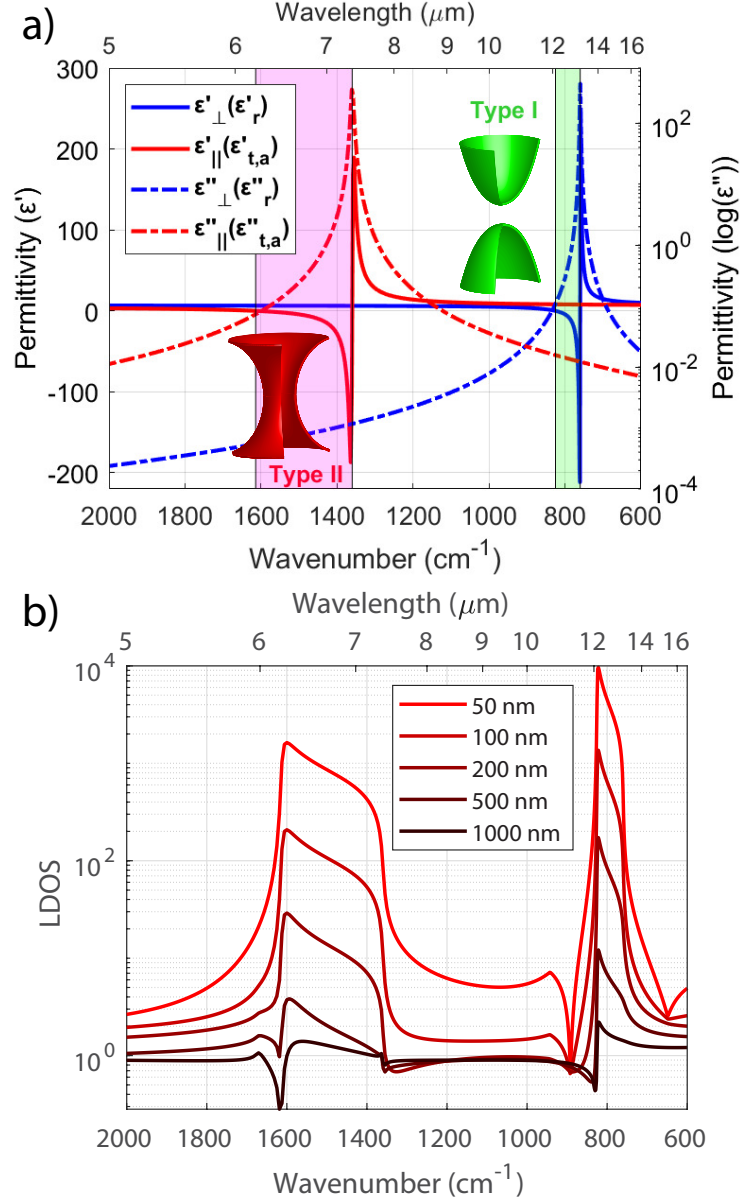
Figure 5.1: a) Real (solid) and imaginary (dashed) parts of the dielectric permittivity for hexagonal boron nitride in the perpendicular (blue) and parralel (red) directions. For the cylindrical geometry of a nanotube, the perpendicular component becomes radial ($\varepsilon_\perp = \varepsilon_r$) and the parrallel component becomes the axial ($\varepsilon_\parallel = \varepsilon_a$) and tangential ($\varepsilon_\parallel = \varepsilon_t$) component of permittivity for a BNNT. The two Reststrahlen bands are highlighted in magenta (upper band) and green (lower band). b) LDOS above a hBN-vacuum interface at various distances from 50 nm (top) to 1000 nm (bottom).

cylinder for the two permittivities of hBN [111], [112]. There are three resonant polaritonic modes that lead to strong absorption. First, at 1573 cm^{-1}, is
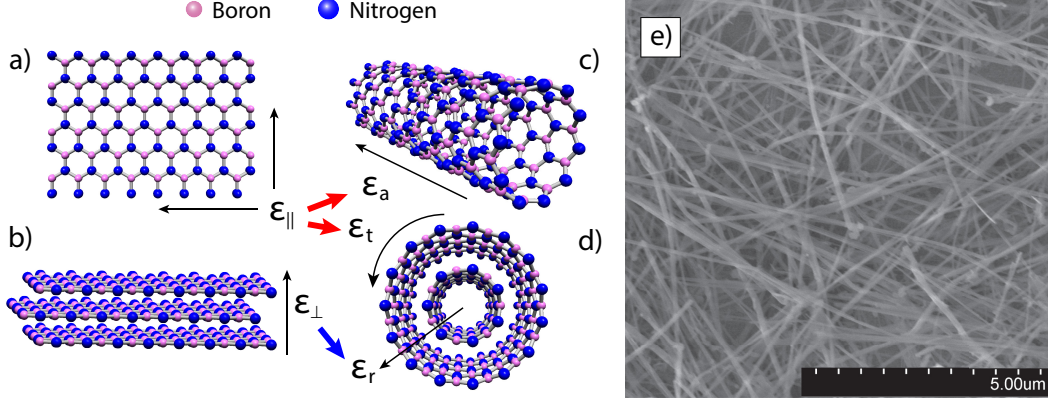
Figure 5.2: Schematic of the atomic structure of hBN from a) plane view showing $\varepsilon_\parallel$ and b) side view of bulk hBN showing $\varepsilon_\perp$. c) side view of BNNT showing ε_a and d) end view of BNNT showing ε_r and ε_t. e) SEM image of disordered BNNT system that transmission and emission measurements are taken from.

the tangential (T) mode that results from B-N stretching in the tangential direction (ε_t) [113], [114]. The second, at 1356 cm^{-1}, is the longitudinal (L) mode and results from B-N stretching in the axial direction (ε_a) [113], [114]. Third is the radial buckling (RB) mode, at 817 cm^{-1}, which is the result of B-N oscillations between tubes of multi-walled BNNTs (sheets of hBN) in the radial direction (ε_r) [113].

IR transmission measurements are performed to confirm the presence of the predicted absorption resonances. To do this, multi-walled BNNTs of average diameter 50 nm and lengths of 5-20 μm are dispersed on to a polished Si wafer that is partially transmissive from 4-25 μm. The transmission measurement is plotted as the extinction spectrum (-$\log_{10}(T)$) and is shown in figure 5.3 b).

Figure 5.3 b) clearly shows the three absorption resonances predicted by Mie theory in figure 5.3 a). The L mode occurs at 1367 cm^{-1} which we consider to be a negligible shift from 1356 cm^{-1}. The T mode is now located at 1540 cm^{-1}, a 33 cm^{-1} shift from predicted. This is likely due to a shift in the optical phonon frequencies caused by the curvature of the nanotube geometry, which is supported by other studies that observe a shift in the frequency of this mode for varying nanotube radii [114]. This would also suggest that for disordered systems of BNNTs with varying radii, a slight broadening of this

66
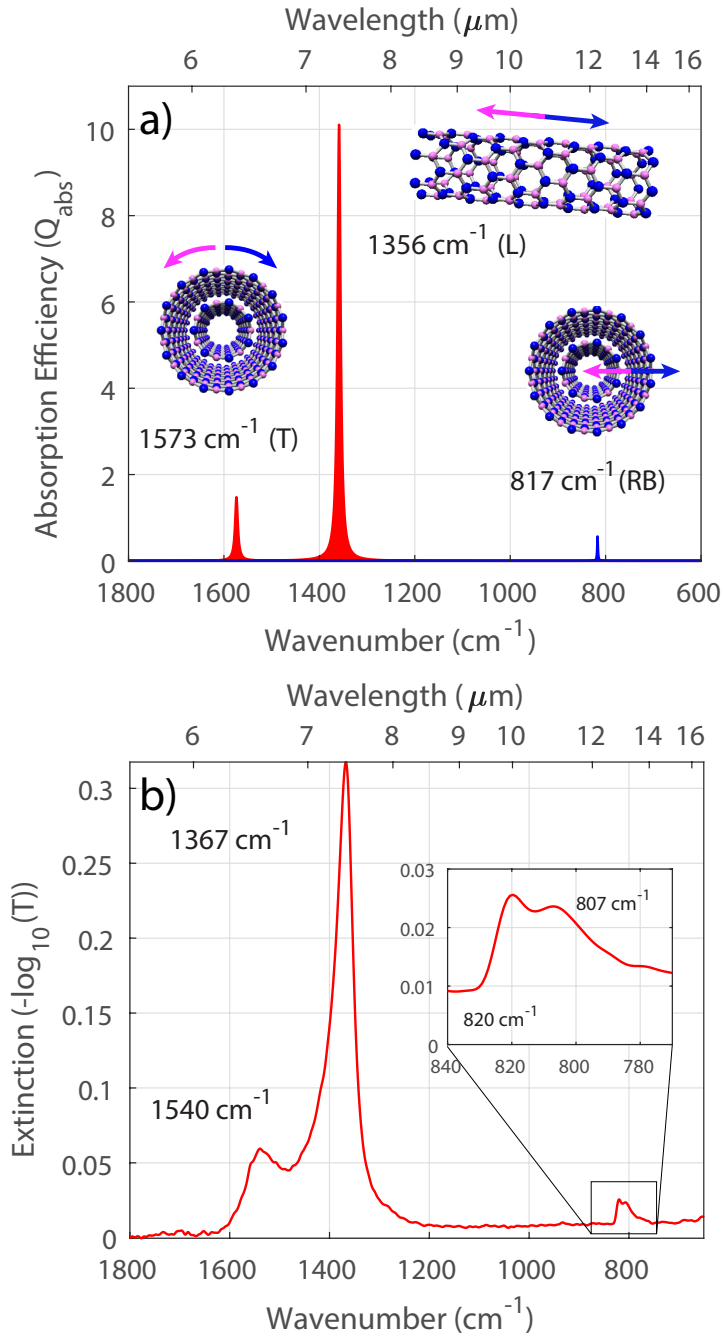
Figure 5.3: a) Absorption efficiency for an infinitely long cylindrical hBN nanotube. The T and L modes correspond to the upper frequency oscillator ($\varepsilon_{t,a}$) and are shown in red, while the RB mode corresponds to the lower frequency oscillator (ε_r) is shown in blue. Schematics of each mode are shown and illustrate the boron (pink) and nitrogen (blue) ion movement for a given incident field. b) Extinction spectrum for the disordered system of BNNTs.

mode should be observed, as is seen here. A sharper T mode emission peak should be possible with precise control over nanotube radii. Interestingly, the weak RB mode appears to have split in to two peaks located at 807 and 820 cm^{-1}. While this "splitting" has been observed before in other BNNT studies [114], the origin is not well understood. Further calculations from first principles are needed to identify the cause but speculatively it could be the result of complex interaction between multiple layers of a multi-walled BNNT with different chiralities [114].

5.3   Thermal Emission Spectroscopy

Kirchoff's law states that the linear spectral and angular emissivity ($\epsilon(\omega, \theta)$) is equal to the spectral and angular absorptivity ($\alpha(\omega, \theta)$) [1]. This suggests that the same absorption bands seen in transmission measurements should also be present in thermal emission measurements. By thermally exciting the BNNTs, we can investigate the optical phonon modes via IR spectroscopy as they are IR active and will radiate at elevated temperatures.

Thermal emission measurements are performed with a custom high temperature vacuum chamber IR spectroscopy set up shown in figure 5.4 and described in more detail in reference [[80]]. To isolate thermal emission from the BNNTs one must suppress background thermal radiation generated by the substrate heater. To achieve this the disordered BNNT system is deposited on a refractory high IR reflectivity thin film (300 nm of tungsten). Figure 5.5 shows the emissivity spectrum of the disordered BNNT system on a 300 nm tungsten thin film at 938 K.

The emissivity spectrum is calculated as:

$$\epsilon(\omega, \theta, T_S) = \frac{S_S(\omega, \theta, T_S) - S_R(\omega, T_R)}{L(\omega, T_S)R_{det}(\omega)A_{spot}\Omega} , \qquad (5.2)$$

where $S_S(\omega, \theta, T_S)$ is the spectral angular radiance of the sample at temperature T_S and angle θ, $S_R(\omega, T_R)$ is the background spectral radiance of the room and optical elements in the beam path at room temperature, $L(\omega, T_S)$ is the spectral radiance of a black-body at temperature T_S, $R_{det}(\omega)$ is the cal-
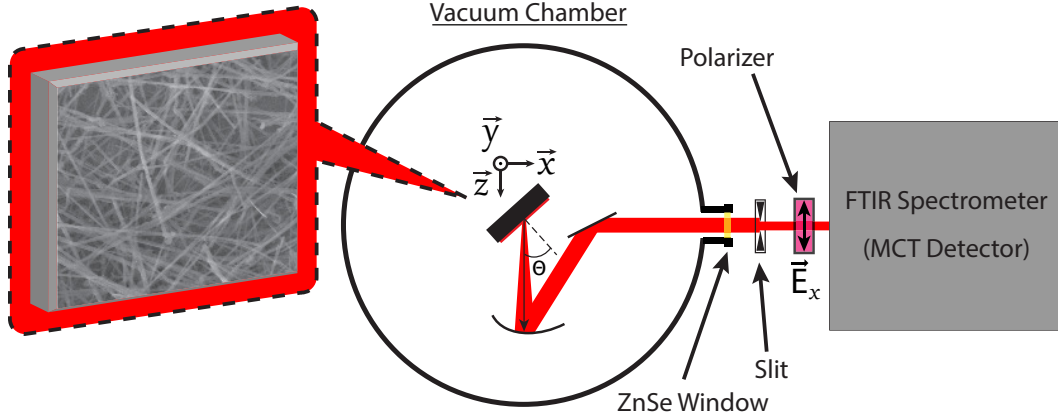
Figure 5.4: Schematic of experimental set-up of thermal emission vacuum chamber spectrometer.
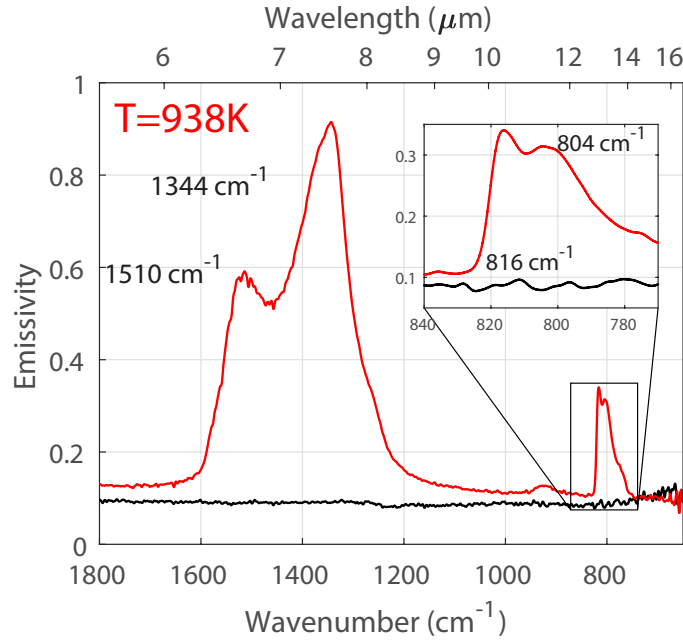
Figure 5.5: Spectral emissivity of BNNT system on tungsten thin film (solid red) at 938 K. The emissivity spectrum of a tungsten thin film is shown (solid black) for reference.

ibrated responsivity function of the detector, A_{spot} is the collection spot size on the sample and Ω is the solid angle of collection.

In the emissivity spectrum we see the three spectrally distinct absorption bands seen in the Mie absorption efficiency spectrum (figure 5.3 a)) as well as the extinction spectrum (figure 5.3 b)). The T and L modes now exist at 1510

69

and 1344 cm^{-1} respectively. The "splitting" of the RB mode is still observed in emission measurement and are now located at 803 and 814 cm^{-1}. This red shifting of optical phonon modes is discussed in the following section.

5.3.1 Temperature Dependence of Spectral Emissivity

To characterize the red shift of the absorption bands at elevated temperatures, we measure emissivity from 560 to 938 K. Over this temperature range we observe a frequency shift of ≈ 18 cm^{-1} for the T mode and ≈ 13 cm^{-1} for the L mode. This is the result of red shifting of optical phonon frequencies of hBN at elevated temperatures [80] likely caused by thermal expansion. We note that the shift in the RB mode appears to be less pronounced, now occurring at 803 and 814 cm^{-1}. However, if you analyze the peak shifting in terms of wavelength, all modes shift by ≈ 50 nm over the full temperature range (560 - 938 K). Also of note is that for more moderate temperatures (560 K), the L mode peak approaches the black-body limit achieving an emissivity of $\varepsilon = 0.97$. This is due increased polaritonic damping at higher temperatures.
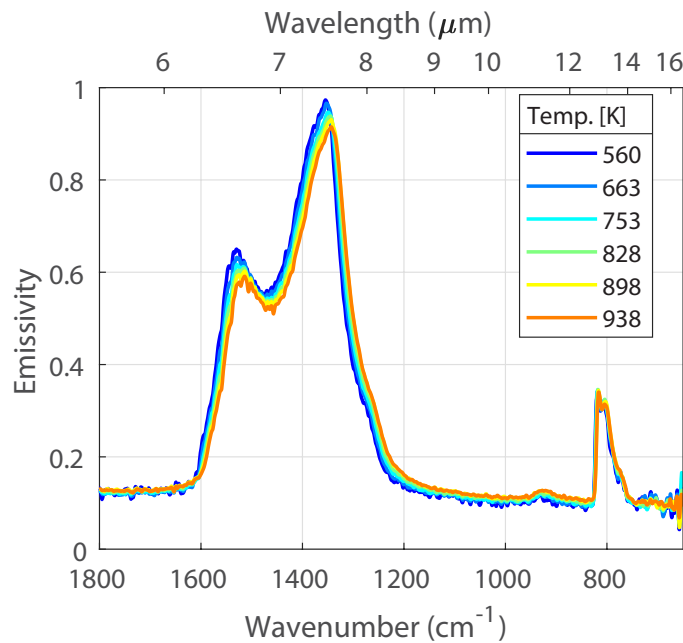
Figure 5.6: Temperature dependence of BNNT emissivity.

5.3.2 Thermal Antenna Effect in Disordered Nanotubes

In general, a disordered system of particles such as this should exhibit no angularly dependent emission behavior. However, for our system, there is one degree of quasi-order, which is that the nanotubes are predominantly lying down with their axis parallel to the substrate plane. Using this fact, we can take polarized angularly dependent thermal emission measurements to further probe and experimentally distinguish the optical phonon modes of BNNTs. Because the L mode results from ion oscillations along the nanotube length, the radiation emitted from this mode will be polarized along the nanotube axis. Figure 5.7 shows the two basis orientations that a nanotube can have and the electric field polarization for each. If we consider each nanotube as a dipole antenna, we know that the radiation pattern is strongest when the wave vector is perpendicular to the nanotube axis $(\vec{k} \perp \vec{l_c})$ and does not radiate parallel to the nanotube axis $(\vec{k} \parallel \vec{l_c})$. We can therefore attempt to remove the L mode resonance from the emissivity spectrum by collecting emission at highly oblique angles $(\theta \to 90°)$ to suppress $\vec{E_x}$ polarized emission and use a wire grid IR polarizer to remove $\vec{E_y}$ polarized emission.

Figure 5.8 shows the x-polarized emissivity spectrum as the angle is varied from $\theta = 0° - 70°$. We can see the main L mode peak is suppressed at higher angles, while the other modes (T and RB) are largely unchanged. If precise control over the orientation of the BNNT system was possible, we would be able to more effectively suppress the L mode leaving only the T and RB mode present in the emissivity spectrum. The relative presence of the L mode is an indication that for our sample, some BNNTs are not purely in the plane of the substrate and have a slight angle relative to the substrate surface.

5.4 Conclusion

In summary, we have measured the emissivity spectrum of a disordered BNNT system and show its thermal antenna behavior can be observed even in a disordered system. Three emission bands located at 1510, 1344 and 810 cm^{-1} (6.6, 7.4 and 12.3 μm) are present in the emissivity spectrum (at 938 K),
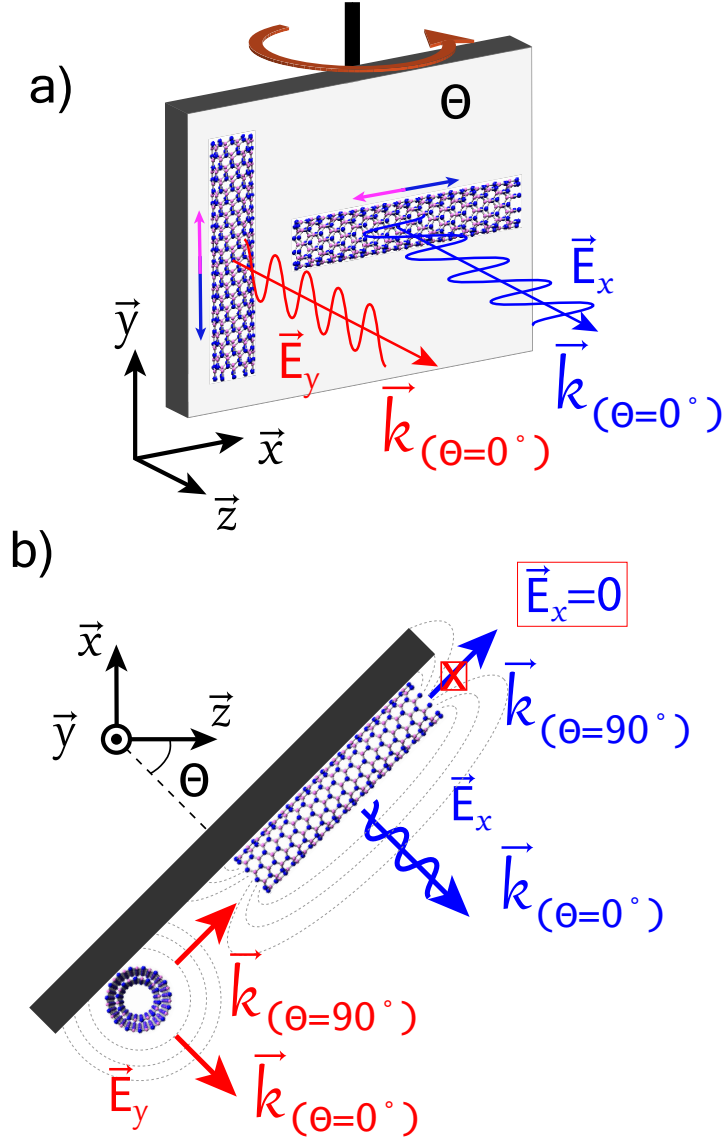
Figure 5.7: Schematic of the L mode radiation pattern and polarization orientation. Emission is measured in the z-direction.

which are result of optical phonon modes supported by BNNTs. The emissivity spectrum is compared to the measured extinction spectrum and Mie absorption efficiency and show strong agreement. At normal incidence, the emissivity of the L mode approaches the black body limit ($\epsilon = 0.97$ at 560K).

We would like to highlight that due to the low mass of boron and nitrogen atoms, hBN possesses the highest known optical phonon frequencies. Moreover, although the hBN LO frequency is generally not observed in planar forms
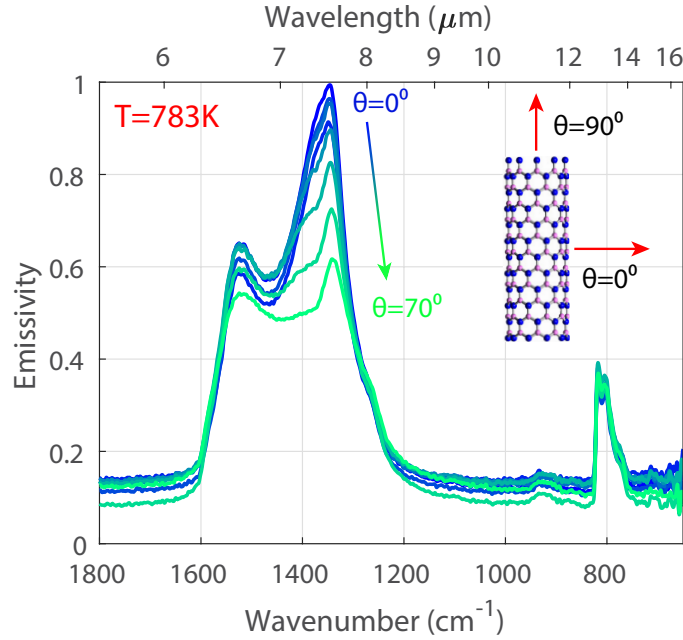
Figure 5.8: Angular dependence of $\vec{E}_x$ polarized BNNT emissivity at 783 K.

of the material, it is present in the tubular form of BNNTs. To our knowledge, the T mode present in the emissivity spectrum of our BNNT system is the highest frequency thermal polariton mode ever measured, making it an excellent candidate for high temperature thermal photonics. A proposed system that would isolate the emission of this T mode from its neighboring L mode is a forest of vertically standing BNNTs. In such a device, The L mode emission would radiate parallel to the samples plane with the T and RB modes propagating normal to the sample ($\theta = 0°$). The theoretical absorption/emission efficiency of this proposed system at normal incidence is shown in figure 5.9.

With interest in BNNTs expanding, we believe the measured emissivity spectrum and antenna behavior will prove valuable, especially for researchers exploring the potential of this exciting material for extreme environment and high temperature applications.
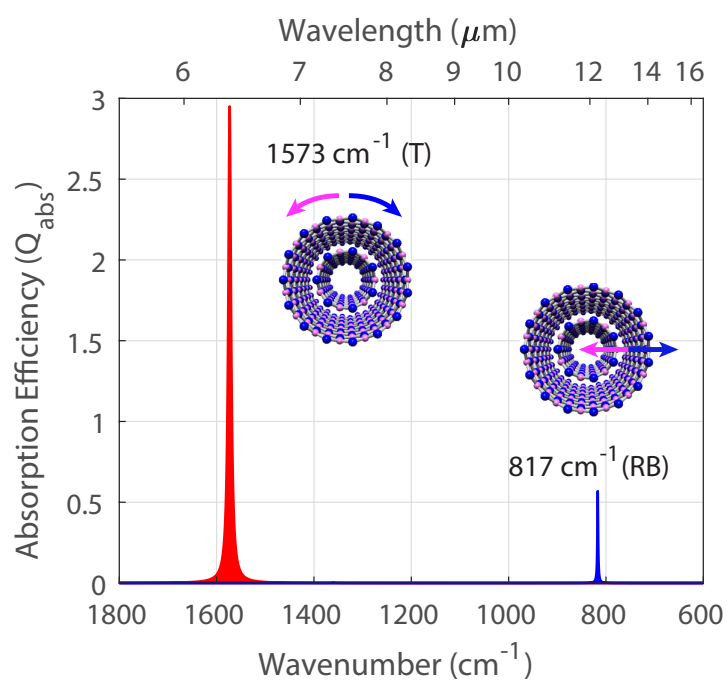
Figure 5.9: Theoretical absorption efficiency of vertically aligned BNNT forest.

Chapter 6

Summary

Complete control of thermal energy and radiation remains an open and challenging problem to this day. However, the results of this thesis show that the future of thermal photonics is bright. Here, we will summarize the findings and contributions presented in the former chapters.

Our study began in Chapter 1 where we discussed the fundamental physics of polaritons that we use to engineer resonances and control light matter interactions. The concept of emissivity was introduced to describe how thermal energy is lost to radiation. The thesis and field of thermal photonics was motivated here by introducing the technologies of passive radiative cooling and thermophotovoltaics.

Chapter 2 began by looking at plasmonic resonances in 2D metallic nanowire metamaterials. We show strong plasmon polaritonic resonances can be engineered to enhance visible frequency absorption. The behavior of the metamaterial is simulated using effective medium theory as well as full wave simulations with commercial software. Key results from this chapter include:

- Strong visible frequency absorption resonances can be engineering using plasmonic nanowire metamaterial designs.

- The strong absorption resonances in nanowire metamaterial can have superior performance over multilayer metamaterials.

- The low melting point of metals limits the applicability of plasmonic metamaterials.

75

In Chapter 3, we move to a polar ceramic material system that also supports polaritonic oscillations. A 2D bi-periodic grating is patterned in to a SiC wafer to couple bound surface phonon polaritons with free space. Notable achievements include:

- Demonstration of dual-band thermal emission within the Reststrahlen band of SiC.

- Angularly dependent measurements show the dispersive behavior of surface waves and agree well with simulations.

Chapter 4 looks at the potential of LSPhP as thermal emitters. SiO_2 and SiC μ-particles are deposited on a low-e substrate to obtain thermal emission measurements and calculate emissivity spectra. These emission measurements are compared with absorption measurements as well as Mie theory simulations and show strong agreement. This work shows:

- SiO_2 and SiC μ particles can be used as strong emitters of thermal radiation.

- Their polaritonic resonances overlap well with the atmospheric transmission window, suggesting they are well suited for passive radiative cooling applications.

- Cooling to temperatures $\approx 6°C$ below ambient could be achieved with such designs.

Chapter 5 explores the unique material system of BNNTs for high temperature, high-frequency optcial phonon thermal emission. Through thermal emission and absorption measurements, we are able to investigate the strong anisotropic behavior of BNNT phononic modes. The findings of this work show:

- BNNTs possess the highest known optical phonon frequecies to date.

- BNNTs show strong radiative properties in extremem environments up to $(938K)$.

References

[1] J.-J. Greffet and M. Nieto-Vesperinas, "Field theory for generalized bidirectional reflectivity: Derivation of helmholtz's reciprocity principle and kirchhoff's law," *J. Opt. Soc. Am. A*, vol. 15, no. 10, pp. 2735–2744, Oct. 1998. DOI: `10.1364/JOSAA.15.002735`. [Online]. Available: `http://josaa.osa.org/abstract.cfm?URI=josaa-15-10-2735`.   2, 68

[2] X. Liu, T. Tyler, T. Starr, A. F. Starr, N. M. Jokerst, and W. J. Padilla, "Taming the blackbody with infrared metamaterials as selective thermal emitters," *Phys. Rev. Lett.*, vol. 107, p. 045 901, 4 Jul. 2011. DOI: `10.1103/PhysRevLett.107.045901`.   2, 34

[3] P. N. Dyachenko, S. Molesky, A. Y. Petrov, M. Störmer, T. Krekeler, S. Lang, M. Ritter, Z. Jacob, and M. Eich, "Controlling thermal emission with refractory epsilon-near-zero metamaterials via topological transitions," *Nature Communications*, no. 7, Jun. 2016. DOI: `10.1038/ncomms11809`.   2, 34, 49, 62

[4] F. Marquier, C. Arnold, M. Laroche, J. J. Greffet, and Y. Chen, "Degree of polarization of thermal light emitted by gratings supporting surface waves," *Opt. Express*, vol. 16, no. 8, pp. 5305–5313, Apr. 2008. DOI: `10.1364/OE.16.005305`. [Online]. Available: `http://www.opticsexpress.org/abstract.cfm?URI=oe-16-8-5305`.   2, 43

[5] N. Dahan, A. Niv, G. Biener, Y. Gorodetski, V. Kleiner, and E. Hasman, "Extraordinary coherent thermal emission from sic due to coupled resonant cavities," *Journal of Heat Transfer*, vol. 130, pp. 112401-1-112401-5, 11 Sep. 2008. DOI: `10.1115/1.2955475`. [Online]. Available: `http://dx.doi.org/10.1115/1.2955475`.   2, 62

[6] J.-J. Greffet, R. Carminati, K. Joulain, J.-P. Mulet, S. Mainguy, and Y. Chen, "Coherent emission of light by thermal sources," *Nature*, vol. 416, pp. 61–64, 2002. DOI: `10.1038/416061a`.   2, 34, 36, 37, 49, 62

[7] Y. Nam, Y. X. Yeng, A. Lenert, P. Bermel, I. Celanovic, M. Soljačić, and E. N. Wang, "Solar thermophotovoltaic energy conversion systems with two-dimensional tantalum photonic crystal absorbers and emitters," *Solar Energy Materials and Solar Cells*, vol. 122, no. Supplement C, pp. 287–296, 2014, ISSN: 0927-0248. DOI: `https://doi.org/10.1016/j.solmat.2013.12.012`. [Online]. Available: `http://www.sciencedirect.com/science/article/pii/S0927024813006454`.   2, 34

[8]   B. Zhao, L. Wang, Y. Shuai, and Z. Zhang, "Thermophotovoltaic emit-
ters based on a two-dimensional grating/thin-film nanostructure," *In-
ternational Journal of Heat and Mass Transfer*, vol. 67, pp. 637–645,
2013, ISSN: 0017-9310. DOI: `10.1016/j.ijheatmasstransfer.2013.`
`08.047`.   2, 34

[9]   A. P. Raman, M. A. Anoma, L. Zhu, E. Rephaeli, and S. Fan, "Passive
radiative cooling below ambient air temperature under direct sunlight,"
Nature, vol. 515, pp. 540–544, 2014, ISSN: 0030-4018. DOI: `10.1038/`
`nature13883`. [Online]. Available: `http://dx.doi.org/10.1038/`
`nature13883`.   2, 34, 59, 62

[10] Y. Zhai, Y. Ma, S. N. David, D. Zhao, R. Lou, G. Tan, R. Yang, and X.
Yin, "Scalable-manufactured randomized glass-polymer hybrid meta-
material for daytime radiative cooling," *Science*, vol. 355, no. 6329,
pp. 1062–1066, 2017, ISSN: 0036-8075. DOI: `10.1126/science.aai7899`.
eprint: `http://science.sciencemag.org/content/355/6329/1062.`
`full.pdf`. [Online]. Available: `http://science.sciencemag.org/`
`content/355/6329/1062`.   2, 49, 59, 62

[11] J. Liu, U. Guler, A. Lagutchev, A. Kildishev, O. Malis, A. Boltasseva,
and V. M. Shalaev, "Quasi-coherent thermal emitter based on refrac-
tory plasmonic materials," *Opt. Mater. Express*, vol. 5, no. 12, pp. 2721–
2728, Dec. 2015. DOI: `10.1364/OME.5.002721`. [Online]. Available:
`http://www.osapublishing.org/ome/abstract.cfm?URI=ome-5-`
`12-2721`.   2, 34, 49

[12] J. A. Schuller, T. Taubner, and M. L. Brongersma, "Optical antenna
thermal emitters," *Nature Photonics*, vol. 3, pp. 658–661, 2009. DOI:
`10.1038/nphoton.2009.188`. [Online]. Available: `https://doi.org/`
`10.1038/nphoton.2009.188`.   2, 49, 62

[13] "The role of refrigeration in the global economy," International Insti-
tute of Refrigeration, 2015. [Online]. Available: `http://www.iifiir.`
`org/userfiles/file/publications/notes/NoteTech_29_EN.pdf`.   3

[14] "The future of cooling opportunities for energy-efficient air condition-
ing," International Energy Agency, 2018. [Online]. Available: `https:`
`//webstore.iea.org/the-future-of-cooling`.   3

[15] M. A. Rosen and I. Dincer, "Exergoeconomic analysis of power plants
operating on various fuels," *Applied Thermal Engineering*, vol. 23, no. 6,
pp. 643–658, 2003, ISSN: 1359-4311. DOI: `DOI:101016/S1359-4311(02)`
`00244-2`. [Online]. Available: `http://dx.doi.org/10.1016/S1359-`
`4311(02)00244-2`.   4

[16] U. Buskies, "The efficiency of coal-fired combined-cycle powerplants,"
Applied Thermal Engineering, vol. 16, no. 12, pp. 959–974, 1996, EU-
ROTHERM Seminar No. 41: Exergoeconomical Analysis and Optimiza-
tion in Chemical Engineering, ISSN: 1359-4311. DOI: `https://doi.org/`

10.1016/1359-4311(96)00001-4. [Online]. Available: `http://www.sciencedirect.com/science/article/pii/1359431196000014`. 4

[17] A. Datas and C. Algora, "Detailed balance analysis of solar thermophotovoltaic systems made up of single junction photovoltaic cells and broadband thermal emitters," *Solar Energy Materials and Solar Cells*, vol. 94, no. 12, pp. 2137–2147, 2010, ISSN: 0927-0248. DOI: `https://doi.org/10.1016/j.solmat.2010.06.042`. [Online]. Available: `http://www.sciencedirect.com/science/article/pii/S092702481000406X`. 4

[18] D. N. Woolf, E. A. Kadlec, D. Bethke, A. D. Grine, J. J. Nogan, J. G. Cederberg, D. B. Burckel, T. S. Luk, E. A. Shaner, and J. M. Hensley, "High-efficiency thermophotovoltaic energy conversion enabled by a metamaterial selective emitter," *Optica*, vol. 5, no. 2, pp. 213–218, Feb. 2018. DOI: `10.1364/OPTICA.5.000213`. [Online]. Available: `http://www.osapublishing.org/optica/abstract.cfm?URI=optica-5-2-213`. 5

[19] E. Rephaeli and S. Fan, "Absorber and emitter for solar thermo-photovoltaic systems to achieve efficiency exceeding the shockley-queisser limit," *Opt. Express*, vol. 17, no. 17, pp. 15 145–15 159, Aug. 2009. DOI: `10.1364/OE.17.015145`. [Online]. Available: `http://www.opticsexpress.org/abstract.cfm?URI=oe-17-17-15145`. 5, 62

[20] G. Mie, "Beiträge zur optik trüber medien, speziell kolloidaler metallösungen," *Annalen der Physik*, vol. 330, no. 3, pp. 377–445, 1908. DOI: `10.1002/andp.19083300302`. eprint: `https://onlinelibrary.wiley.com/doi/pdf/10.1002/andp.19083300302`. [Online]. Available: `https://onlinelibrary.wiley.com/doi/abs/10.1002/andp.19083300302`. 14, 48, 51, 52

[21] R. J. Pollard, A. Murphy, W. R. Hendren, P. R. Evans, R. Atkinson, G. A. Wurtz, A. V. Zayats, and V. A. Podolskiy, "Optical nonlocalities and additional waves in epsilon-near-zero metamaterials," *Phys. Rev. Lett.*, vol. 102, p. 127 405, 12 Mar. 2009. DOI: `10.1103/PhysRevLett.102.127405`. [Online]. Available: `https://link.aps.org/doi/10.1103/PhysRevLett.102.127405`. 18, 29, 30, 32

[22] S. Molesky, C. J. Dewalt, and Z. Jacob, "High temperature epsilon-near-zero and epsilon-near-pole metamaterial emitters for thermophotovoltaics," *Opt. Express*, vol. 21, no. S1, A96–A110, Jan. 2013. DOI: `10.1364/OE.21.000A96`. 18, 20, 21, 34, 49, 62

[23] P. Evans, W. R. Hendren, R. Atkinson, G. A. Wurtz, W. Dickson, A. V. Zayats, and R. J. Pollard, "Growth and properties of gold and nickel nanorods in thin film alumina," *Nanotechnology*, vol. 17, p. 5746, 23 Sep. 2006. 18, 19, 24

[24] M. A. Noginov, Y. A. Barnakov, G. Zhu, T. Tumkur, H. Li, and E. E. Narimanov, "Bulk photonic metamaterial with hyperbolic dispersion," *Applied Physics Letters*, vol. 94, no. 15, p. 151 105, 2009. DOI: `10.1063/1.3115145`. eprint: `https://doi.org/10.1063/1.3115145`. [Online]. Available: `https://doi.org/10.1063/1.3115145`.   18, 19

[25] C. Argyropoulos, N. M. Estakhri, F. Monticone, and A. Alù, "Negative refraction, gain and nonlinear effects in hyperbolic metamaterials," *Opt. Express*, vol. 21, no. 12, pp. 15 037–15 047, Jun. 2013. DOI: `10.1364/OE.21.015037`. [Online]. Available: `http://www.opticsexpress.org/abstract.cfm?URI=oe-21-12-15037`.   18

[26] A. V. Kabashin, P. Evans, S. Pastkovsky, W. Hendren, G. A. Wurtz, R. Atkinson, R. Pollard, V. A. Podolskiy, and A. V. Zayats, "Plasmonic nanorod metamaterials for biosensing," *Nature Materials*, vol. 8, pp. 867–871, Oct. 2009. DOI: `10.1038/nmat2546`. [Online]. Available: `https://www.nature.com/articles/nmat2546#supplementary-information`.   18

[27] N. Abdallah, F. Castella, F. Delebecque-Fendt, and F. Méhats, "The strongly confined schrödinger–poisson system for the transport of electrons in a nanowire," *SIAM Journal on Applied Mathematics*, vol. 69, no. 4, pp. 1162–1173, 2009. DOI: `10.1137/080715950`. eprint: `https://doi.org/10.1137/080715950`. [Online]. Available: `https://doi.org/10.1137/080715950`.   18

[28] B. D. F. Casse, W. T. Lu, Y. J. Huang, E. Gultepe, L. Menon, and S. Sridhar, "Super-resolution imaging using a three-dimensional metamaterials nanolens," *Applied Physics Letters*, vol. 96, no. 2, p. 023 114, 2010. DOI: `10.1063/1.3291677`. eprint: `https://doi.org/10.1063/1.3291677`. [Online]. Available: `https://doi.org/10.1063/1.3291677`.   18

[29] L. V. Alekseyev, E. E. Narimanov, T. Tumkur, H. Li, Y. A. Barnakov, and M. A. Noginov, "Uniaxial epsilon-near-zero metamaterial for angular filtering and polarization control," *Applied Physics Letters*, vol. 97, no. 13, p. 131 107, 2010. DOI: `10.1063/1.3469925`. eprint: `https://doi.org/10.1063/1.3469925`. [Online]. Available: `https://doi.org/10.1063/1.3469925`.   18

[30] H. Wang, X. Liu, L. Wang, and Z. Zhang, "Anisotropic optical properties of silicon nanowire arrays based on the effective medium approximation," *International Journal of Thermal Sciences*, vol. 65, pp. 62–69, 2013, ISSN: 1290-0729. DOI: `https://doi.org/10.1016/j.ijthermalsci.2012.08.018`. [Online]. Available: `http://www.sciencedirect.com/science/article/pii/S1290072912002426`.   18, 21, 49

[31] M. S. Mirmoosa and C. Simovski, "Micron-gap thermophotovoltaic systems enhanced by nanowires," *Photonics and Nanostructures - Fundamentals and Applications*, vol. 13, pp. 20–30, 2015, ISSN: 1569-4410. DOI: `https://doi.org/10.1016/j.photonics.2014.10.007`. [Online]. Available: `http://www.sciencedirect.com/science/article/pii/S1569441014000923`. 18, 21

[32] C. R. Simovski, P. A. Belov, A. V. Atrashchenko, and Y. S. Kivshar, "Wire metamaterials: Physics and applications," *Advanced Materials*, vol. 24, no. 31, pp. 4229–4248, 2012. DOI: `10.1002/adma.201200931`. eprint: `https://onlinelibrary.wiley.com/doi/pdf/10.1002/adma.201200931`. [Online]. Available: `https://onlinelibrary.wiley.com/doi/abs/10.1002/adma.201200931`. 18, 20, 21

[33] S.-A. Biehs, M. Tschikin, R. Messina, and P. Ben-Abdallah, "Superplanckian near-field thermal emission with phonon-polaritonic hyperbolic metamaterials," *Applied Physics Letters*, vol. 102, no. 13, p. 131 106, 2013. DOI: `10.1063/1.4800233`. eprint: `https://doi.org/10.1063/1.4800233`. [Online]. Available: `https://doi.org/10.1063/1.4800233`. 18, 21

[34] L. Menon, W. T. Lu, A. L. Friedman, S. P. Bennett, D. Heiman, and S. Sridhar, "Negative index metamaterials based on metal-dielectric nanocomposites for imaging applications," *Applied Physics Letters*, vol. 93, no. 12, p. 123 117, 2008. DOI: `10.1063/1.2945647`. eprint: `https://doi.org/10.1063/1.2945647`. [Online]. Available: `https://doi.org/10.1063/1.2945647`. 19

[35] J. Kanungo and J. Schilling, "Experimental determination of the principal dielectric functions in silver nanowire metamaterials," *Applied Physics Letters*, vol. 97, no. 2, p. 021 903, 2010. DOI: `10.1063/1.3462311`. eprint: `https://doi.org/10.1063/1.3462311`. [Online]. Available: `https://doi.org/10.1063/1.3462311`. 19

[36] Y. Jie, W. Yuan, T. Kun-Tong, L. Zhaowei, Y. Xiaobo, B. Guy, S. A. M., W. Yuh-Lin, and Z. Xiang, "Design, fabrication and characterization of indefinite metamaterials of nanowires," *Philosophical Transactions of the Royal Society A: Mathematical, Physical and Engineering Sciences*, vol. 369, pp. 3434–3446, 2011. DOI: `10.1098/rsta.2011.0159`. eprint: `https://doi.org/10.1098/rsta.2011.0159`. [Online]. Available: `https://doi.org/10.1098/rsta.2011.0159`. 19

[37] P. R. Evans, R. Kullock, W. R. Hendren, R. Atkinson, R. J. Pollard, and L. M. Eng, "Optical transmission properties and electric field distribution of interacting 2d silver nanorod arrays," *Advanced Functional Materials*, vol. 18, no. 7, pp. 1075–1079, 2008. DOI: `10.1002/adfm.200701289`. eprint: `https://onlinelibrary.wiley.com/doi/pdf/10.1002/adfm.200701289`. [Online]. Available: `https://onlinelibrary.wiley.com/doi/abs/10.1002/adfm.200701289`. 19

[38] B. M. Wells, C. M. Roberts, and V. A. Podolskiy, "Metamaterials-based salisbury screens with reduced angular sensitivity," *Applied Physics Letters*, vol. 105, no. 16, p. 161 105, 2014. DOI: 10.1063/1.4899131. eprint: https://doi.org/10.1063/1.4899131. [Online]. Available: https://doi.org/10.1063/1.4899131.   19, 21

[39] Computer Simulation Technology, *Cst microwave studio*. [Online]. Available: https://www.cst.com.   19

[40] A. Poddubny, I. Iorsh, P. Belov, and Y. Kivshar, "Hyperbolic metamaterials," *Nature Photonics*, vol. 7, 948 EP -, Nov. 2013, Review Article. [Online]. Available: https://doi.org/10.1038/nphoton.2013.243.   20

[41] F. Monticone and A. Alù, "Metamaterials and plasmonics: From nanoparticles to nanoantenna arrays, metasurfaces, and metamaterials," *Chinese Physics B*, vol. 23, no. 4, p. 047 809, 2014. [Online]. Available: http://stacks.iop.org/1674-1056/23/i=4/a=047809.   20

[42] B. M. Wells, A. V. Zayats, and V. A. Podolskiy, "Nonlocal optics of plasmonic nanowire metamaterials," *Phys. Rev. B*, vol. 89, p. 035 111, 3 Jan. 2014. DOI: 10.1103/PhysRevB.89.035111. [Online]. Available: https://link.aps.org/doi/10.1103/PhysRevB.89.035111.   20

[43] K.-T. Tsai, G. A. Wurtz, J.-Y. Chu, T.-Y. Cheng, H.-H. Wang, A. V. Krasavin, J.-H. He, B. M. Wells, V. A. Podolskiy, J.-K. Wang, Y.-L. Wang, and A. V. Zayats, "Looking into meta-atoms of plasmonic nanowire metamaterial," *Nano Letters*, vol. 14, no. 9, pp. 4971–4976, 2014, PMID: 25115592. DOI: 10.1021/nl501283c. eprint: https://doi.org/10.1021/nl501283c. [Online]. Available: https://doi.org/10.1021/nl501283c.   20

[44] P. Shekhar, J. Atkinson, and Z. Jacob, "Hyperbolic metamaterials: Fundamentals and applications," *Nano Convergence*, vol. 1, no. 1, p. 14, Jun. 2014, ISSN: 2196-5404. DOI: 10.1186/s40580-014-0014-6. [Online]. Available: https://doi.org/10.1186/s40580-014-0014-6.   20, 63

[45] Y. Liu, G. Bartal, and X. Zhang, "All-angle negative refraction and imaging in a bulk medium made of metallic nanowires in the visible region," *Opt. Express*, vol. 16, no. 20, pp. 15 439–15 448, Sep. 2008. DOI: 10.1364/OE.16.015439. [Online]. Available: http://www.opticsexpress.org/abstract.cfm?URI=oe-16-20-15439.   22

[46] K. H. Lee and C. C. Wong, "Decoupling two-step anodization in anodic aluminum oxide," *Journal of Applied Physics*, vol. 106, no. 10, p. 104 305, 2009. DOI: 10.1063/1.3257261. eprint: https://doi.org/10.1063/1.3257261. [Online]. Available: https://doi.org/10.1063/1.3257261.   24

[47] M. J. Liew, S. Roy, and K. Scott, "Development of a non-toxic electrolyte for soft gold electrodeposition: An overview of work at university of newcastle upon tyne," *Green Chem.*, vol. 5, pp. 376–381, 4 2003. DOI: `10.1039/B301176N`. [Online]. Available: `http://dx.doi.org/10.1039/B301176N`. 24

[48] J. A. BEARDEN, "X-ray wavelengths," *Rev. Mod. Phys.*, vol. 39, pp. 78–124, 1 Jan. 1967. DOI: `10.1103/RevModPhys.39.78`. [Online]. Available: `https://link.aps.org/doi/10.1103/RevModPhys.39.78`. 27

[49] S. Campione, D. de Ceglia, M. A. Vincenti, M. Scalora, and F. Capolino, "Electric field enhancement in ε-near-zero slabs under tm-polarized oblique incidence," *Phys. Rev. B*, vol. 87, p. 035 120, 3 Jan. 2013. DOI: `10.1103/PhysRevB.87.035120`. [Online]. Available: `https://link.aps.org/doi/10.1103/PhysRevB.87.035120`. 30

[50] S. Pendharker, H. Hu, S. Molesky, R. Starko-Bowes, Z. Poursoti, S. Pramanik, N. Nazemifard, R. Fedosejevs, T. Thundat, and Z. Jacob, "Thermal graphene metamaterials and epsilon-near-zero high temperature plasmonics," *Journal of Optics*, vol. 19, no. 5, p. 055 101, 2017. [Online]. Available: `http://stacks.iop.org/2040-8986/19/i=5/a=055101`. 34, 49, 62

[51] C. Arnold, F. ˜. Marquier, M. Garin, F. Pardo, S. Collin, N. Bardou, J.-L. Pelouard, and J.-J. Greffet, "Coherent thermal infrared emission by two-dimensional silicon carbide gratings," *Phys. Rev. B*, vol. 86, p. 035 316, 3 Jul. 2012. DOI: `10.1103/PhysRevB.86.035316`. [Online]. Available: `https://link.aps.org/doi/10.1103/PhysRevB.86.035316`. 34, 36, 42, 43, 49, 64

[52] F. Han, X. Sun, L. Wu, and Q. Li, "Dual-wavelength orthogonally polarized radiation generated by a tungsten thermal source," *Opt. Express*, vol. 21, no. 23, pp. 28 570–28 582, Nov. 2013. DOI: `10.1364/OE.21.028570`. [Online]. Available: `http://www.opticsexpress.org/abstract.cfm?URI=oe-21-23-28570`. 34

[53] M. Laroche, C. Arnold, F. Marquier, R. Carminati, J.-J. Greffet, S. Collin, N. Bardou, and J.-L. Pelouard, "Highly directional radiation generated by a tungsten thermal source," *Opt. Lett.*, vol. 30, no. 19, pp. 2623–2625, Oct. 2005. DOI: `10.1364/OL.30.002623`. [Online]. Available: `http://ol.osa.org/abstract.cfm?URI=ol-30-19-2623`. 34

[54] Y.-B. Chen and Z. Zhang, "Design of tungsten complex gratings for thermophotovoltaic radiators," *Optics Communications*, vol. 269, no. 2, pp. 411–417, 2007, ISSN: 0030-4018. DOI: `https://doi.org/10.1016/j.optcom.2006.08.040`. [Online]. Available: `http://www.sciencedirect.com/science/article/pii/S0030401806008546`. 34

[55] H. T. Miyazaki, K. Ikeda, T. Kasaya, K. Yamamoto, Y. Inoue, K. Fujimura, T. Kanakugi, M. Okada, K. Hatade, and S. Kitagawa, "Thermal emission of two-color polarized infrared waves from integrated plasmon cavities," *Applied Physics Letters*, vol. 92, no. 14, p. 141 114, 2008. DOI: 10.1063/1.2906375. eprint: https://doi.org/10.1063/1.2906375. [Online]. Available: https://doi.org/10.1063/1.2906375.   34

[56] V. Rinnerbauer, Y. X. Yeng, W. R. Chan, J. J. Senkevich, J. D. Joannopoulos, M. Soljačić, and I. Celanovic, "High-temperature stability and selective thermal emission of polycrystalline tantalum photonic crystals," *Opt. Express*, vol. 21, no. 9, pp. 11 482–11 491, May 2013. DOI: 10.1364/OE.21.011482. [Online]. Available: http://www.opticsexpress.org/abstract.cfm?URI=oe-21-9-11482.   34, 49

[57] Y. Guo, C. L. Cortes, S. Molesky, and Z. Jacob, "Broadband superplanckian thermal emission from hyperbolic metamaterials," *Applied Physics Letters*, vol. 101, no. 13, p. 131 106, 2012. DOI: 10.1063/1.4754616.   34, 49, 63

[58] B. N. III, C. Wu, G. T. Eyck, M. Sinclair, I. Brener, and G. Shvets, "Efficient infrared thermal emitters based on low-albedo polaritonic meta-surfaces," *Applied Physics Letters*, vol. 102, no. 21, p. 211 111, 2013. DOI: 10.1063/1.4808086. eprint: http://dx.doi.org/10.1063/1.4808086. [Online]. Available: http://dx.doi.org/10.1063/1.4808086.   34

[59] O. Ilic, P. Bermel, G. Chen, J. D. Joannopoulos, I. Celanovic, and M. Soljačić, "Tailoring high-temperature radiation and the resurrection of the incandescent source," *Nature Nanotechnology*, vol. 11, pp. 320–324, Jan. 2016. DOI: 10.1038/nnano.2015.309. [Online]. Available: http://dx.doi.org/10.1038/nnano.2015.309.   34

[60] P. Bermel, M. Ghebrebrhan, M. Harradon, Y. X. Yeng, I. Celanovic, J. D. Joannopoulos, and M. Soljačić, "Tailoring photonic metamaterial resonances for thermal radiation," *Nanoscale Research Letters*, vol. 6, no. 1, p. 549, Oct. 2011, ISSN: 1556-276X. DOI: 10.1186/1556-276X-6-549. [Online]. Available: https://doi.org/10.1186/1556-276X-6-549.   34

[61] E. Rephaeli, A. Raman, and S. Fan, "Ultrabroadband photonic structures to achieve high-performance daytime radiative cooling," *Nano Letters*, vol. 13, no. 4, pp. 1457–1461, 2013, PMID: 23461597. DOI: 10.1021/nl4004283. [Online]. Available: http://dx.doi.org/10.1021/nl4004283.   34

[62] H. T. Miyazaki, T. Kasaya, M. Iwanaga, B. Choi, Y. Sugimoto, and K. Sakoda, "Dual-band infrared metasurface thermal emitter for co2 sensing," *Applied Physics Letters*, vol. 105, no. 12, p. 121 107, 2014. DOI: 10.1063/1.4896545. eprint: https://doi.org/10.1063/1.4896545. [Online]. Available: https://doi.org/10.1063/1.4896545.   34

[63] S. Edalatpour, J. DeSutter, and M. Francoeur, "Near-field thermal elec-
      tromagnetic transport: An overview," *Journal of Quantitative Spec-
      troscopy and Radiative Transfer*, vol. 178, no. Supplement C, pp. 14–
      21, 2016, Electromagnetic and light scattering by nonspherical particles
      XV: Celebrating 150 years of Maxwell's electromagnetics, ISSN: 0022-
      4073. DOI: `https://doi.org/10.1016/j.jqsrt.2015.12.027`. [On-
      line]. Available: `http://www.sciencedirect.com/science/article/`
      `pii/S0022407315301801`.   34

[64] M. Francoeur, M. P. Mengüç, and R. Vaillon, "Control of near-field
      radiative heat transfer via surface phonon–polariton coupling in thin
      films," *Applied Physics A*, vol. 103, no. 3, pp. 547–550, Jun. 2011, ISSN:
      1432-0630. DOI: `10.1007/s00339-010-6184-0`. [Online]. Available:
      `https://doi.org/10.1007/s00339-010-6184-0`.   34

[65] A. Narayanaswamy, S. Shen, and G. Chen, "Near-field radiative heat
      transfer between a sphere and a substrate," *Phys. Rev. B*, vol. 78,
      p. 115 303, 11 Sep. 2008. DOI: `10.1103/PhysRevB.78.115303`. [On-
      line]. Available: `https://link.aps.org/doi/10.1103/PhysRevB.78.`
      `115303`.   34

[66] J. Li, B. Liu, and S. Shen, "Tunable narrow-band near-field thermal
      emitters based on resonant metamaterials," *Phys. Rev. B*, vol. 96, p. 075 413,
      7 Aug. 2017. DOI: `10.1103/PhysRevB.96.075413`. [Online]. Available:
      `https://link.aps.org/doi/10.1103/PhysRevB.96.075413`.   34

[67] A. Hervé, J. Drevillon, Y. Ezzahri, K. Joulain, D. Meneses, and J.-P.
      Hugonin, "Temperature dependence of a microstructured sic coherent
      thermal source," *Journal of Quantitative Spectroscopy and Radiative
      Transfer*, vol. 180, pp. 29–38, Sep. 2016.   35, 37, 38, 42, 57

[68] J. D. Caldwell, L. Lindsay, V. Giannini, I. Vurgaftman, T. L. Rei-
      necke, S. A. Maier, and O. J. Glembocki, "Low-loss, infrared and tera-
      hertz nanophotonics using surface phonon polaritons. nanophotonics,"
      Nanophotonics, vol. 4, no. 1, pp. 44–68, 2015. DOI: `10.1515/nanoph-`
      `2014-0003`.   36, 49, 51, 62

[69] F. Marquier, K. Joulain, J.-P. Mulet, R. Carminati, J.-J. Greffet, and
      Y. Chen, "Coherent spontaneous emission of light by thermal sources,"
      Phys. Rev. B, vol. 69, p. 155 412, 15 Apr. 2004. DOI: `10.1103/PhysRevB.`
      `69.155412`. [Online]. Available: `https://link.aps.org/doi/10.`
      `1103/PhysRevB.69.155412`.   36

[70] B. Rousseau, J. F. Brun, D. D. S. Meneses, and P. Echegut, "Tempera-
      ture measurement: Christiansen wavelength and blackbody reference,"
      International Journal of Thermophysics, vol. 26, no. 4, pp. 1277–1286,
      Jul. 2005, ISSN: 1572-9567. DOI: `10.1007/s10765-005-6726-4`. [On-
      line]. Available: `https://doi.org/10.1007/s10765-005-6726-4`.
                                                                           37, 42

[71] D. D. S. Meneses, J.-F. Brun, P. Echegut, and P. Simon, "Contribution of semi-quantum dielectric function models to the analysis of infrared spectra," *Applied Spectroscopy*, vol. 58, no. 8, pp. 969–974, 2004. DOI: 10.1366/0003702041655467. [Online]. Available: https://doi.org/10.1366/0003702041655467.   37

[72] S. Link, Z. L. Wang, and M. A. El-Sayed, "Alloy formation of goldsilver nanoparticles and the dependence of the plasmon absorption on their composition," *The Journal of Physical Chemistry B*, vol. 103, no. 18, pp. 3529–3533, 1999. DOI: 10.1021/jp990387w. eprint: https://doi.org/10.1021/jp990387w. [Online]. Available: https://doi.org/10.1021/jp990387w.   48

[73] N. G. Khlebtsov and L. A. Dykman, "Optical properties and biomedical applications of plasmonic nanoparticles," *Journal of Quantitative Spectroscopy and Radiative Transfer*, vol. 111, no. 1, pp. 1–35, 2010, ISSN: 0022-4073. DOI: https://doi.org/10.1016/j.jqsrt.2009.07.012. [Online]. Available: http://www.sciencedirect.com/science/article/pii/S0022407309002581.   48

[74] T. J. Norman, C. D. Grant, D. Magana, J. Z. Zhang, J. Liu, D. Cao, F. Bridges, and A. Van Buuren, "Near infrared optical absorption of gold nanoparticle aggregates," *The Journal of Physical Chemistry B*, vol. 106, no. 28, pp. 7005–7012, 2002. DOI: 10.1021/jp0204197. eprint: https://doi.org/10.1021/jp0204197. [Online]. Available: https://doi.org/10.1021/jp0204197.   48

[75] A. R. Gentle and G. B. Smith, "Radiative heat pumping from the earth using surface phonon resonant nanoparticles," *Nano Letters*, vol. 10, no. 2, pp. 373–379, 2010, PMID: 20055479. DOI: 10.1021/nl903271d. eprint: https://doi.org/10.1021/nl903271d. [Online]. Available: https://doi.org/10.1021/nl903271d.   49

[76] S. Atiganyanun, J. B. Plumley, S. J. Han, K. Hsu, J. Cytrynbaum, T. L. Peng, S. M. Han, and S. E. Han, "Effective radiative cooling by paint-format microsphere-based photonic random media," *ACS Photonics*, vol. 5, no. 4, pp. 1181–1187, 2018. DOI: 10.1021/acsphotonics.7b01492. eprint: https://doi.org/10.1021/acsphotonics.7b01492. [Online]. Available: https://doi.org/10.1021/acsphotonics.7b01492.   49

[77] H. Mutschke, A. C. Andersen, D. Clément, T. Henning, and G. Peiter, "Infrared properties of SiC particles,", vol. 345, pp. 187–202, May 1999. arXiv: astro-ph/9903031 [astro-ph].   49, 52, 55, 58

[78] M. Laroche, R. Carminati, and J.-J. Greffet, "Coherent thermal antenna using a photonic crystal slab," *Phys. Rev. Lett.*, vol. 96, p. 123 903, 12 Mar. 2006. DOI: 10.1103/PhysRevLett.96.123903. [Online]. Available: https://link.aps.org/doi/10.1103/PhysRevLett.96.123903.   49

[79]   B. J. Lee, C. J. Fu, and Z. M. Zhang, "Coherent thermal emission from one-dimensional photonic crystals," *Applied Physics Letters*, vol. 87, no. 7, p. 071 904, 2005. DOI: `10.1063/1.2010613`. eprint: `https://doi.org/10.1063/1.2010613`. [Online]. Available: `https://doi.org/10.1063/1.2010613`.   49, 62

[80]   R. Starko-Bowes, J. Dai, W. Newman, S. Molesky, L. Qi, A. Satija, Y. Tsui, M. Gupta, R. Fedosejevs, S. Pramanik, Y. Xuan, and Z. Jacob, "Dual-band quasi-coherent radiative thermal source," *Journal of Quantitative Spectroscopy and Radiative Transfer*, vol. 216, pp. 99–104, 2018, ISSN: 0022-4073. DOI: `https://doi.org/10.1016/j.jqsrt.2018.05.010`. [Online]. Available: `http://www.sciencedirect.com/science/article/pii/S0022407317309299`.   49, 55–57, 62, 68, 70

[81]   R. Starko-Bowes, J. Atkinson, W. Newman, H. Hu, T. Kallos, G. Palikaras, R. Fedosejevs, S. Pramanik, and Z. Jacob, "Optical characterization of epsilon-near-zero, epsilon-near-pole, and hyperbolic response in nanowire metamaterials," *J. Opt. Soc. Am. B*, vol. 32, no. 10, pp. 2074–2080, Oct. 2015. DOI: `10.1364/JOSAB.32.002074`. [Online]. Available: `http://josab.osa.org/abstract.cfm?URI=josab-32-10-2074`.   49, 62

[82]   C. Khandekar and Z. Jacob, "Circularly polarized thermal radiation from nonequilibrium coupled antennas," *arXiv e-prints*, arXiv:1812.03359, arXiv:1812.03359, Dec. 2018. arXiv: `1812.03359 [cond-mat.mes-hall]`.   49

[83]   S. A. Dyakov, V. A. Semenenko, N. A. Gippius, and S. G. Tikhodeev, "Magnetic field free circularly polarized thermal emission from a chiral metasurface," *Phys. Rev. B*, vol. 98, p. 235 416, 23 Dec. 2018. DOI: `10.1103/PhysRevB.98.235416`. [Online]. Available: `https://link.aps.org/doi/10.1103/PhysRevB.98.235416`.   49

[84]   W. M. Haynes, *CRC handbook of chemistry and physics*. CRC press, 2014.   49

[85]   Y. Sasaki, Y. Nishina, M. Sato, and K. Okamura, "Optical-phonon states of sic small particles studied by raman scattering and infrared absorption," *Phys. Rev. B*, vol. 40, pp. 1762–1772, 3 Jul. 1989. DOI: `10.1103/PhysRevB.40.1762`. [Online]. Available: `https://link.aps.org/doi/10.1103/PhysRevB.40.1762`.   50, 55, 58

[86]   S. Popova, T. Tolstykh, and V. Vorobev, "Optical characteristics of amorphous quartz in the 1400–200 cm1 region," *Opt. Spectrosc.*, no. 33, pp. 444–445, 1972.   50

[87]   I. H. Malitson, "Interspecimen comparison of the refractive index of fused silica∗,†," *J. Opt. Soc. Am.*, vol. 55, no. 10, pp. 1205–1209, Oct. 1965. DOI: `10.1364/JOSA.55.001205`. [Online]. Available: `http://www.osapublishing.org/abstract.cfm?URI=josa-55-10-1205`.   50

87

[88] H. Fröhlich, *Theory of Dielectrics*. Oxford: Clarendon, 1949.   51

[89] R. Ruppin and R. Englman, "Optical phonons of small crystals," *Reports on Progress in Physics*, vol. 33, no. 1, p. 149, 1970. [Online]. Available: `http://stacks.iop.org/0034-4885/33/i=1/a=304`.   51, 52, 104

[90] C. Matzler, "Matlab functions for mie scattering and absorption," *IAP Res Rep*, vol. 8, Jul. 2002.   52, 102

[91] E. Tervo, Z. Zhang, and B. Cola, "Collective near-field thermal emission from polaritonic nanoparticle arrays," *Phys. Rev. Materials*, vol. 1, p. 015 201, 1 Jun. 2017. DOI: `10.1103/PhysRevMaterials.1.015201`. [Online]. Available: `https://link.aps.org/doi/10.1103/PhysRevMaterials.1.015201`.   55, 58

[92] V. Stelmakh, V. Rinnerbauer, J. D. Joannopoulos, M. Soljačić, I. Celanovic, J. J. Senkevich, C. Tucker, T. Ives, and R. Shrader, "Evolution of sputtered tungsten coatings at high temperature," *Journal of Vacuum Science & Technology A*, vol. 31, no. 6, p. 061 505, 2013. DOI: `10.1116/1.4817813`. eprint: `https://doi.org/10.1116/1.4817813`. [Online]. Available: `https://doi.org/10.1116/1.4817813`.   56

[93] N. Verbrugghe, D. Fasquelle, B. Duponchel, and S. Députier, "Study of tungsten films deposited by dc sputtering dedicated to integrated heaters," *Journal of Vacuum Science & Technology B*, vol. 35, no. 3, p. 031 204, 2017. DOI: `10.1116/1.4981786`. eprint: `https://doi.org/10.1116/1.4981786`. [Online]. Available: `https://doi.org/10.1116/1.4981786`.   56

[94] A. Rubio, J. L. Corkill, and M. L. Cohen, "Theory of graphitic boron nitride nanotubes," *Phys. Rev. B*, vol. 49, pp. 5081–5084, 7 Feb. 1994. DOI: `10.1103/PhysRevB.49.5081`. [Online]. Available: `https://link.aps.org/doi/10.1103/PhysRevB.49.5081`.   62

[95] C. Zhi, Y. Bando, C. Tang, and D. Golberg, "Boron nitride nanotubes," *Materials Science and Engineering: R: Reports*, vol. 70, no. 3, pp. 92–111, 2010, 3rd IEEE International NanoElectronics Conference (INEC), ISSN: 0927-796X. DOI: `https://doi.org/10.1016/j.mser.2010.06.004`. [Online]. Available: `http://www.sciencedirect.com/science/article/pii/S0927796X10000665`.   62

[96] P. Jiang, X. Qian, R. Yang, and L. Lindsay, "Anisotropic thermal transport in bulk hexagonal boron nitride," *Phys. Rev. Materials*, vol. 2, p. 064 005, 6 Jun. 2018. DOI: `10.1103/PhysRevMaterials.2.064005`. [Online]. Available: `https://link.aps.org/doi/10.1103/PhysRevMaterials.2.064005`.   62

[97] C. W. Chang, A. M. Fennimore, A. Afanasiev, D. Okawa, T. Ikuno, H. Garcia, D. Li, A. Majumdar, and A. Zettl, "Isotope effect on the thermal conductivity of boron nitride nanotubes," *Phys. Rev. Lett.*, vol. 97, p. 085 901, 8 Aug. 2006. DOI: `10.1103/PhysRevLett.97.085901`. [Online]. Available: `https://link.aps.org/doi/10.1103/PhysRevLett.97.085901`.   62

[98] J. D. Caldwell, A. V. Kretinin, Y. Chen, V. Giannini, M. M. Fogler, Y. Francescato, C. T. Ellis, J. G. Tischler, C. R. Woods, A. J. Giles, M. Hong, K. Watanabe, T. Taniguchi, S. A. Maier, and K. S. Novoselov, "Sub-diffractional volume-confined polaritons in the natural hyperbolic material hexagonal boron nitride," *Nature Communications*, vol. 5, p. 5221, Oct. 2014. DOI: `10.1038/ncomms6221`. [Online]. Available: `https://doi.org/10.1038/ncomms6221`.   62, 64

[99] X. G. AU - Xu, B. G. Ghamsari, J.-H. Jiang, L. Gilburd, G. O. Andreev, C. Zhi, Y. Bando, D. Golberg, P. Berini, and G. C. Walker, "One-dimensional surface phonon polaritons in boron nitride nanotubes," *Nature Communications*, vol. 5, p. 4782, Aug. 2014. DOI: `10.1038/ncomms5782`. [Online]. Available: `https://doi.org/10.1038/ncomms5782`.   62

[100] J. Ahn, Z. Xu, J. Bang, A. E. L. Allcca, Y. P. Chen, and T. Li, "Stable emission and fast optical modulation of quantum emitters in boron nitride nanotubes," *Opt. Lett.*, vol. 43, no. 15, pp. 3778–3781, Aug. 2018. DOI: `10.1364/OL.43.003778`. [Online]. Available: `http://ol.osa.org/abstract.cfm?URI=ol-43-15-3778`.   62

[101] T. T. Tran, C. Elbadawi, D. Totonjian, C. J. Lobo, G. Grosso, H. Moon, D. R. Englund, M. J. Ford, I. Aharonovich, and M. Toth, "Robust multicolor single photon emission from point defects in hexagonal boron nitride," *ACS Nano*, vol. 10, no. 8, pp. 7331–7338, 2016, PMID: 27399936. DOI: `10.1021/acsnano.6b03602`. eprint: `https://doi.org/10.1021/acsnano.6b03602`. [Online]. Available: `https://doi.org/10.1021/acsnano.6b03602`.   62

[102] P. J. Gielisse, S. S. Mitra, J. N. Plendl, R. D. Griffis, L. C. Mansur, R. Marshall, and E. A. Pascoe, "Lattice infrared spectra of boron nitride and boron monophosphide," *Phys. Rev.*, vol. 155, pp. 1039–1046, 3 Mar. 1967. DOI: `10.1103/PhysRev.155.1039`. [Online]. Available: `https://link.aps.org/doi/10.1103/PhysRev.155.1039`.   64

[103] J. Kischkat, S. Peters, B. Gruska, M. Semtsiv, M. Chashnikova, M. Klinkmüller, O. Fedosenko, S. Machulik, A. Aleksandrova, G. Monastyrskyi, Y. Flores, and W. T. Masselink, "Mid-infrared optical properties of thin films of aluminum oxide, titanium dioxide, silicon dioxide, aluminum nitride, and silicon nitride," *Appl. Opt.*, vol. 51, no. 28, pp. 6789–6798, Oct. 2012. DOI: `10.1364/AO.51.006789`. [Online]. Available: `http://ao.osa.org/abstract.cfm?URI=ao-51-28-6789`.   64

[104] H. Vogt and G. Rossbroich, "Accurate determination of the far-infrared dispersion in srtio3 by hyper-raman spectroscopy," *Phys. Rev. B*, vol. 24, pp. 3086–3091, 6 Sep. 1981. DOI: `10.1103/PhysRevB.24.3086`. [Online]. Available: `https://link.aps.org/doi/10.1103/PhysRevB.24.3086`.   64

[105] K. Kamarás, K. Barth, F. Keilmann, R. Henn, M. Reedyk, C. Thomsen, M. Cardona, J. Kircher, P. L. Richards, and J. Stehlé, "The low-temperature infrared optical functions of srtio3 determined by reflectance spectroscopy and spectroscopic ellipsometry," *Journal of Applied Physics*, vol. 78, no. 2, pp. 1235–1240, 1995. DOI: `10.1063/1.360364`. eprint: `https://doi.org/10.1063/1.360364`. [Online]. Available: `https://doi.org/10.1063/1.360364`.   64

[106] F. GERVAIS, "Strontium titanate (srtio3)," in *Handbook of Optical Constants of Solids*, E. D. PALIK, Ed., Boston: Academic Press, 1998, pp. 1035–1047, ISBN: 978-0-12-544422-4. DOI: `https://doi.org/10.1016/B978-0-08-055630-7.50062-6`. [Online]. Available: `http://www.sciencedirect.com/science/article/pii/B9780080556307500626`.   64

[107] G. Shkerdin, S. Rabbaa, J. Stiens, and R. Vounckx, "Free-electron absorption in n-doped GaN semiconductors at mid-IR wavelengths in the strong phonon–plasmon coupling regime," *Journal of Physics D: Applied Physics*, vol. 45, no. 49, p. 495 103, Nov. 2012. DOI: `10.1088/0022-3727/45/49/495103`. [Online]. Available: `https://doi.org/10.1088%5C%2F0022-3727%5C%2F45%5C%2F49%5C%2F495103`.   64

[108] N. Marschall and B. Fischer, "Dispersion of surface polaritons in gap," *Phys. Rev. Lett.*, vol. 28, pp. 811–813, 13 Mar. 1972. DOI: `10.1103/PhysRevLett.28.811`. [Online]. Available: `https://link.aps.org/doi/10.1103/PhysRevLett.28.811`.   64

[109] S. Molesky and Z. Jacob, "Definition of polaritonic fluctuations in natural hyperbolic media," *Phys. Rev. A*, vol. 99, p. 033 833, 3 Mar. 2019. DOI: `10.1103/PhysRevA.99.033833`. [Online]. Available: `https://link.aps.org/doi/10.1103/PhysRevA.99.033833`.   63

[110] C. L. Cortes, W. Newman, S. Molesky, and Z. Jacob, "Quantum nanophotonics using hyperbolic metamaterials," *Journal of Optics*, vol. 14, no. 6, p. 063 001, May 2012. DOI: `10.1088/2040-8978/14/6/063001`. [Online]. Available: `https://doi.org/10.1088%2F2040-8978%2F14%2F6%2F063001`.   63

[111] M. Kerker, *The scattering of light and other electromagnetic radiation*. Academic Press, 1969.   65

[112] C. F. Bohren and D. Huffman, *Absorption and scattering of light by small particles*, ser. Wiley science paperback series. Wiley, 1983, ISBN: 9780471293408. [Online]. Available: `https://books.google.com/books?id=S1RCZ8BjgN0C`.   65, 103, 104

[113] L. Wirtz, A. Rubio, R. A. de la Concha, and A. Loiseau, "Ab initio calculations of the lattice dynamics of boron nitride nanotubes," *Phys. Rev. B*, vol. 68, p. 045 425, 4 Jul. 2003. DOI: `10.1103/PhysRevB.68.045425`. [Online]. Available: `https://link.aps.org/doi/10.1103/PhysRevB.68.045425`.   66

[114] C. H. Lee, J. Wang, V. K. Kayatsha, J. Y. Huang, and Y. K. Yap, "Effective growth of boron nitride nanotubes by thermal chemical vapor deposition," *Nanotechnology*, vol. 19, no. 45, p. 455 605, Oct. 2008. DOI: `10.1088/0957-4484/19/45/455605`. [Online]. Available: `https://doi.org/10.1088%2F0957-4484%2F19%2F45%2F455605`.   66, 68

Appendix A

Detector Calibration

Arguably, the most important measurement in any experiment is the calibration measurement. Without a well calibrated detector, the accuracy of any subsequent measurement is uncertain. Most spectrometers come calibrated or have a calibration source included, such as a mercury lamp for visible spectrometers. In the infrared, a commonly used calibration standard is polystyrene which has a well known IR fingerprint. The Thermo Fisher Scientific is50 FTIR used in these experiments comes with a polystyrene standard included for spectral calibrations.

Another variable that must be calibrated for when calculating emissivity is the responsivity of the detector. This is a more complex procedure and not typically measured by FTIR manufacturers. To calibrate the responsivity of IR detectors, black-body cavity sources are often used as they the theoretical spectral radiance of a black-body is well known. Typically a single measurement is used to calculate the responsivity of a detector and eventually the emissivity of a sample. However, one must be careful when doing this as nonlinearities in detector response can give erroneous results.

In this section we will describe the method used to calibrate our FTIR's mercury cadmium telluride (MCT) detector with a black-body cavity source. Our method will uncover potential nonlinearities while measuring the detector's response function. Figure A.1 shows a picture of our vacuum chamber and FTIR thermal emission experiment.
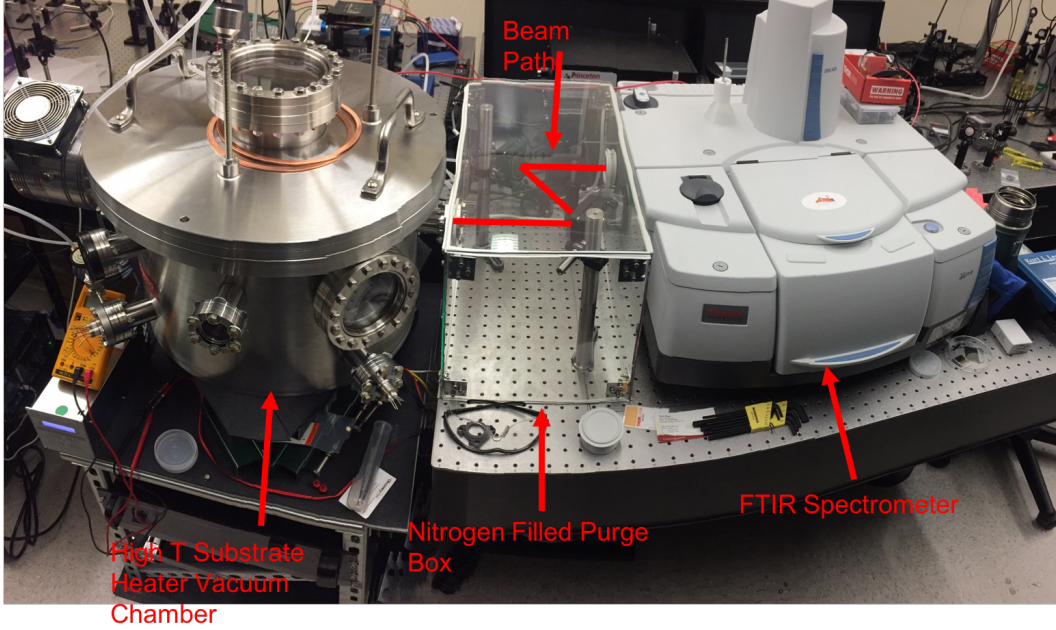
Figure A.1: Picture of vacuum chamber and FTIR thermal emission experimental set up.

A.1 Black-body Cavity Measurement

First we use the raw spectral radiance of the black-body cavity source at temperature ranging from 473 to 1273 K. Because we want to be able to measure polarized thermal emission properties and there are a number of mirrors and beam splitters in the beam path, we need to take calibration measurement for both polarizer orientations, the detector will have a different responsivity to horizontally or vertically polarized light. Figure A.2 shows the raw spectral radiance as measured by the FTIR for different temperatures.

The intensity $I(\lambda, T)$ spectra shown in figure A.2 can be represented by:

$$I(\lambda, T) = R(\lambda)\Omega A_{spot} \frac{2hc^2}{\lambda^5} \frac{1}{e^{\frac{hc}{\lambda k_B T}} - 1} , \tag{A.1}$$

where $R(\lambda)$ is the responsivity of the detector, Ω is the solid angle of collection, A_{spot} is the focal spot size, λ is wavelength, h is the Planck constant, k_B is the Boltzmann constant, c is the speed of light in vacuum and T is the temperature in Kelvin. To calibrate the detector, we need to know its responsivity as a function of wavelength. To do this, we plot the intensity
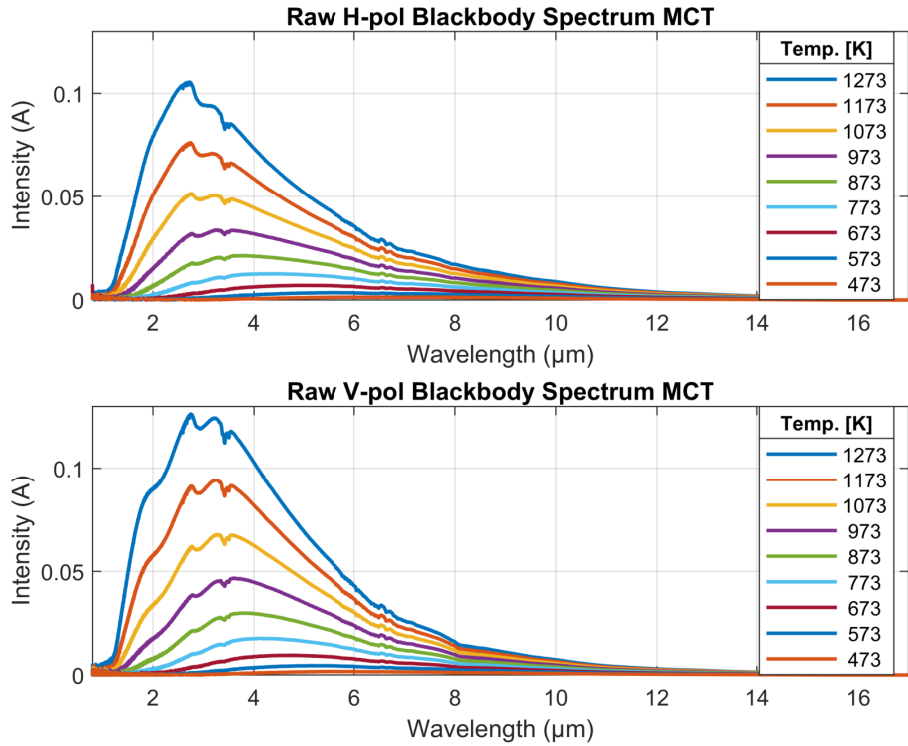
Figure A.2: Raw emission signal collected by FTIR detector for two polarization states of the black-body cavity source at different operating temperatures.

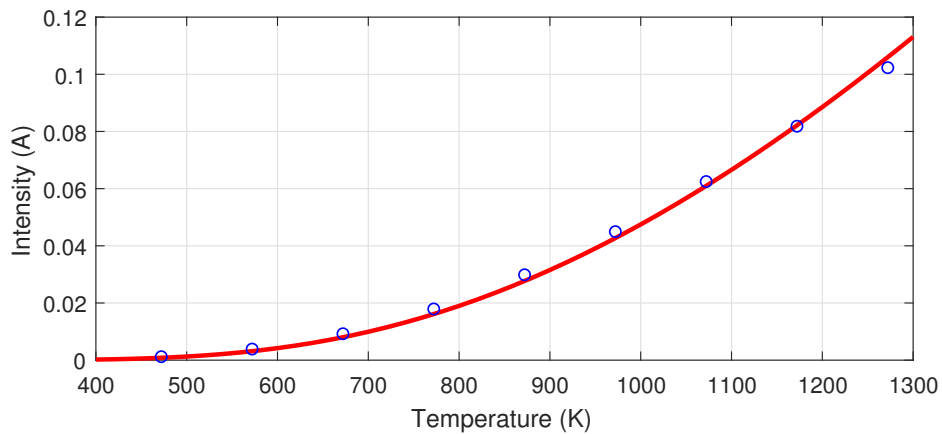detected at a given wavelength as a function of temperature (shown in figure A.3.

Figure A.3: Example of fitting procedure to calibrate responsivity. Intensity of 4 μm light is plotted as a function of temperature.

We can then fit the data points according to equation A.1 using only $R(\lambda)$

94

as our fitting parameter. This fitting procedure is repeated for the entire wavelength space to produce the responsivity function for each polarization, shown in figure A.4.
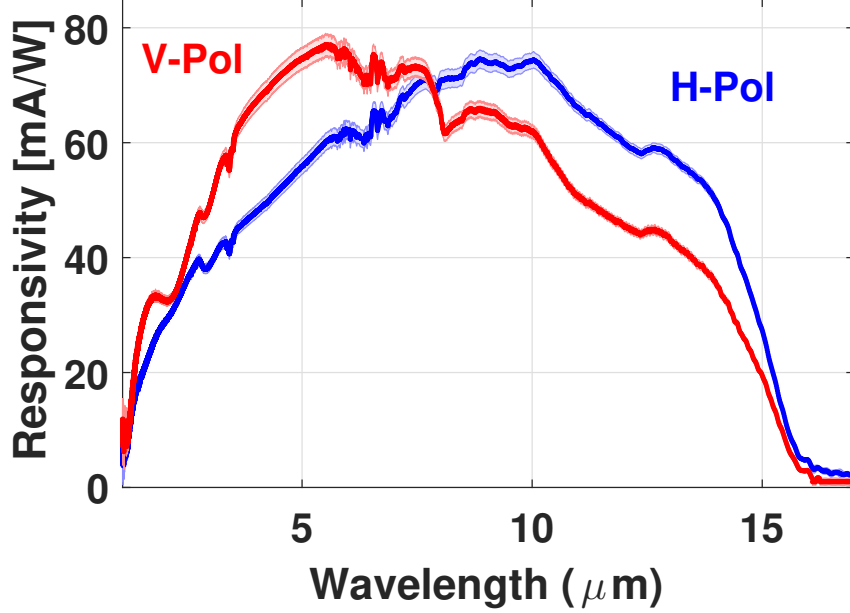

Figure A.4: The response function of the detection system for horizontal (H-Pol) and Vertical (V-Pol) polarized radiation.

Now that the responsivity of the detector for each polarization is known. We can use this to calculate the emissivity spectrum of any arbitrary material or sample. To calculate the emission spectrum of of the black-body cavity source, we plot the calibration corrected emission spectrum in figure A.5 using the equation:

$$I_{BB}(\lambda, T) = \frac{S_{BB}(\lambda, T)}{R(\lambda) \Omega A_{spot}} \ . \tag{A.2}$$

We can now see that for both polarizations, we observe the same spectral radiance which is to be expected if they are measuring the same emission signal. Also plotted in figure A.2 is the theoretical black-body spectral radiance (thin black lines) at the same measured temperatures

$$L(\lambda, T) = \frac{2hc^2}{\lambda^5} \frac{1}{e^{\frac{hc}{\lambda k_B T}} - 1} \ . \tag{A.3}$$
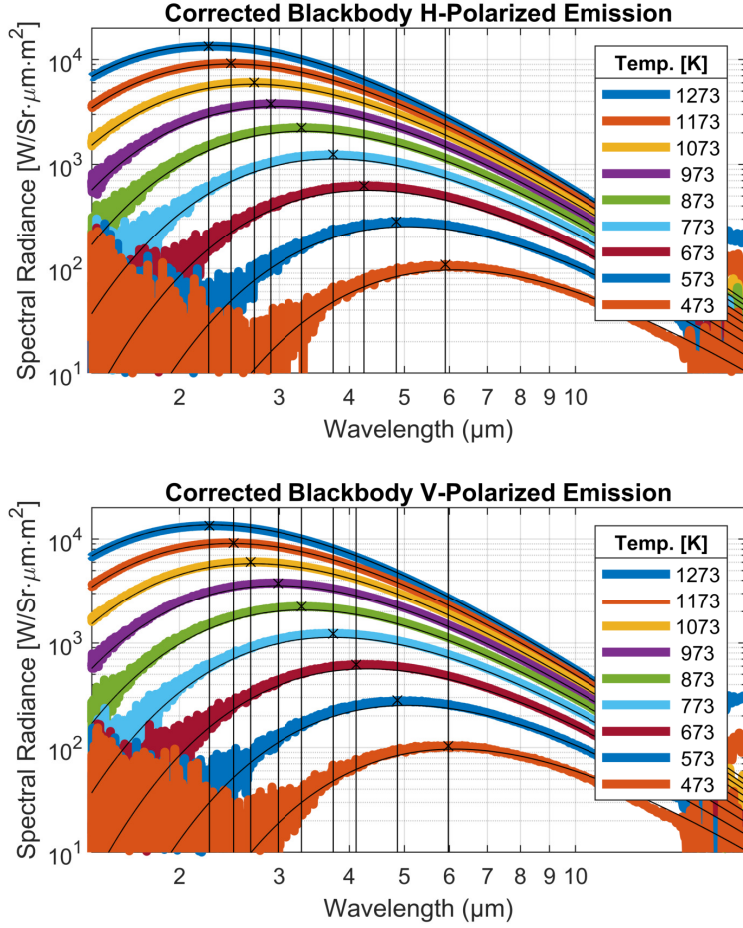
Figure A.5: The emission spectra of the black-body cavity after being corrected using the response function of FTIR detector in figure A.4.

To bolster our confidence in the calibrated responsivity function, we fit the peak emission wavelength as a function of black-body temperature. The relation between peak emission wavelength and temperature for a black-body emitter should follow Wien's displacement law

$$\lambda_{max}(T) = \frac{b}{T} \tag{A.4}$$

where λ_{max} is the peak wavelength at temperature T and $b = 2897.7\mu mK$ is Wein's constant. The peak wavelength for each temperature is fit and marked in figure A.2 with an x and vertical line. These wavelengths (λ_{max}) are then plotted as a function of temperature in figure A.6 as black circles. These

data points are then fit with Wien's law using b as the only free variable. The resulting fit is plotted in figure A.6 as the dashed red line. Also for comparison we included Wiens law using the literature accepted value of $b = 2897.7\mu mK$. We can see our experimentally obtained value for Wein's constant differs by only 2% which is a good agreement.
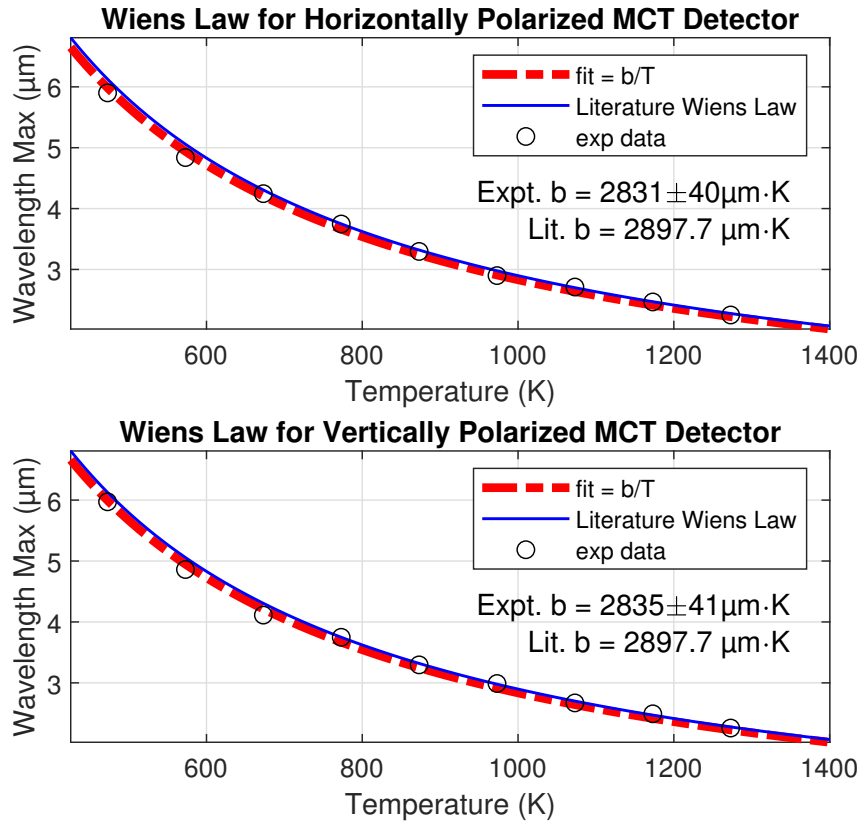

Figure A.6: Wien's displacement law for the MCT detector with two orthogonally polarized signals. The fit value of Wein's constant b is close to that of the literature accepted value for Wein's constant ($b = 2897.7\mu m \cdot K$).

Appendix B

Radiative Cooling

In this appendix we define the terms used in calculations of passive radiative cooling power and spectra. Also described is a calculation for two types of radiative emitters, comparing their cooling power at different temperatures.

B.1 Radiative Cooling Interaction Terms

A radiative cooler will interact with radiation from the sun, the atmosphere and deep space ($\approx$3K). The net cooling power P_{cool} can then be calculated as:

$$P_{cool}(T) = P_{rad}(T_s) - P_{atm}(T_a) - P_{sun} - P_{cond+conv} \qquad \text{(B.1)}$$

Here, $P_{rad}(T)$ is the power radiated out by the radiative cooler at temperature T and can be calculated as:

$$P_{rad}(T_s) = A \int d\Omega cos(\theta) \int_0^\infty d\lambda I_{BB}(\lambda, T_s)\epsilon_{rad}(\lambda, \theta) \qquad \text{(B.2)}$$

Where $\int d\Omega = 2\pi \int_0^{2\pi} d\theta sin(\theta)$ is the angular integral over the hemisphere and θ is the polar angle measured from the zenith. $I_{BB}(T_s) = \frac{2hc^2}{\lambda^5}\frac{1}{e^{hc/\lambda k_b T_s}-1}$ is the spectral radiance of a blackbody at temperature T_s. $\epsilon_{rad}(\lambda, \theta)$ is the emissivity spectrum of the radiative cooler. While it is in general angularly dependent, we will consider non angularly dependent emissivity to simplify the calculation.

$P_{atm}(T_a)$ is the power absorbed by the radiative cooler from the atmosphere and is:

$$P_{atm}(T_a) = A \int d\Omega cos(\theta) \int_0^\infty d\lambda I_{BB}(\lambda, T_a)\epsilon_{rad}(\lambda, \theta)\epsilon_{atm}(\lambda, \theta) \qquad \text{(B.3)}$$

Where $\epsilon_{atm}(\lambda, \theta) = 1 - t(\lambda)^{1/cos(\theta)}$ is the angularly dependent emissivity of the atmosphere and $t(\lambda)$ is the transmission spectrum of the atmosphere.

P_{sun} is the power absorbed by the radiator from the sun and can be calculated as:

$$P_{sun} = \int_0^\infty d\lambda \epsilon_{rad}(\lambda, \theta_{sun}) I_{AM1.5}(\lambda) \qquad \text{(B.4)}$$

Where $I_{AM1.5}(\lambda)$ is the solar spectral irradiance (direct + circumsolar) and θ_{sun} is the fixed angle of the sun, so no integration is required. To simplify the calculation we will assume the radiator is facing the sun such that $\theta_{sun} = 0$.

$P_{cond+conv}$ is the non-radiative energy transfer between the environment and the radiative cooler taking in to account both conduction and convection. It is calculated as follows:

$$P_{cond+conv} = Ah_c(T_a - T_s); \qquad \text{(B.5)}$$

Where $h_c = h_{cond} + h_{conv}$ is the combined non-radiative heat coefficient that accounts for both conductive and convective heat gain. While it is important to consider all terms when calculating total cooling power, $P_{cond+conv}$ does not depend on optical properties of materials. Therefore, it can be neglected when optimizing or comparing net cooling power across designs.

B.1.1 Radiative cooling power

By using the near ideal heat sink of deep space, in principle, one could reach a high energy transfer efficiency ($\eta = (1 - \frac{T_1}{T_2}) * 100\%$). To achieve this, we must target maximal overlap between the radiators emissivity spectrum with the transmission spectrum of the atmosphere. Figure B.1 shows the transmission spectrum of the atmosphere (blue area) as well as the spectral radiance of black-body at 300 K (red line). We can see that there exists a large overlap in the two spectra between approximately 8 and 13 μm. This is often referred

to as the atmospheric transmission window and is typically the spectral region most often targeted to achieve maximal cooling in radiative cooling designs.
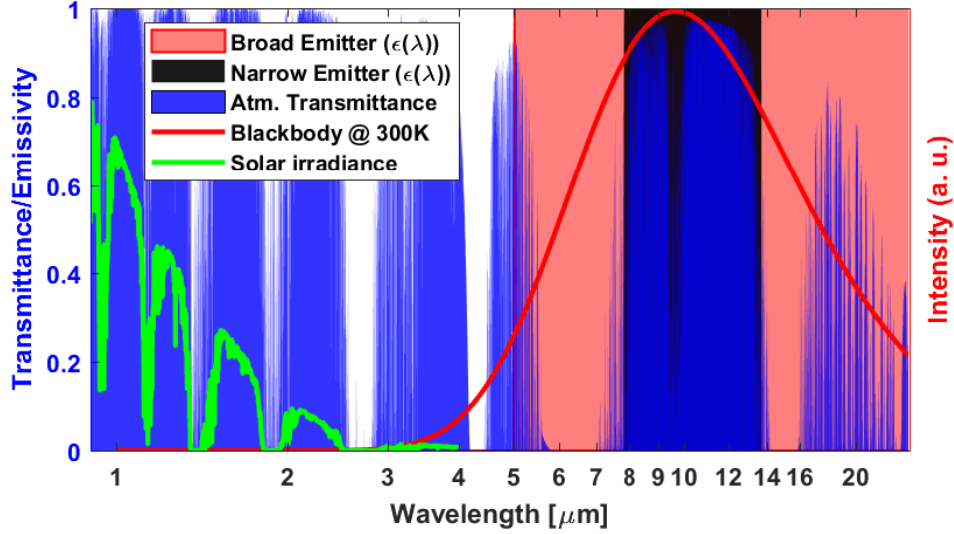

Figure B.1: Relevant spectra involved in radiative cooling. Green line is the solar spectrum (AM1.5). Red line is a black-body at 300 K. Blue shaded area is the transmission spectrum of the atmosphere. Red area is the ideal emissivity of a broad emitter ($\epsilon = 1\,[\lambda > 5\mu m]$). Black area is the emissivity of an ideal narrow emitter ($\epsilon = 1\,[7.8\mu m < \lambda < 13.7\mu m]$).

Of equal, if not more, importance is the spectral region below 5 μm where the strong solar spectrum exists (green line in figure B.1). Because the radiative cooler must face the sky to take advantage of deep space as a heat sink, it necessarily must also be exposed to the sun in the daytime hours. For this reason it is essential that any device reflect this radiation back to the atmosphere. Absorption of solar radiation can hinder or completely eliminate any cooling effect from a radiative cooler.

We will look at the cooling power for two idealized emitters. The first "broad" emitter having $\epsilon = 1$ for $\lambda > 5$ and second, a "narrow" emitter having $\epsilon = 1$ for $7.8\mu m < \lambda < 13.7\mu m$. To analyze the performance of these two types of emitters, we have plotted their net cooling power as a function of emitter temperature in figure B.2. For these calculations, we have assumed an atmospheric temperature of 300 K, the emitter absorbs 5% of the sun's energy (P_{sun}), and that the conductive and convective heat transfer (P_{con})

is a nominal 2 $W/m^2 K$. We see that for higher temperatures, the device benefits from having broader emissivity and therefore higher emissive power. In contrast, the ideal emitter has higher cooling power once the temperature of the device drops below 291 K. It is also able to reach a lower equilibrium temperature, which occurs once $P_{cool} = 0$.
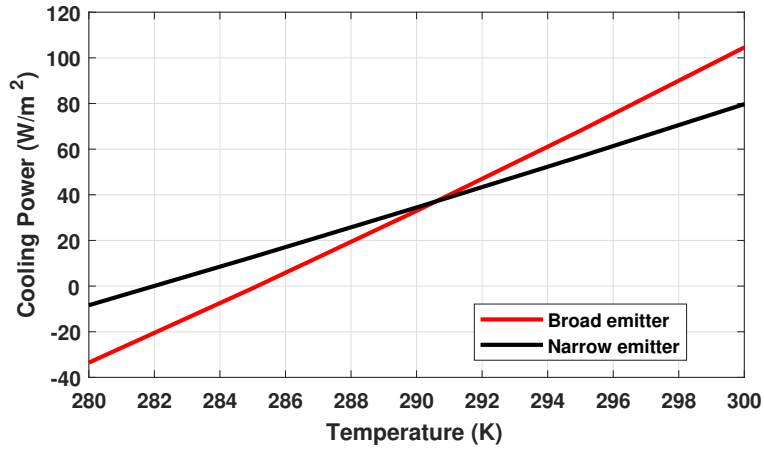

Figure B.2: Relevant spectra involved in radiative cooling.

Appendix C

Mie Scattering Calculation

C.1 Mie Coefficients for Spherical Particle

For spherical particles we can calculate the extinction, scattering and absorption efficiencies using equations (C.1), (C.2) and (C.3) [90].

$$Q_{sca} = \frac{2}{x^2} \sum_{n=1}^{n_{max}} (2n+1)(|a_n|^2 + |b_n|^2) \tag{C.1}$$

$$Q_{ext} = \frac{2}{x^2} \sum_{n=1}^{n_{max}} (2n+1)Re(a_n + b_n) \tag{C.2}$$

$$Q_{ext} = Q_{sca} + Q_{abs} \tag{C.3}$$

Where x is the size parameter ($k_0 r$). a_n and b_n are the Mie coefficients. For spherical particles of dielectric materials as we are considering, they can be calculated using equations (C.4) and (C.5).

$$a_n = \frac{m^2 j_n(mx)[x j_n(x)]' - j_n(x)[mx j_n(mx)]'}{m^2 j_n(mx)[x h_n^{(1)}(x)]' - h_n^{(1)}(x)[mx j_n(mx)]'} \tag{C.4}$$

$$b_n = \frac{j_n(mx)[x j_n(x)]' - j_n(x)[mx j_n(mx)]'}{j_n(mx)[x h_n^{(1)}(x)]' - h_n^{(1)}(x)[mx j_n(mx)]'} \tag{C.5}$$

Here, $h_n^{(1)}(x) = j_n(x) + i y_n(x)$ are the spherical Hankel functions of order n, $j_n(x)$ and $y_n(x)$ are the spherical Bessel functions of order n, m is the relative refractive index of the particle medium and again x is the size parameter. As the particle size becomes larger it is able to support more polar modes

with the particles volume and therefore we need to consider more terms in the summation within equations C.1 and C.2. Bohren and Huffman [112] propose that the infinite series can be truncated to $n_{max} = x + 4x^{1/3} + 2$ which is also used here.

C.2   Mie Coefficients for Cylindrical Particle

For cylindrical shaped particles with high aspect ratio, we can approximate the scattering and absorption widths as that for an infinitely long cylinder. If we consider normal incidence (light propogating perpendicular to the cylinder axis), we can have two polarizaton states

(i) $E \parallel z$

$$C_{sca} = \frac{2}{k_0 r} \sum_{n=-\infty}^{n=\infty} |b_n|^2 \,, \tag{C.6}$$

$$C_{abs} = \frac{2}{k_0 r} \sum_{n=-\infty}^{n=\infty} \left(-\operatorname{Re} b_n - |b_n|^2 \right) , \tag{C.7}$$

$$C_{ext} = -\frac{2}{k_0 r} \sum_{n=-\infty}^{n=\infty} \left(\operatorname{Re} b_n \right) , \tag{C.8}$$

with

$$b_n = \frac{k_i J_n'(k_i r) J_n(k_0 r) - k_0 J_n(k_i r) J_n'(k_0 r)}{k_0 J_n(k_i r) H_n'(k_0 r) - k_i J_n(k_i r) H_n(k_0 r)} \,, \tag{C.9}$$

where $k_0 = \varepsilon_M^{1/2} \omega / c$, $k_i = \varepsilon^{1/2} \omega / c$ are spherical harmonics and J_n and H_n are cylindrical Bessel and Hankel functions respectively.

(ii) $E \perp z$

$$C_{sca} = \frac{2}{k_0 r} \sum_{n=-\infty}^{n=\infty} |a_n|^2 \,, \tag{C.10}$$

$$C_{abs} = \frac{2}{k_0 r} \sum_{n=-\infty}^{n=\infty} \left(-\mathrm{Re}\, a_n - |a_n|^2 \right), \tag{C.11}$$

$$C_{ext} = -\frac{2}{k_0 r} \sum_{n=-\infty}^{n=\infty} \left(\mathrm{Re}\, a_n \right), \tag{C.12}$$

with

$$a_n = \frac{k_i J_n(k_i r) J_n'(k_0 r) - k_0 J_n'(k_i r) J_n(k_0 r)}{k_0 J_n'(k_i r) H_n(k_0 r) - k_i J_n(k_i r) H_n'(k_0 r)} . \tag{C.13}$$

Following these equations we can calculate the scattering, absorption and extinction efficiencies as

$$Q_b = \frac{C_b}{2r}, \tag{C.14}$$

where $b = abs, sca, ext$. The methodology for calculating the absorption, scattering and extinction efficiency of cylindrical particles is taken from [89], [112].

Appendix D

Tungsten Sputtering

To measure thermal emission from polaritonic particles, they must be deposited on a substrate with a low emissivity to suppress background thermal radiation. Highly reflective metal thin films are a natural choice. However, are not stable at the temperatures we wish to achieve. Tungsten is a refractory metal with high reflectivity in the infrared that has the ability to sustain high temperature environments.

To find the best conditions for depositing a highly reflective thin film, we span argon sputtering pressure and DC power supplied to the tungsten target during sputter deposition. Table D.1 shows the parameters used for different deposition runs.

Table D.1: Table of tungsten Sputtering parameters

Sample no.	Power [W]	Ar Pressure [mTorr]	time [mm:ss]	thickness [nm]
1	120	7	5:00	-
2	120	5	5:00	-
3	120	3	5:00	60.2
4	120	2	5:00	54.3
5	120	2	27:34	300

The IR reflectivity of the resulting films is measured using a home built FTIR reflection set up. We can see in figure D.1 that for lower pressures and a power of 120 Watts, we are able to achieve reflectivity values of ¿90% throughout the mid-IR region. The green highlighted set of parameters in table D.1 are the final parameters used for tungsten thin films used throughout this

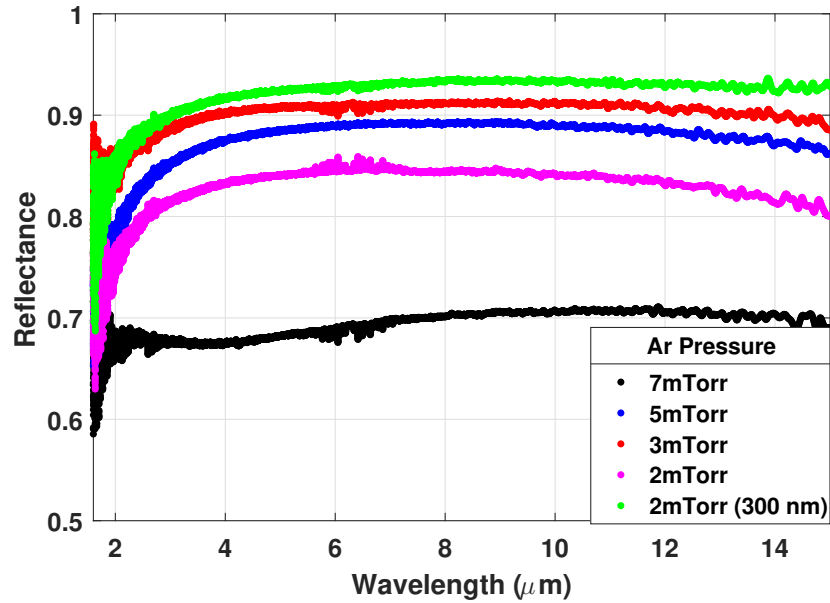thesis. Its reflectivity spectrum is also the green line in figure D.1.

Figure D.1: Infrared reflectance of sputtered tungsten thin films deposited using different argon pressure.

To confirm the tungsten thin film has low emissivity behavior even at high temperatures, thermal emission measurements are taken of the thick highly reflective film and the emissivity spectrum at varying temperature is shown in figure D.2. We see that even at high temperature, tungsten thin films exhibit emissivity values of ≈ 0.1 throughout the mid-IR spectrum.
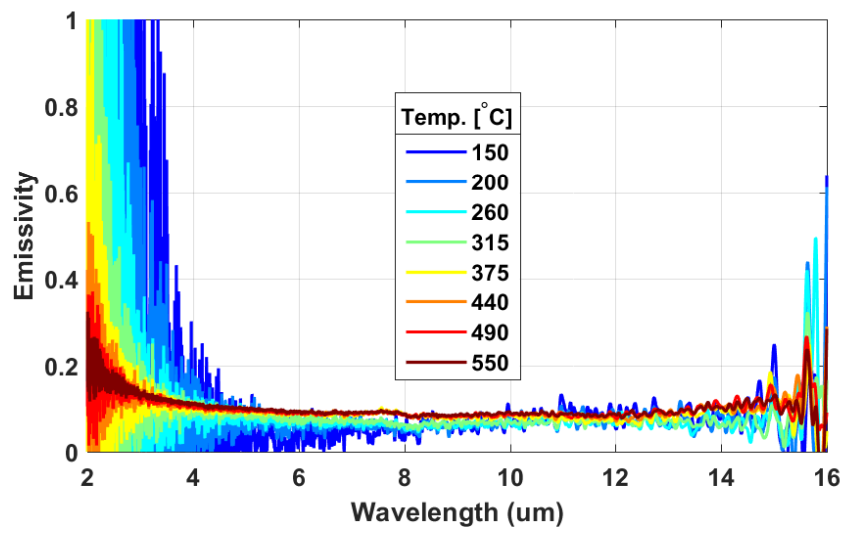
Figure D.2: Thermal emission spectrum of 300 nm tungsten thin film on a Si substrate.